© 2010 by Tyson Aaron Olheiser. All rights reserved.

PENETRATION DEPTH MEASUREMENTS OF ORGANIC SUPERCONDUCTORS

BY

TYSON AARON OLHEISER

DISSERTATION

Submitted in partial fulfillment of the requirements
for the degree of Doctor of Philosophy in Physics
in the Graduate College of the
University of Illinois at Urbana-Champaign, 2010

Urbana, Illinois

Doctoral Committee:

Professor Dale Van Harlingen, Chair
Professor Russell Giannetta, Director of Research
Professor Michael Stone
Professor Tony Liss

Abstract

The temperature dependence of the magnetic penetration depth (λ) has been measured in single crystals of fully deuterated κ-$(ET)_2Cu[N(CN)_2]Br$. This material separates into superconducting (SC) and antiferromagnetic (AFI) phases. The relative amounts of SC and AFI phases has been shown to depend on the cooling rate of these materials in the vicinity of 80 K. In varying the cooling rate from 0.0025-180 K/min, the Meissner fraction appears to vary logarithmically with the cooling time, suggesting that these organics act like a glassy system near 80 K where SC nucleation grains are formed. In addition, the penetration depth of deuterated κ-$(ET)_2Cu[N(CN)_2]Br$ consistently displays a power law temperature dependence with an exponent of $n = 1.6$-1.8 for Meissner fractions ranging from 0.03-0.60. This suggests that these samples are robust dirty d-wave superconductors like their undeuterated counterpart.

With abnormally large penetration depths resulting from traditional analysis, an aluminum plating technique was used to measure the absolute penetration depth of deuterated κ-$(ET)_2Cu[N(CN)_2]Br$. The large values of $\lambda(0)$ were confirmed with this technique. Measurements yielded values that increased from 29-320 μm with increasing cooling rate. This finding motivated the development of a SC spherical grain model where the deuterated sample was assumed to be a collection of independent spheres of undeuterated κ-$(ET)_2Cu[N(CN)_2]Br$. The model yielded grain sizes on the order of 5-40 μm, which agrees well with literature. Also, high and low temperature data was checked for self consistency.

In addition to this work, the temperature dependence of the interplane penetration depth of undeuterated κ-$(ET)_2Cu[N(CN)_2]Br$ was performed. With higher order corrections to the traditional analysis accounted for, a value of $\lambda_\perp = 130$ μm was measured. Also, the temperature dependence of the superfluid density was similar to in-plane behavior, suggesting that interplane transport in these materials is coherent despite being highly anisotropic and definitely 2D in nature.

Table of Contents

Chapter 1 Motivations **1**

Chapter 2 Experimental Background **5**
2.1 Oscillator Electromagnetic Theory 5
2.2 Tunnel Diode Circuitry Design and Stability 9
2.3 Oscillator Circuit Theory 14
2.4 Calibration 16
2.5 Frequencies 18
2.6 Penetration Depth from Raw Data 22
2.7 Cryostat 23

Chapter 3 Penetration Depth **28**
3.1 Superconductivity 28
3.1.1 History 28
3.1.2 Mechanism 28
3.1.3 Superconducting Gap 29
3.2 Penetration Depth 32
3.2.1 London Equations 32
3.2.2 Penetration Depth Behavior: High T 33
3.2.3 Penetration Depth Behavior: Low T 35
3.3 Aluminum Plating 36

Chapter 4 In-Plane Penetration Depth of Deuterated κ-$(ET)_2Cu[N(CN)_2]Br$ **41**
4.1 Temperature Dependence of $\Delta\lambda_{d8}$ 43
4.2 Absolute Values of Penetration Depth 45
4.3 Spherical Grain Analysis 51
4.4 Conclusions 60

Chapter 5 Interplane Penetration Depth of κ-$(ET)_2Cu[N(CN)_2]Br$ **61**
5.1 Experimental 61
5.2 Penetration Depth and Superfluid Density 63
5.3 Discussion 65
5.4 Summary 69

Appendix A Attempted STM Fabrication of MgB_2 Nanoislands **70**
A.1 Introduction 70
A.2 Experiment 70
A.3 Conductance Spectroscopy 74
A.4 Discussion 74
A.5 Conclusion 75

References **76**

Chapter 1

Motivations

From the time of the discovery of superconductivity until the early 1980's, the highest recorded critical temperatures (T_c) were 20-23 K. At that point, the theory produced by Bardeen, Cooper, and Schrieffer (BCS) accurately characterized these materials as uniformly gapped, s-wave superconductors with a phonon-mediated pairing mechanism[1]. With the discovery of LaBaCuO in 1986, the scientific community struggled to explain their findings using the BCS picture[2]. Although the proposed theoretical limits of T_c for a phonon-mediated mechanism were exceeded, some attempted to modify and explain old theories in order to make LaBaCuO fit the conventional picture. With the discovery of superconductivity in YBaCuO in 1987[3], a T_c value of 90 K required scientists to take a new look at the mechanism and gap structure of this class of superconductors called the *cuprates*[4].

Around the same time frame as the cuprates, organic superconductors were discovered almost by accident. At this time, organic synmetals were studied extensively. The idea of nonmetallic materials displaying a metal-like behavior was a fascinating possibility that could shed light on current understanding of conductivity. In 1973, Ferraris et al. made the first organic synmetal[5]. Following this breakthrough, Bechgaard studied pressure effects on a new set of salts which led to the discovery of superconductivity with T_c = 1-2 K[6]. The first ambient pressure organic superconductor was found in 1981[7].

Superconductivity was first discovered in the κ-(BEDT-TTF)$_2$X (κ-(ET)$_2$X) family in 1988[8]. Although other organic superconductors were known at the time, this family exhibited some characteristics strikingly similar to the cuprates. In terms of structure, κ-(ET)$_2$X mimicked the cuprates in that they behaved like stacked 2D conducting planes. This is evidenced by a large anisotropy of the in-plane and interplane resistivities where $\rho_\perp/\rho_{||} \approx 1000$ in these materials[9]. Also, DC-magnetization measurements yielded an interplane coherence length of $\xi_\perp = 4$ Å[10]. Since the spacing between conducting layers (1.5 nm) is considerably smaller than $\xi_\perp$, this material truly represents a 2D system.

In addition to the electronic structure, both κ-(ET)$_2$X and cuprates appear to have nodal superconducting gaps that most likely represent a d-wave symmetry. Although some experiments have claimed s-wave pairing[12], penetration depth[13,14,15], thermal conductivity[16,17], specific heat[18,19] and STM[20] experiments

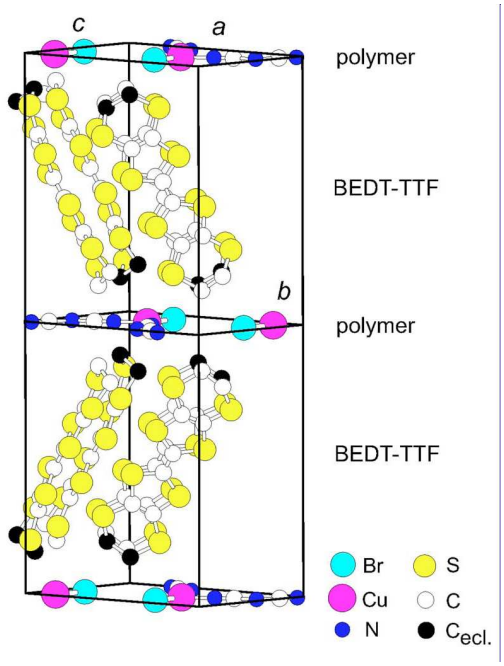


Figure 1.1: The structure of κ-$(ET)_2Cu[N(CN)_2]Br$ consists of BEDT-TTF molecule pairs that are separated by insulating polymers. The terminating ethylene groups are depicted in the eclipsed formation. Reprinted with permission.[11].

all provide strong support for nodal quasiparticles. Although the majority of measurements suggested a gap with nodes, the most convincing pieces of evidence for d-wave came from NMR measurements that confirmed a spin singlet state[21,22].

The most striking similarity between the cuprates and the κ-$(ET)_2X$ family involves their respective phase diagrams. In the case of the cuprates, the properties of the material strongly depend on the oxygen doping level. A cartoon representation of the YBaCuO phase diagram is given in Fig. 1.2. Notice that only a specific range of oxygen doping results in a superconductor (SC) with a critical temperature that depends on the specific oxygen level. In addition, underdoping can result in the system arranging itself into an antiferromagnetic insulator (AFI) that is separated from the superconducting phase by a pseudogap region. In the case of the κ-$(ET)_2X$ family, the phase diagram is remarkably similar. The temperature vs. pressure diagram for κ-$(ET)_2Cu[N(CN)_2]Cl$ is shown in Fig. 1.3. Notice there also appears to be SC and AFI phases determined by the external pressure, with the ambient pressure state of κ-$(ET)_2Cu[N(CN)_2]Cl$ being an AFI. It is believed that undeuterated κ-$(ET)_2Cu[N(CN)_2]Br$ behaves similar to κ-$(ET)_2Cu[N(CN)_2]Cl$ for pressures greater than 400 bar, where the system behaves like a SC. However, deuteration of the terminating hydrogen atoms of the ET chains in κ-$(ET)_2Cu[N(CN)_2]Br$ has been shown to push the sample into a coexistant state of SC and AFI phases[23]. Connecting to the κ-$(ET)_2Cu[N(CN)_2]Cl$ picture, the conventional

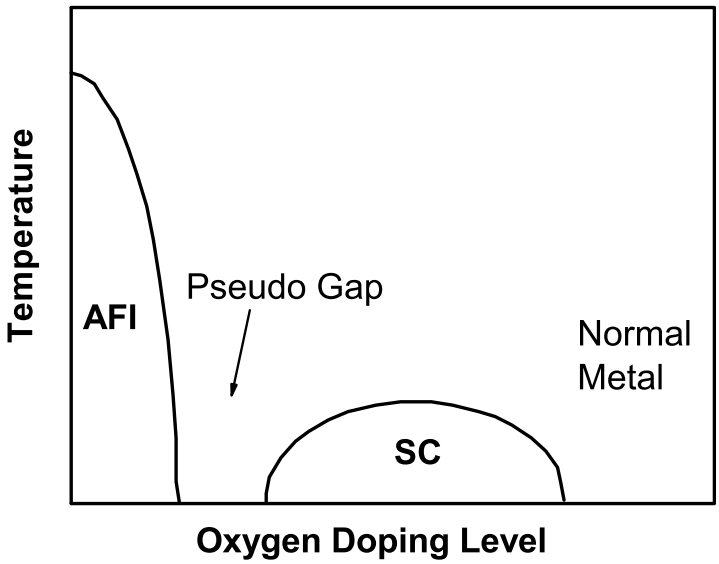


Figure 1.2: The critical temperature versus oxygen doping fraction phase diagram for YBaCuO.

thought is that deuteration produces an internal pressure that effectively shifts the specimens laterally in the phase diagram into the coexistance region corresponding to 300 bar. Also, the cooling rate of the deuterated κ-$(ET)_2Cu[N(CN)_2]Br$ has been shown to change the T_c as well as determine the relative amounts of SC and AFI phases[24].

These interesting characteristics motivated this investigation into the penetration depth behavior of these organics. Although a variety of measurements indicate that undeuterated (h8) κ-$(ET)_2Cu[N(CN)_2]Br$ has an in-plane penetration depth $\lambda_{||} \sim 1$ μm at 0K, a definitive measure of the in-plane penetration depth of deuterated (d8) κ-$(ET)_2Cu[N(CN)_2]Br$ was lacking. Since most techniques are only capable of measuring changes in λ, a tunnel diode oscillator technique involving aluminum plated samples was used to measure the absolute penetration depth of these samples for varying cooling rates. This also provided a way to determine the superconducting fraction as a function of cooling rate and possibly support the picture of a coexistence of SC and AFI phases. In addition, high resolution measurements of the temperature dependence of λ for $T < T_c/3$ were taken to probe the nature of the superconducting gap.

Although deuterated samples were the main focus of the project, there was still some unanswered questions regarding the undeuterated system. A wide range of values measured for the interplane penetration depth ($\lambda_\perp(0) = 30 - 220$ μm) demanded a more careful analysis. Using a well chosen sample geometry measured in a tunnel diode oscillator, a more confident value for $\lambda_\perp(0)$ was obtained through a more precise treatment of the sample geometry and calculation of penetration depth values from frequency data. Also, the temperature dependence of the λ was used to determine the coherence of interplane currents.

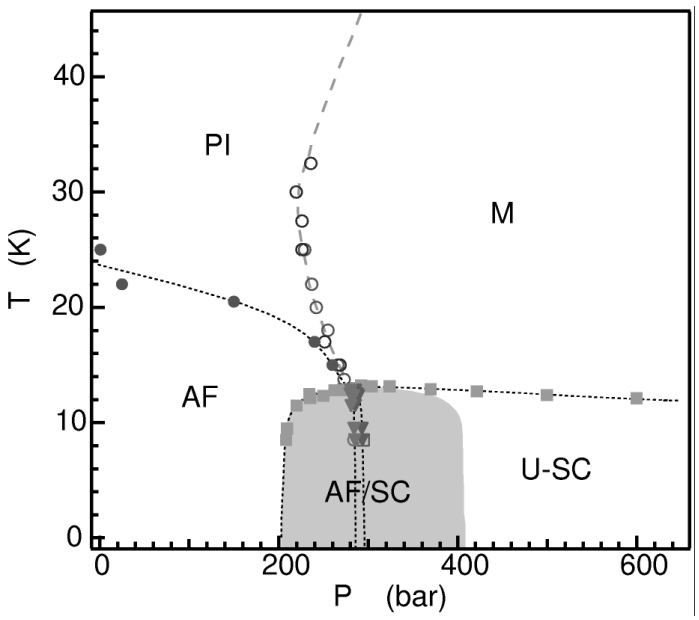


Figure 1.3: The critical temperature versus pressure phase diagram for κ-$(ET)_2Cu[N(CN)_2]Cl$. At low temperatures, the material acts like an antiferromagnet at ambient pressure. As the pressure increases, the material undergoes a transition to a superconductor with a coexistence region. Reprinted with permission.[25]

Chapter 2

Experimental Background

2.1 Oscillator Electromagnetic Theory

The tunnel diode oscillator technique probes the AC-magnetic susceptibility of samples exposed to a magnetic field produced by a coil that is part of an LC tank circuit. When an ideal superconducting sample is placed in a coil at $T = 0$, the net coil volume will be that of the empty coil volume minus the effective volume taken up by the sample. As the temperature increases, the penetration depth (λ) of the superconductor will increase. This will result in a larger net coil volume, which will change the resonance frequency of the LC circuit. Therefore, the changes in measured frequency will be directly related to changes in λ.

This connection between frequency and λ first requires an expression for the total impedance of the sample volume. This is accomplished by examining Poynting's theorem, which involves the electric field ($\mathbf{E}$) and current density ($\mathbf{J}$). Starting with the expression

$$\frac{1}{2}\int_V \mathbf{J}^* \cdot \mathbf{E}\, d^3x \tag{2.1}$$

the following definition of $\mathbf{J}$, a vector identity, and a Maxwell equation

$$\mathbf{J} = \nabla \times \mathbf{H} + i\omega\mathbf{D} \tag{2.2}$$

$$\mathbf{A} \cdot (\nabla \times \mathbf{B}) = \nabla \cdot (\mathbf{B} \times \mathbf{A}) + \mathbf{B} \cdot (\nabla \times \mathbf{A}) \tag{2.3}$$

$$\nabla \times \mathbf{E} = -\frac{\partial \mathbf{B}}{\partial t} = i\omega\mathbf{B} \tag{2.4}$$

are used to get the following expression[26]

$$\frac{1}{2}\int_V \mathbf{J}^* \cdot \mathbf{E}\, d^3x = \int_V \nabla \cdot \left[-\frac{1}{2}\mathbf{E} \times \mathbf{H}^*\right] d^3x + \frac{i\omega}{2}\int_V (\mathbf{B} \cdot \mathbf{H}^* - \mathbf{E} \cdot \mathbf{D}^*)\, d^3x \tag{2.5}$$

where $\mathbf{H}$ is the auxillary field, $\mathbf{B}$ is the magnetic field, $\mathbf{A}$ is the vector potential, and ω is the field oscillation

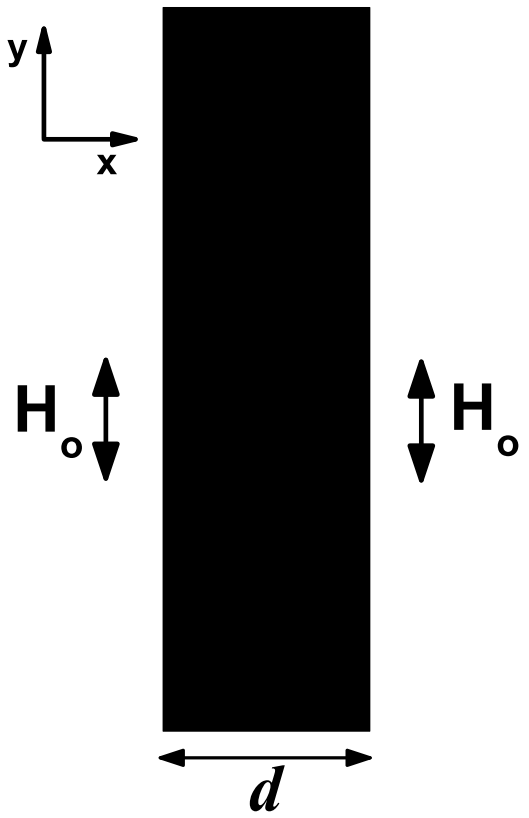


Figure 2.1: A thin superconducting slab of thickness d in a field $\mathbf{H}_0$. The origin is situated in the center of the slab

frequency. The bracketed portion is the Poynting vector ($\mathbf{S}$), which represents the power density of the electromagnetic fields. Using the divergence theorem, it is clear that the first term on the right hand side represents the average power going in or out of the sample volume. For the simplified case of a sample with negligible polarization and magnetization, ($\epsilon \approx \epsilon_o$, $\mu \approx \mu_o$) and neglecting energy loss by radiation

$$-\int_V \nabla \cdot \mathbf{S}\, d^3x = -\oint_S \mathbf{S} \cdot \widehat{n}\, d^2x = \frac{1}{2} I^2 Z \tag{2.6}$$

$$Z(\omega) = \frac{1}{I^2}\left[(\sigma^* + i\omega\epsilon_o)\int_V |\mathbf{E}|^2 d^3x - i\omega\mu_o \int_V |\mathbf{H}|^2\, d^3x\right] \tag{2.7}$$

where σ is the conductivity. Thus, the impedance (Z) of the sample can be derived if the $\mathbf{E}$ and $\mathbf{H}$ fields are found and integrated over the sample volume. As a specific example, a slab of thickness d will be examined in a parallel field, $\mathbf{H_o}$. The situation is shown in Fig. 2.1. The spatial dependence of the magnetic field inside the sample is obtained from the London equations.

$$\nabla^2\mathbf{H} = -i\sigma\mu_o\omega\mathbf{H} \equiv (1/\lambda)^2\mathbf{H} \tag{2.8}$$

As it turns out, the conductivity for an ideal superconductor is purely imaginary.

Since the slab lies in the yz-plane, the field strength will only depend on x. Also, since the external field is along the $\hat{y}$, the field inside will also point in the same direction. This results in the general solution

$$\mathbf{H} = [Ae^{-x/\lambda} + B^{x/\lambda}]\hat{y} \tag{2.9}$$

Using the boundary conditions of the sample $H(d/2) = H(-d/2) = H_o$, the exact expression becomes

$$\mathbf{H} = \left[H_o \frac{\cosh(x/\lambda)}{\cosh(d/2\lambda)}\right]\hat{y} \tag{2.10}$$

With the magnetic field derived, the next step is to calculate the electric field. Since the tunnel diode operating frequency is on the order of MHz, the Maxwell equations can be used in the low frequency limit ($\mu_o\sigma = (\omega\lambda^2)^{-1} >> \omega/c^2$). The resulting electric field can be found from $\mathbf{H}$ in the following way

$$\frac{\partial H}{\partial x}\hat{z} = \sigma\mathbf{E} = \frac{i}{\mu_o\omega}\frac{1}{\lambda^2}\mathbf{E} \tag{2.11}$$

$$\mathbf{E} = i\mu_o\omega\lambda H_o \frac{\sinh(x/\lambda)}{\cosh(d/\lambda)} \tag{2.12}$$

With the two fields derived, the impedance of the sample can be determined using Eqn. 2.7. It must be remembered that this experiment is run at a low frequency ($f << \lambda/c$), which amounts to calling the σ^* term negligible from Eqn. 2.7. Therefore, the impedance per surface area (A_s) is calculated

$$Z = -i\omega\mu_o A_s\lambda\left(\frac{H_o}{I}\right)^2 \frac{\sinh(2d/\lambda)}{\cosh^2(d/\lambda)} \tag{2.13}$$

In order to account for impedance changes from the sample, we use the empty coil as a reference. From basic E&M, the impedance of a coil is $Z_{coil} = -i\omega L_{coil}$. In looking at the relationship between coil EMF and flux (Φ), the inductance of the coil (L_{coil}) can be derived

$$V = -\frac{d\Phi}{dt} = -NA_{turn}\frac{dB}{dt} = -NA_{turn}\left(\mu_o\frac{N}{\ell}\frac{dI}{dt}\right) = -\mu_o n^2 V_{coil}\frac{dI}{dt} \equiv -L_{coil}\frac{dI}{dt} \tag{2.14}$$

where A_{turn} and N represent the area and number of turns, ℓ is the length of the coil, and n is the number of turns per unit length. Since the only piece of the coil volume that is capable of changing the impedance

is that pertaining to the sample, the change in impedance is

$$\delta Z = Z_{in} - Z_{out} = Z_s - Z_s(\lambda \to \infty) \tag{2.15}$$

$$\delta Z = -i\omega \left\{ \mu_o n^2 V_s \left[\frac{2\lambda}{d} \tanh(d/2\lambda) - 1 \right] \right\} \equiv -i\omega \delta L \tag{2.16}$$

With a relationship between the penetration depth and changes in coil inductance, the last step is to relate changes in the inductance (δL) to changes in the measured resonance frequency. This is done by looking at small changes in the resonance frequency (ω_o) due to small changes in the inductance

$$\omega_o = \sqrt{\frac{1}{L_o C}} \tag{2.17}$$

$$\frac{\delta\omega}{\omega_o} = -\frac{1}{2}\frac{\delta L}{L_o} \tag{2.18}$$

where L_o and L_{coil} are used synonymously. Since the change in the inductance due to the sample is given in Eqn. 2.16 and L_o is simply the inductance of the empty coil, a direct relationship between oscillator frequency and penetration depth at any given sample temperature can be found

$$\frac{f_s(T) - f_{ec}}{f_{ec}} = \frac{V_s}{2V_c}\left(1 - \frac{2\lambda(T)}{d}\tanh\frac{d}{2\lambda(T)}\right) \tag{2.19}$$

/noidnent where $f_s(T)$ represents the frequency of the coil upon inserting the sample. It must be emphasized that the above analysis can only be applied to thin samples that have an infinite surface area. Furthermore, it was assumed that the slab was isotropic. In order to treat the case of a 2D system, the expression derived by Mansky *et al.* was used[27]

$$\frac{f_s(T) - f_{ec}}{f_{ec}} = \frac{V_s}{2V_c}\left(1 - \frac{2\lambda_{||}(T)}{d}\tanh\frac{d}{2\lambda_{||}(T)} - \frac{16\lambda_\perp}{\pi^2 w}\sum_{n=0}^{\infty}\frac{\tanh q_n w/2}{(2n+1)^2(k_n^2\lambda_{||}^2+1)^{3/2}}\right) \tag{2.20}$$

where $k_n = \frac{2n+1}{d}\pi$ and $q_n^2 = \frac{k_n^2\lambda_{||}^2+1}{\lambda_\perp^2}$. A picture of the situation is given as Fig. 2.2. Upon closer inspection, this expression depends on the ratios $\lambda_{||}/d$, $\lambda_\perp/w$, and their magnitudes relative to one another. For the case of YBCO, Hardy and coworkers used thin samples with large surface areas to isolate $\lambda_{||}$[28]. Since $\lambda_\perp/\lambda_{||} \sim 10$ in YBCO, this was accomplished by placing samples with a geometry of $w/d \sim 100$ in a parallel magnetic field.

As for the organics, preliminary experiments as well as work done by other groups suggested ratios on

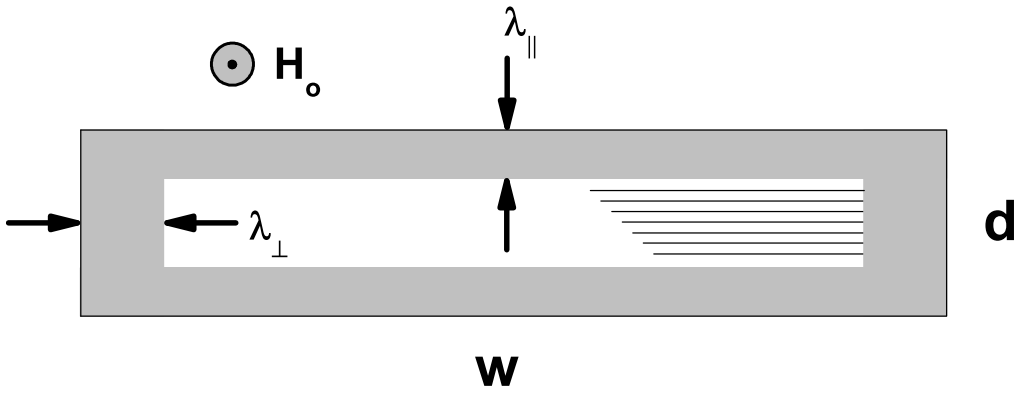


Figure 2.2: A superconducting slab of thickness d and width w in a parallel field $\mathbf{H}_0$.

the order of $\lambda_\perp/\lambda_{||} \sim 100$ [13,29,30,15]. Given the difficulty of finding sample geometries that have length to thickness aspect ratios of 1000, a new approach was needed. With the goal of isolating $\lambda_{||}$ in mind, a flat slab was placed in a perpendicular magnetic field to assure that all supercurrents would flow in the conducting planes. The difficulty with this approach is determining the demagnetization factor for this orientation. In 2000, Prozorov and Giannetta provided a much needed analysis of a rectangular slab in a perpendicular field [31]. In short, the complications of sample geometry were modeled as

$$\frac{f_s(T) - f_{ec}}{f_{ec}} = \frac{1}{1-N}\frac{V_s}{2V_c}\left(1 - \frac{\lambda(T)}{R_{eff}}\tanh\frac{R_{eff}}{\lambda(T)}\right) \tag{2.21}$$

where R_{eff} is an effective dimension that depends on the sample length and thickness. This analysis was key to the work done in this project.

2.2 Tunnel Diode Circuitry Design and Stability

The circuit used in this experiment is shown in Fig. 2.3. The DC equivalent circuit is given as Fig. 2.4. From a DC standpoint, all of the inductors and capacitors can be treated as shorts and breaks in the circuit, respectively. The role of resistors R_1 and R_2 was to bias the tunnel diode to the proper location

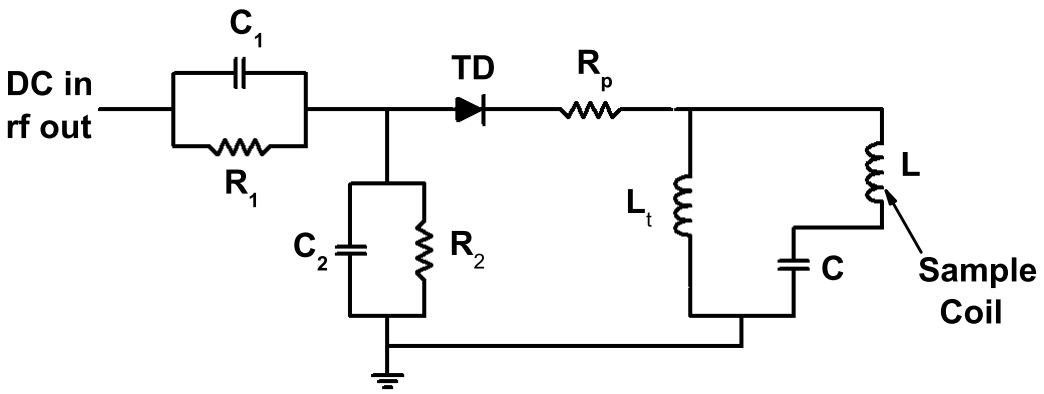


Figure 2.3: The tunnel diode circuit with the sample coil playing the role of the inductor in the LC tank oscillator.

in its IV curve where it exhibits negative resistance ($-R_d$). The IV curve for the tunnel diode is given in Fig. 2.5. In choosing the best tunnel diode for our experiment, the slope of the negative resistance region was calculated. Since the point of the tunnel diode is to provide a zero resistance LC tank circuit, the slope had to be comparable to the expected impedance of the circuit. This is essential for oscillation. From an AC perspective, the capacitors C_1 and C_2 play a crucial role. The smaller C_1 provides an effective short circuit across R_1 for the signal. The capacitance of C_2 is much larger and acts as an initial filter that shorts any high frequency noise or harmonics before it reaches the room temperature electronics.

In order for the experiment to operate, there were two conditions that had to be satisfied. First, there must be a way to properly bias the tunnel diode into its negative resistance state. Second, shifts in oscillator frequency must be measurable. As it turns out, both of these operations can be carried out in one coax line. Effectively, the coax is set at a particular DC bias that indirectly produces an AC signal that travels back up the biased line. The tunnel diode biasing was performed using a temperature stabilized voltage reference (Burr-Brown REF-10) that outputs voltages steady to $\pm 5\mu\mathrm{V}/^{\circ}C$. Care was taken to use a voltage divider that resulted in minimizing the power input to the tunnel diode circuit in order to prevent self-heating at

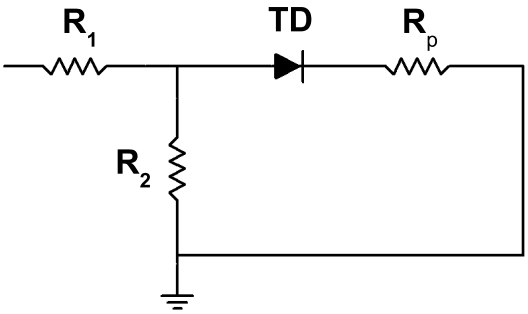


Figure 2.4: The equivalent DC circuit used to bias the TD.

low temperatures.

Due to the sensitivity of the experiment, certain measures were taken to minimize vibration and effects due to thermal instability. All vacuum pumping lines were buried in sand between the pumps and cryostat. Also, all pumps were kept outside of the Faraday cage in which the experiment was performed. The dewar was placed on a styrofoam platform to minimize vibrations from foot traffic near the experiment. For thermal stability, all of the biasing circuitry as well as the tunnel diode and capacitor components were temperature controlled at 3K. This temperature was chosen in order to minimize the heat load on other nearby components. Polystyrene capacitors provided the best stability and lowest field dependence.

The coil itself is isolated from the circuitry using g10 insulating rods as shown in Fig. 2.6. Thermally anchored to the 1K pot, the coil temperature is rigidly maintained at roughly 2K. The 1K pot was chosen as the heat sink for two reasons. First, the coil is weakly heat sunk to the ^{3}He stage. Therefore, a lower coil temperature is less likely to heat up this stage. Second, it is important to heat sink the coil to a stage that has a large cooling power. This helps eliminate the possibility of the sample heating the coil when taking temperature sweeps. The importance of stabilizing the coil temperature cannot be over stated. The basic assumption of the experiment is that the entire frequency shift of the LC circuit is due to changes in the sample, which is contained inside the coil. If the coil temperature is variable, this assumption is false and information about the sample penetration depth cannot be decoupled from the frequency shift due to the coil itself.

Since the experiment involves measuring the signal of a small sample in a coil, the sample holder needed

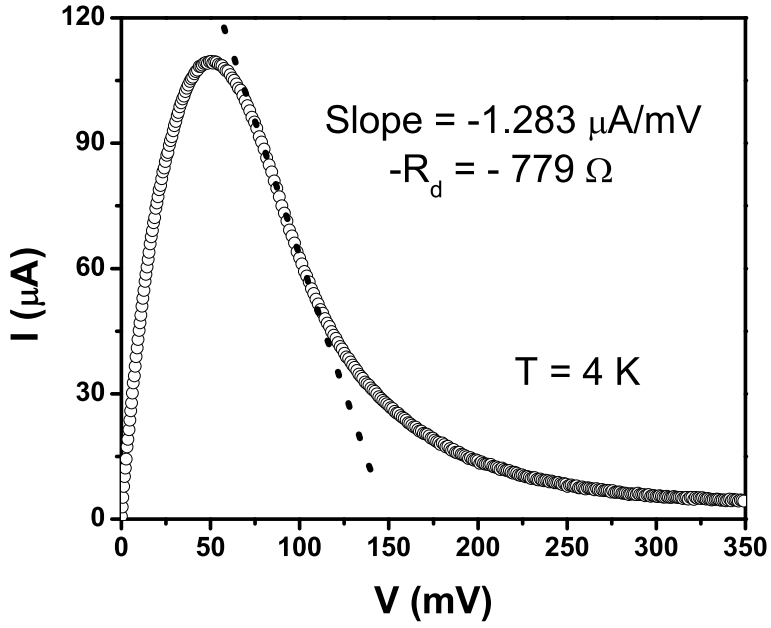


Figure 2.5: The IV curve for the tunnel diode used in the experiment.

two qualities. First, it had to be temperature and field independent with regards to susceptibility. Otherwise, the data would represent a complex convolution of sample and holder susceptibilities. Second, the holder needed to be thermally conducting in order to change the temperature of the sample. The material that best satisfied these two criteria was sapphire. In terms of magnetic susceptibility, sapphire remains in the range -0.2 to -0.35$\times 10^{-6}$ emu/g for temperatures ranging from 1-300K, respectively[32]. In other words, this material exhibits a slight paramagnetic shift that changes very little with temperature. In addition, sapphire has a thermal conductivity comparable to copper for temperatures down to 10 K.[33]

Although it is obviously important to keep bulk hardware cold throughout the measurement, the wires themselves have the potential of warming up pieces of the experiment. Thin resistive wiring used for thermometry and heaters can easily be anchored to stages using tape or varnish. However, coax wires required more care because of the insulating layer between the outer and inner conductors. This problem was remedied through the use of a stripline. The inner conductor of the coax originating at the head of the cryostat is soldered to one end of the stripline, which is thermally connected to the ^{4}He bath. The other end is soldered to another coax that continues down to the tunnel diode circuitry. In order to preserve signal amplitude, the geometry of the stripline was designed to be 50 Ω. Also, this coax heat sink was shielded with a copper cover plate to reduce stray rf interference.

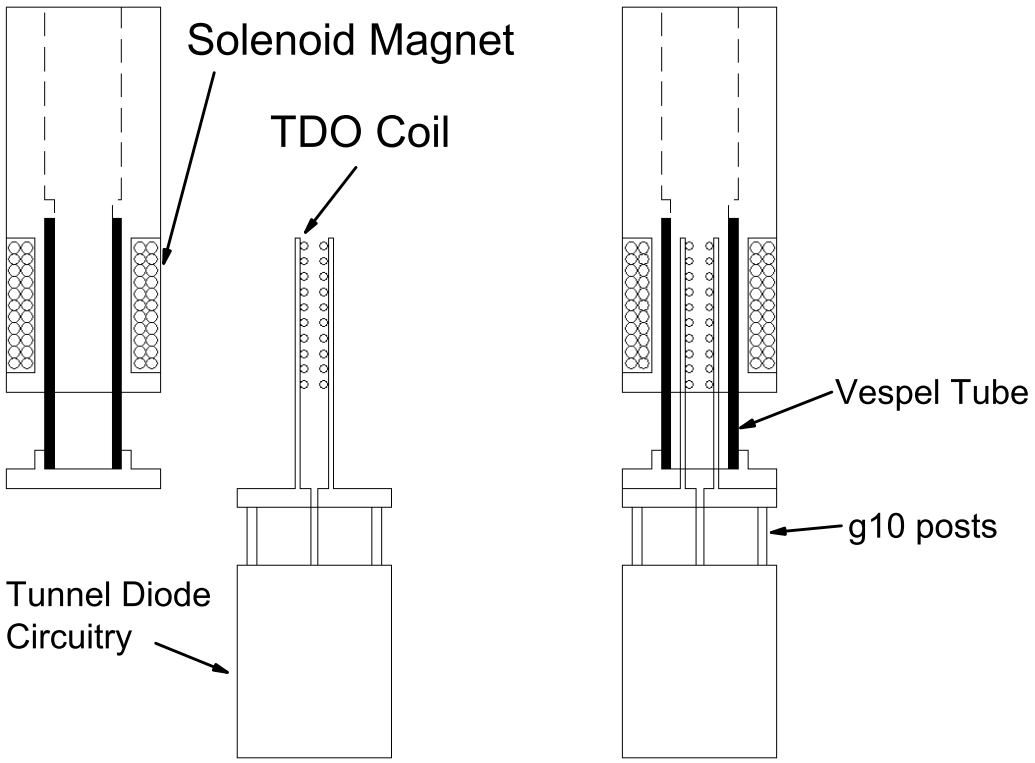


Figure 2.6: Basic setup of the experiment. One piece is responsible for housing the solenoid magnet and serves as a guide to align the sample holding sapphire rod and the tunnel diode oscillator (TDO) coil. The other piece contains the TDO coil and the TD circuitry, which are thermally isolated by insulating g10 rods.

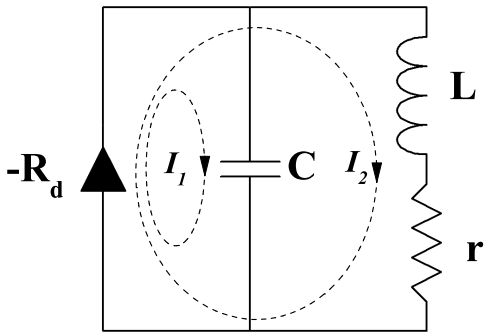


Figure 2.7: The tunnel diode oscillating circuit with a small loss element (r) associated with the inductor resistance.

2.3 Oscillator Circuit Theory

Although the tunnel diode circuit is relatively simple, only specific combinations of circuit elements result in a clean, oscillating signal. There are several good resources for determining the proper set of elements. Van Degrift's original paper describing this technique gives a set of ranges for each of the capacitor and resistor elements for a given tunnel diode resistance ($-R_d$) and hand wound coil used in the experiment.[34] Since the tunnel diode exhibits negative resistance, this will be denoted as $-R_d$ with the minus sign stated explicitly. The criteria is given in Table 2.1.

In order to characterize the oscillation of the circuit, the elements that make up the oscillator must be treated as non-ideal[35]. In other words, the quality factor, Q, will be assumed to be a finite value. This is accomplished by considering a non-ideal inductor that has some small resistance, r, in series. The circuit under consideration is shown as Fig. 2.7. If the AC voltage across the tunnel diode is defined as v_d, two Kirchoff loops and current conservation results in the following equations

$$\frac{I_1}{i\omega C} + v_d = 0 \tag{2.22}$$

$$I_2\left(i\omega L + r\right) + v_d = 0 \tag{2.23}$$

$$-\frac{v_d}{R_d} = I_1 + I_2 \tag{2.24}$$

In solving for I_1 and I_2 from the voltage loops and plugging the results into the current node equation, the following result is obtained

$R_p \approx \lvert R_d \rvert/4$	Prevents parasitic oscillation and yet does not disturb the fundamental oscillation
$R_2 \approx \lvert -R_d + R_p \rvert/4$	Properly biases the circuit yet does not waste power
$R_1 \geq \lvert R_d \rvert$ $\lvert R_d \rvert = 1000 \times 1/\omega_o C_2$	R_1 and C_2 are made large in order to isolate the circuit from room temperature sources of interference
$C_1 = C_2 \lvert R_d \rvert/100000 R_L$	This allows a few microvolts of signal to the initial room temperature amplifier with input resistance $R_L = 50\Omega$

Table 2.1: Suggested rules for tunnel diode oscillator components with reason for each rule.[34]

$$[LC]\,(i\omega)^2 v_d + \left[rC - \frac{L}{R_d}\right](i\omega)v_d + \left[1 - \frac{r}{R_d}\right] v_d = 0 \tag{2.25}$$

$$\frac{d^2 v_d}{dt^2} + \left[\frac{r}{L} - \frac{1}{R_d C}\right]\frac{dv_d}{dt} + \omega_o^2 \left[1 - \frac{r}{R_d}\right] v_d = 0 \tag{2.26}$$

The second expression represents the circuit equation of motion which naturally follows given that the tunnel diode voltage varies with time as $v_d(t) = v_d(\omega)e^{i\omega t}$.

The frequency can be found from the top expression using the quadratic formula, which results in the following

$$\omega = \sqrt{\omega_o^2\left(1 - \frac{r}{2R_d} - \frac{1}{4Q^2}\right) - \frac{1}{4C^2R_d^2}} + \left[\frac{r}{2L} - \frac{1}{2R_d C}\right] i \tag{2.27}$$

where $Q = \omega_o L/r$. As it turns out, the first term is the real part of the frequency and the second term is the imaginary part. This is true because the argument inside the square root is positive given the components ($\mathrm{R}_d \approx 1000\Omega$, $\mathrm{C} \approx 10^{-10}F$) and frequency ($\omega \approx 10^8$ rad/sec) associated with this experiment. Since Im ω is nothing more than the damping term for the circuit, the bracketed term must be negative for growing oscillation to occur. This amounts to

$$R_d < Q^2 r \tag{2.28}$$

Of course, the oscillations cannot continue to grow for all time. Once an equilibrium condition is met, the oscillation amplitude will stabilize giving a constant waveform. An approximate form for the IV characteristic near the reflection point is given by

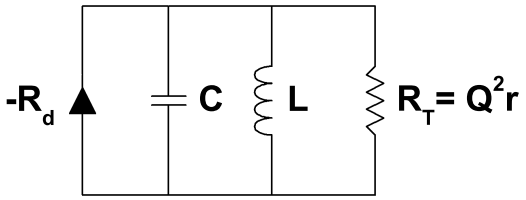


Figure 2.8: The actual circuit can be approximated as a circuit with a parallel tank resistance (R_T) that is equal to the product of the inductor resistance and the square of the quality factor.

$$i_d = -\frac{v_d}{R_d} + \beta v_d^3 \tag{2.29}$$

We then equate the power output of the tunnel diode with the power dissipated by the effective resistance of the tank circuit, R_T. This equivalent circuit is displayed as Fig. 2.8. A generic form for the tunnel diode voltage $v_d = V_o sin(\omega t)$ is plugged into this power constraint, leaving an easy calculation for the amplitude

$$\int_0^{2\pi/\omega} v_d i_d dt = -\int_0^{2\pi/\omega} \frac{v_d^2}{R_T} dt \tag{2.30}$$

$$V_o = \sqrt{\frac{4}{3\beta}\left(\frac{1}{R_d} - \frac{1}{R_T}\right)} \tag{2.31}$$

2.4 Calibration

Since the analysis above applies for a sample that is free floating in the middle of a coil, some corrections need to be added for the actual setup used. As explained earlier, the sample was placed on a sapphire rod which was inserted into the coil. Although sapphire is almost ideal given it is mostly unaffected by temperature and field changes, these small frequency shifts can come into play for sensitive measurements. It should also be mentioned that two different sapphire holders were used in order to explore the anisotropy of samples. The *parallel* and *perpendicular* holders are shown in Fig. 2.9. A set of calibration runs were performed for both the parallel and perpendicular holders with no mounted samples. The temperature dependence for each holder is given in Fig. 2.10. Notice that the total change in frequency for a temperature sweep of the rod is on the order of 0.1 Hz, which is well within the inherent drift of this type of setup. However, if a feature were to emerge at low temperatures on the order of 1 Hz, this background would have to be subtracted from

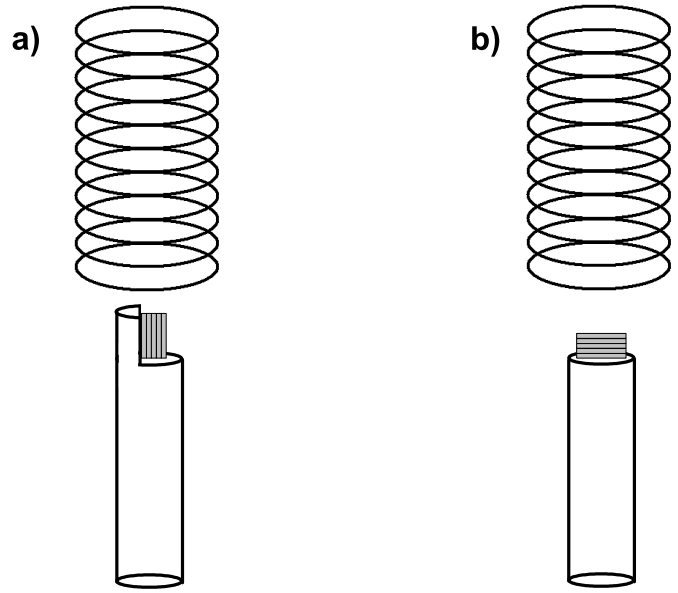


Figure 2.9: The a) parallel and b) perpendicular holders. These names refer to the orientation of the magnetic field induced supercurrents relative to the conducting planes of the 2D sample.

the data.

There is another piece of information associated with the sapphire rod that is absolutely necessary. For reasons that will be discussed later, the total frequency shift that results from taking the sapphire out of the coil is needed in order to properly convert frequency data into changes in penetration depth. This is shown in Fig. 2.11 for both holders. This is accomplished through a spring/pulley system. Even though this material is only weakly paramagnetic, the shift is comparable to that of the sample due to the relatively large size of the sapphire rod compared to the mm^3 samples.

In addition to characterizing the affects of the sapphire, the coil itself required calibration. Looking at Eqn. 2.19, the coil volume is needed in order to relate frequencies to penetration depth. The coil volume can be found by running a sample of known penetration depth and demagnetization at low temperature. In light of this, an indium sphere was examined. The diameter of the sphere was obtained through the use of an optical microscope and a fine scale ruler capable of discerning widths of $\sim$10 μm. Since the sphere radius is much larger than the penetration depth, Eqn. 2.19 simplifies to

$$f_s(0) - f_{ec} = \frac{f_{ec}}{2V_c}\frac{V_s}{1 - N_{sph}} = \frac{3}{2}gV_s \tag{2.32}$$

where $N_{sph} = 1/3$ accounts for the demagnetization associated with a spherical geometry and $g \equiv f_{ec}/2V_c$ contains the coil volume. In order to find g, the sample volume is needed as well as the frequency shift associated with pulling the indium sphere (at 0K) out of the coil, as shown in Fig. 2.12. It is important to

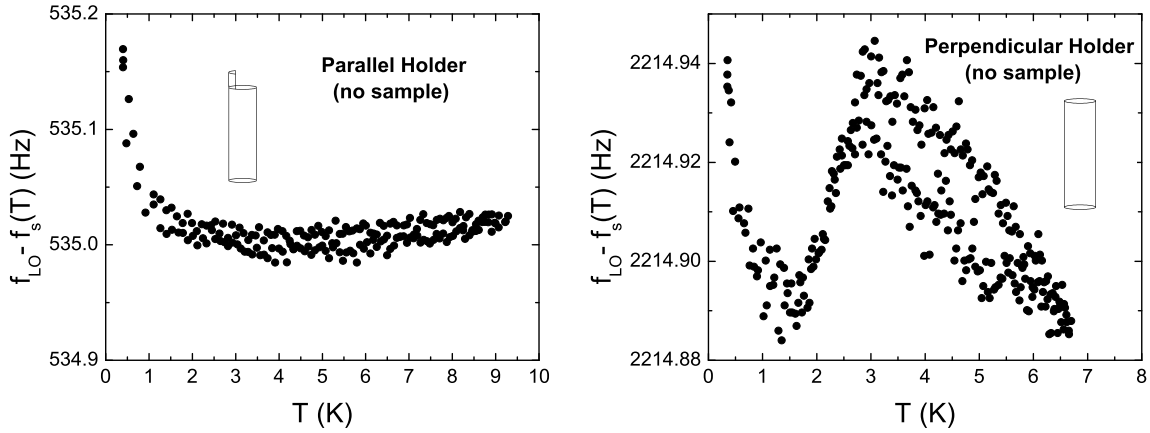


Figure 2.10: The frequency shift associated with ramping the temperature of each sapphire rod in the absence of a sample. The total shift is roughly 0.1 Hz, which is small compared to the total shift of the typical sample.

note that the sapphire shift must be added for reasons mentioned previously. The result of the calibration was $g = 1.16 \times 10^{-4} Hz/\mu m^3$, which was a useful quantity during data analysis.

The last calibration issue is associated with the solenoid and Helmholtz magnets. Although the sapphire is mostly unaffected by these fields, the oscillator coil itself experiences a change in inductance with increased field. An example of this magnetic field background is recorded in Fig. 2.13. Since the frequency can change up to 50 Hz, this shift must be subtracted from all data taken in a magnetic field.

2.5 Frequencies

One advantage of the tunnel diode technique is that the data does not depend on signal amplitude. The problems associated with voltage measurements include impedance mismatches, contact resistance, and other forms of loss that can greatly compromise the accuracy of the data. In this experiment, the useful data comes in the form of frequency changes of an LC oscillator. One difficulty is locating the frequency associated with the oscillator. This was accomplished using a spectrum analyzer and a Marconi frequency synthesizer. The purpose of the synthesizer was to set the proper frequency center and window on the spectrum analyzer. Given the capacitance value and coil dimensions, the oscillation was expected to occur in the vicinity of 10 MHz. Once the analyzer was properly set up, the tunnel diode voltage was slowly increased until a frequency peak emerged. In order to find the peak more easily in future runs, the voltage range that resulted in oscillation was recorded. The tunnel diode voltage was scanned up and back down through the oscillation transition due to the fact that the voltage window was hysteretic.

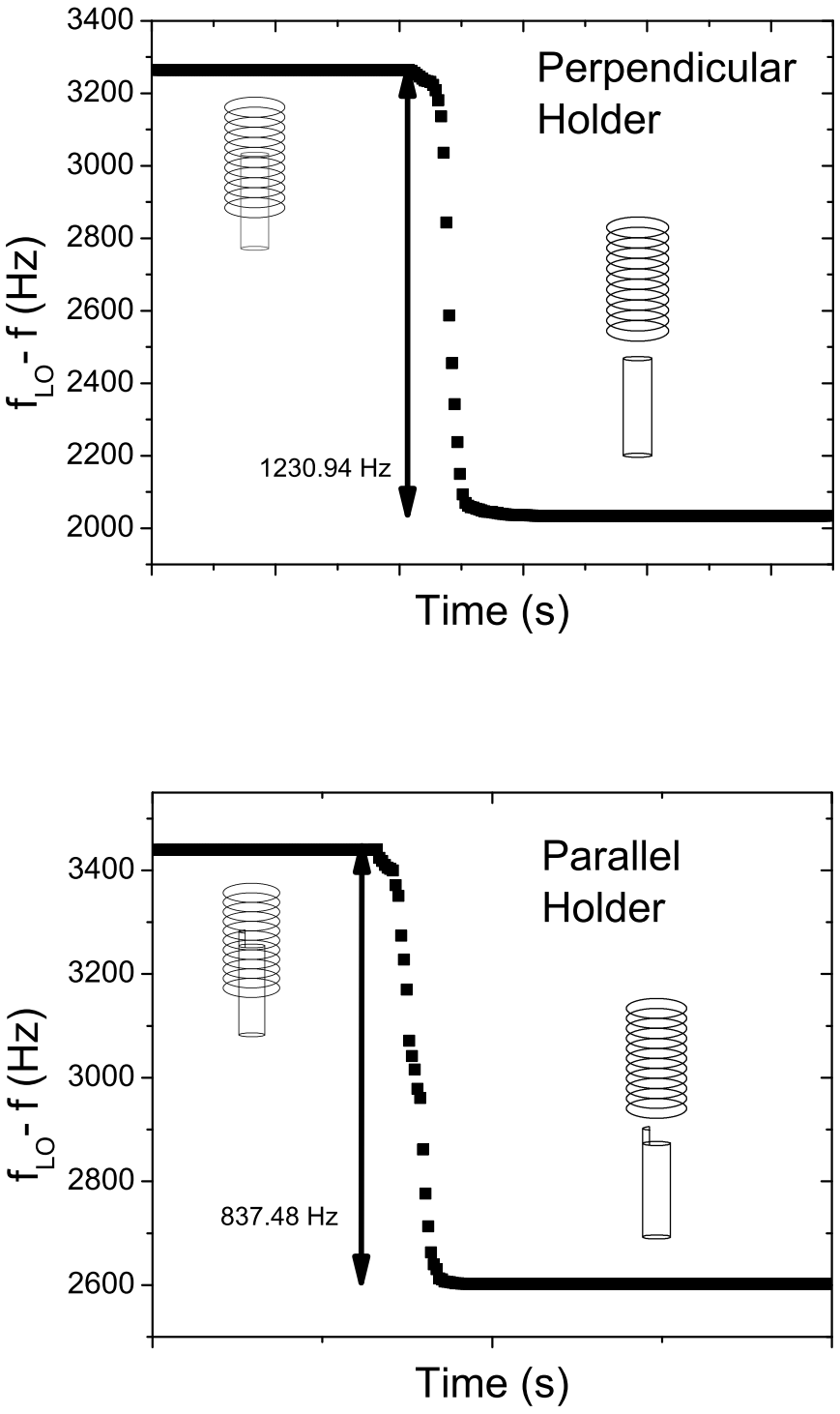


Figure 2.11: The frequency shift associated with pulling the bare sapphire out of the coil for both the perpendicular and parallel holders.

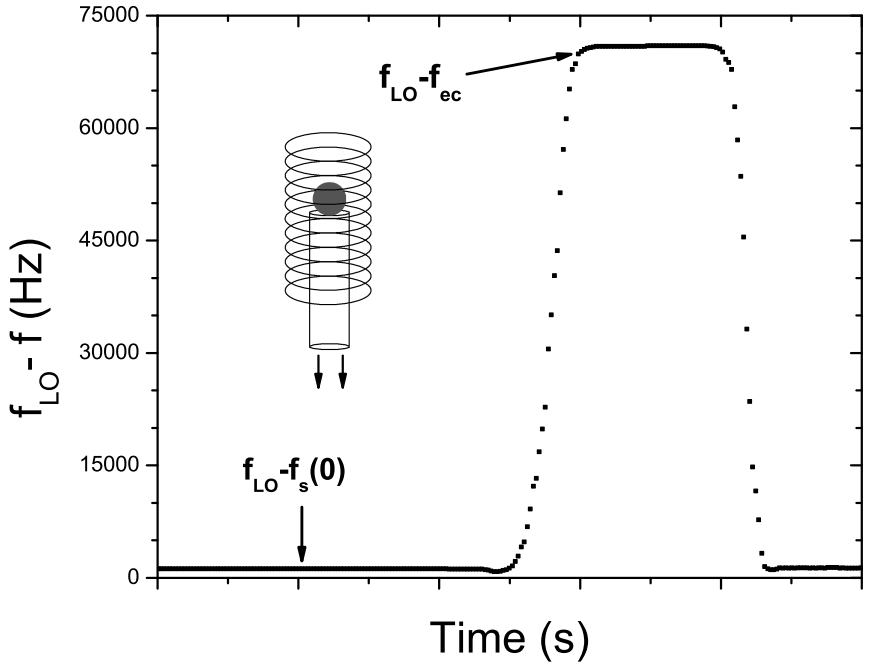


Figure 2.12: The frequency shift associated with pulling the indium sphere out of the coil.

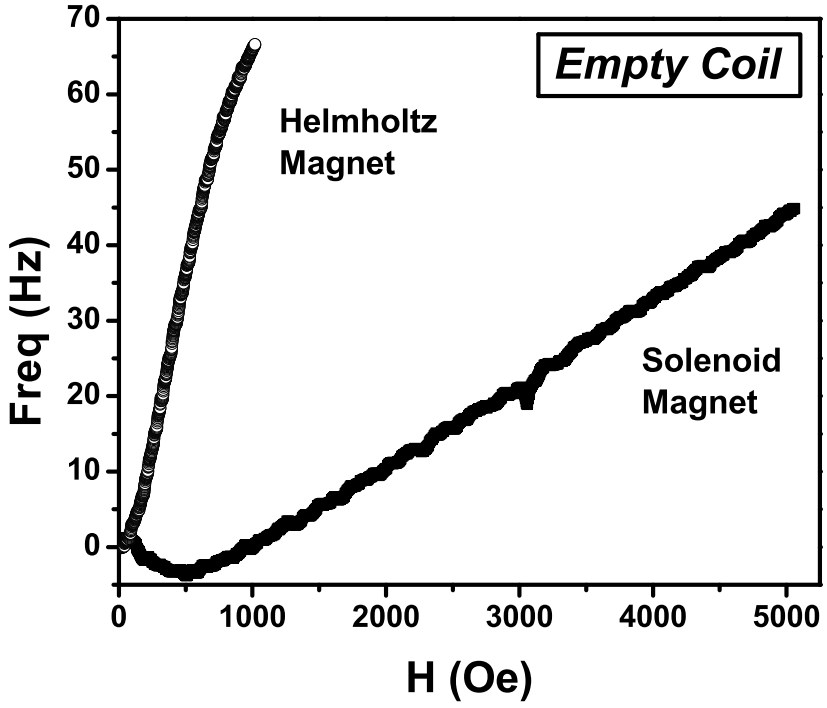


Figure 2.13: The frequency shift associated with ramping the magnetic field with the sample out of the coil

The raw data for this experiment is a noisy AC voltage in the MHz range. Therefore, some care must be taken to properly filter and collect the frequency data. In order to properly filter the signal received from the oscillator, the AC voltage is amplified and sent to a mixer. Using a Marconi frequency synthesizer as a reference in the vicinity of the signal frequency, the mixer outputs a wave with a frequency equal to the difference between the Marconi and the raw signal from the oscillator, which is typically in the range of 11-13 MHz. The reference frequency output by the Marconi is called the local oscillator frequency (f_{LO}). This resulting wave is then passed through a band filtered preamp and is finally measured by an HP Universal counter. Bandwidth reduction was used to filter out noise with frequencies close to the oscillator signal.

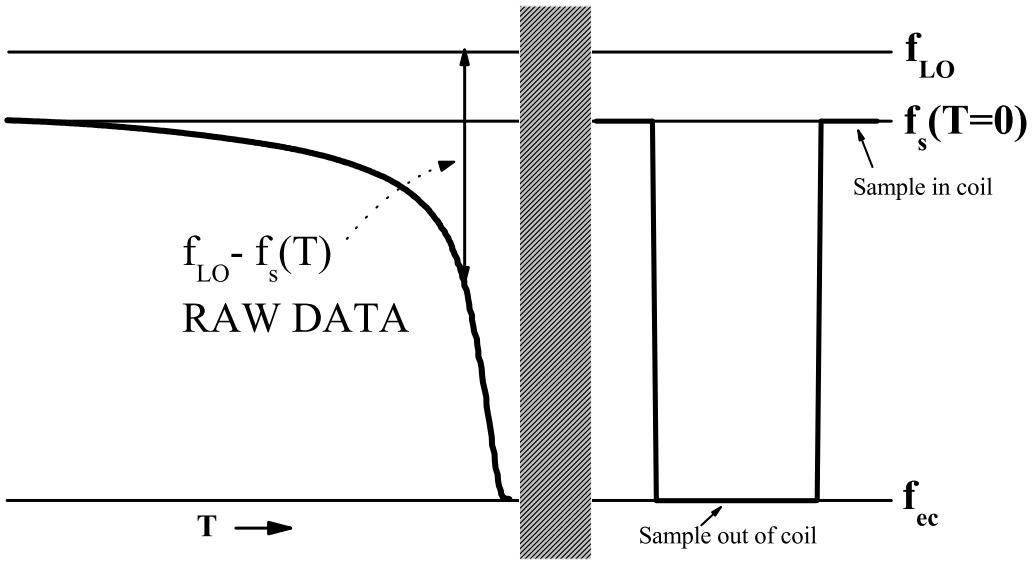


Figure 2.14: A plot of all relevant frequencies connected to the experiment. The left side shows the raw data for increasing temperature. The right side depicts a typical pullout frequency shift. This picture only holds for the absence of the sapphire rod.

Since this experiment is overloaded with reference, background, sample, and shifts in frequency, it was useful to make a plot relating all of these quantities. An example of the temperature sweep and pullout data are given in Fig. 2.14. Since the analysis depends on the frequency shift $f_s(T) - f_s(0)$, this quantity will be renamed $\Delta f_s(T)$ for short. The f_{LO} is set higher than the highest possible LC resonance. This corresponds to the situation where the data grows with increasing temperature, similar to the behavior of the penetration depth. As described earlier, the raw data represents the difference between the local oscillator frequency and the absolute resonance of the LC circuit. Since higher temperatures result in the sample becoming less diamagnetic, the resonance decreases due to the fact that the inductance of a coil increases as the coil volume becomes more paramagnetic. In other words, as the temperature increases, the volume of the coil effectively increases. Eqns. 2.14 and 2.18 indicate that the absolute frequency of the oscillator should decrease as a

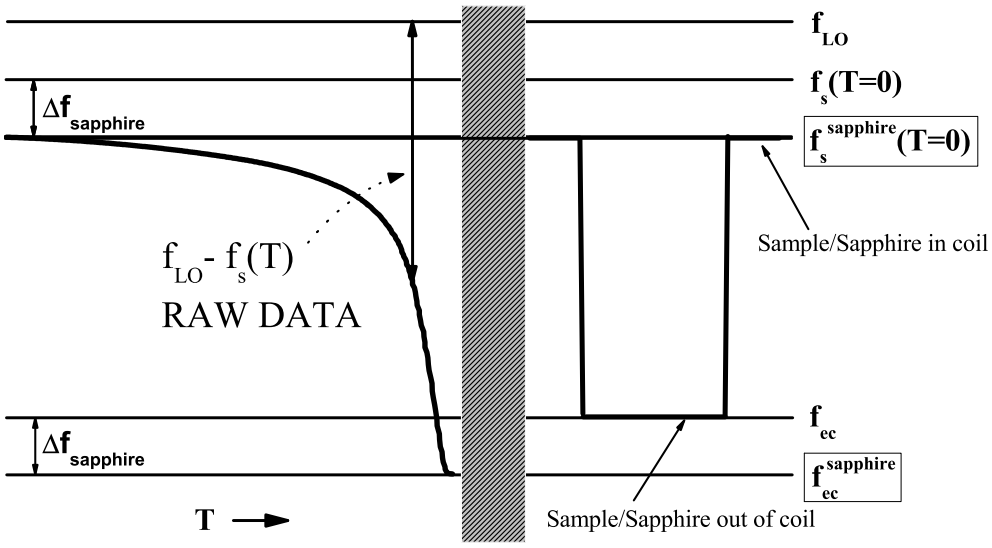


Figure 2.15: A plot of all relevant frequencies accounting for the sapphire holder. The temperature sweep data on the left side is entirely shifted down by $\Delta f_{sapphire}$, whereas the pullout data on the right is only shifted before the sample/sapphire is pulled out.

result. It again must be noted that the picture given in Fig. 2.14 is that of a free floating sample that can be pulled in and out of the coil. In reality, there is a sapphire rod that has a frequency shift ($\Delta f_{sapphire}$) associated with it. The real situation is shown in Fig. 2.15. Although the empty coil and local oscillator are fixed values, the presence of the sapphire in the coil during temperature sweeps effectively shifts the raw data down an amount equal to $\Delta f_{sapphire}$. For the case of the pullout data, the shift only exists as long as the sample remains in the coil.

2.6 Penetration Depth from Raw Data

Although the relationship between the raw data and penetration depth is technically an infinite sum, a common practice is to choose sample dimensions that collapse the expression to the form

$$\frac{f_s(T) - f_{ec}}{f_{ec}} = \frac{1}{1-N}\frac{V_s}{2V_c}\left(1 - \frac{2\lambda(T)}{D}\tanh D/2\lambda(T)\right) \tag{2.33}$$

where D is a function of the sample geometry. For example, $D \to d$ for thin samples in a parallel field. Unfortunately, determining the sample volume is relatively difficult for irregularly shaped samples. In addition, the demagnetization factor for a finite-slab sample in a perpendicular field does not have an analytic expression. A solution to these problems was obtained by modifying the original apparatus so that the sample could be pulled out of the coil and the corresponding pullout frequency (Δf_p) was measurable.

In pulling the sample out of the coil at the lowest possible temperature, the observed frequency shift is equivalent to this expression evaluated at 0 K. In the reasonable limit that $D >> \lambda(0)$

$$\Delta f_p = f_s(0) - f_{ec} = \frac{gV_s}{1-N} \tag{2.34}$$

In other words, the quantities responsible for the largest error can be measured directly *in situ*.

The frequency shift related to the change in penetration depth is $\Delta f_s(T) = f_s(T) - f_s(0)$. Since tanh(x)$\rightarrow$ 1 for $x \geq 2$, one can show that changes in penetration depth are proportional to $\Delta f_s(T)$

$$\Delta f_s(T) = [f_s(T) - f_{ec}] - [f_s(0) - f_{ec}] = [f_{LO} - f_s(0)] - [f_{LO} - f_s(T)] \tag{2.35}$$

$$\Delta f_s(T) = \Delta f_p \left[1 - \frac{2\lambda(T)}{D} \tanh \frac{D}{2\lambda(T)}\right] - \Delta f_p \left[1 - \frac{2\lambda(0)}{D} \tanh \frac{D}{2\lambda(0)}\right] \tag{2.36}$$

$$\lambda(T) - \lambda(0) = \frac{D}{2\Delta f_p}[f_s(0) - f_s(T)] \qquad D >> \lambda \tag{2.37}$$

In order to obtain the best possible value of $f_{LO} - f_s(0)$, the raw frequency data was extrapolated to 0 K. The conversion of raw data into penetration depth is given in Fig. 2.16.

2.7 Cryostat

All experiments were performed on a ^{3}He evaporation cryostat. Temperatures as low as 380 mK could be reached when running optimally. The operation of the cryostat is displayed in Fig. 2.17. Through the use of a thin capillary, liquid ^{4}He was siphoned into a small chamber called the 1K pot. This small puddle of ^{4}He was pumped on, causing the chamber to cool to roughly 1.5 K through evaporative cooling. While this was taking place, ^{3}He gas was pushed down a tube that is heat sunk to the 1K pot, causing the ^{3}He to condense and collect in a separate chamber called the ^{3}He pot. This pot was also pumped using a separate circulating pump, in order to recycle this precious isotope. The front end of the ^{3}He lines was pumped with the aid of a water cooled booster to maximize the pumping speed and reach the lowest possible temperatures. The experiment was in thermal contact with the ^{3}He pot via a copper heat link.

In cooling down, the use of exchange gas was necessary due to the large heat capacity of the experiment and cooling stages. The cool down from 300 K to 77 K took roughly 6-8 hours using a nitrogen gas pressure of about 100 Torr. When liquid nitrogen temperatures were reached, a round of leak checking was administered. If no leaks existed at 77 K, a small amount of ^{3}He exchange gas was placed in the can and the experiment was cooled to 4.4 K.

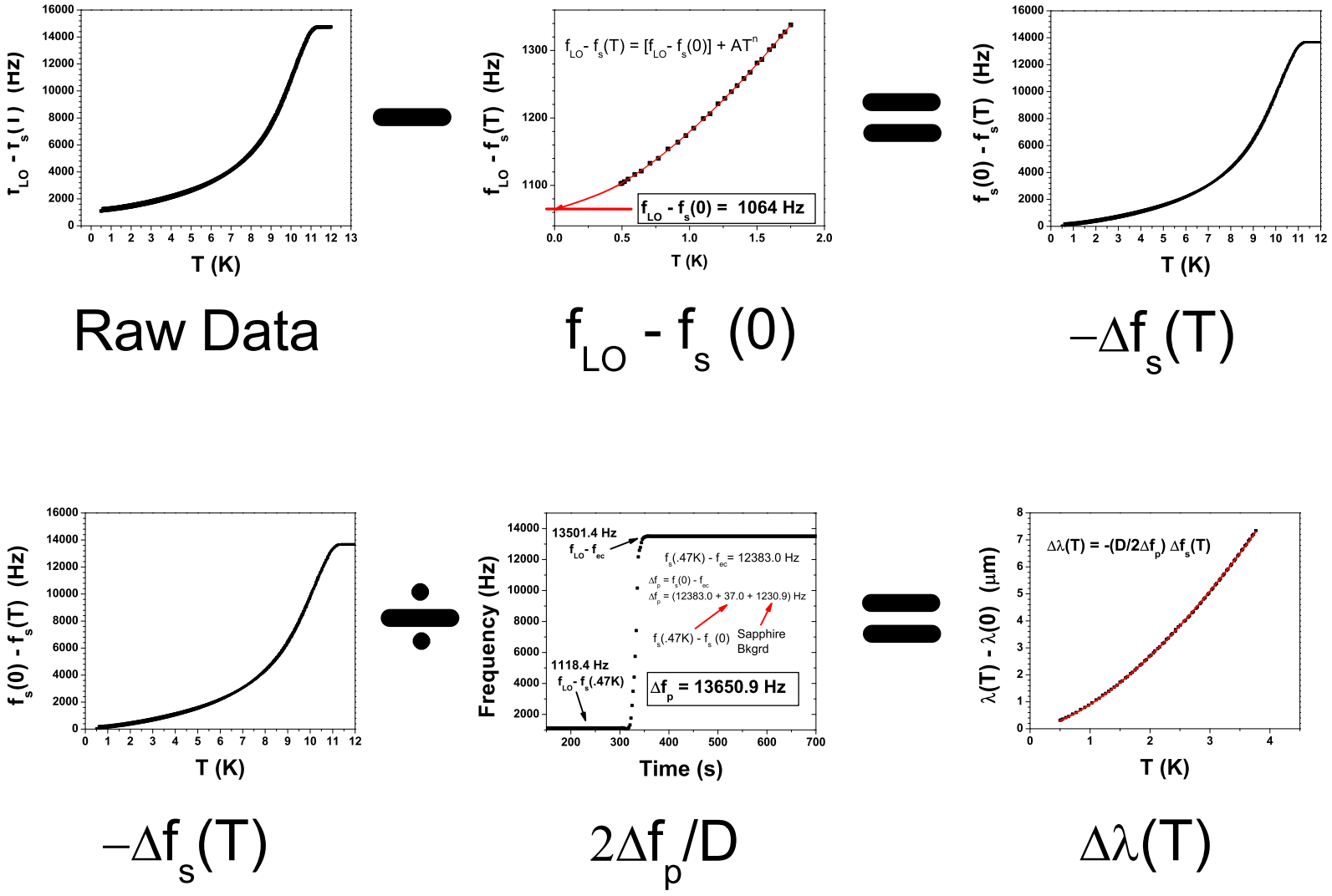


Figure 2.16: A flow chart for the conversion of raw data into penetration depth. The D quantity is a characteristic length dictated by the sample geometry and field orientation

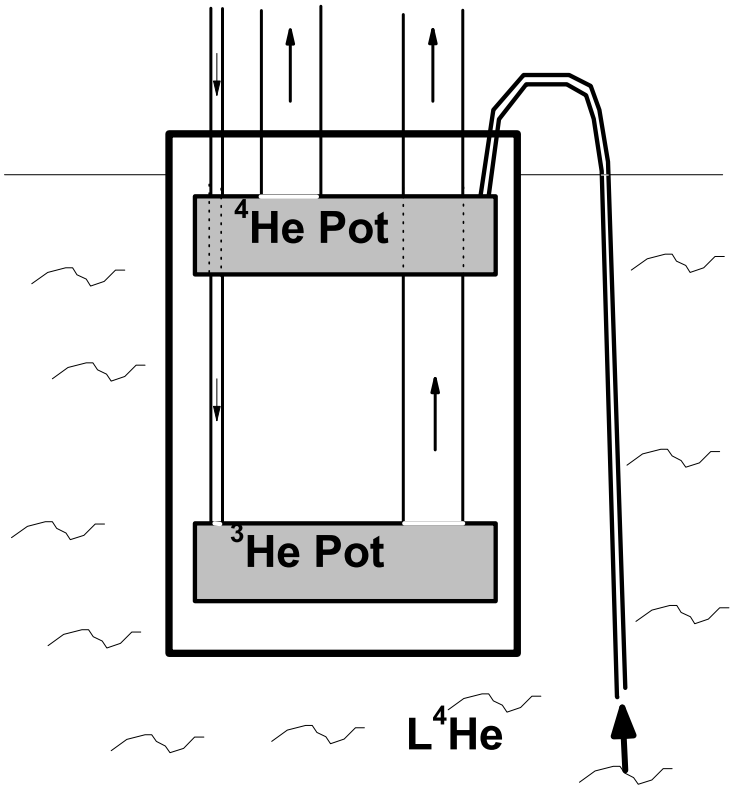


Figure 2.17: The basic operation of a ^{3}He cryostat. The 1K pot siphons liquid ^{4}He from the bath via a thin capillary. A thin tube carrying gaseous ^{3}He is heat sunk to the 1K pot, causing the gas to condense and drip into the ^{3}He pot. Both pots are pumped on, resulting in evaporative cooling. NOTE: The two thin tubes are well chosen flow impedances to optimize cooling.

Of course, residual exchange gas could act as a heat leak from the external ^{4}He bath. This problem was minimized using a charcoal cryopump that was weakly heat sunk to the ^{4}He bath via a fiberglass g10 post. While cooling to 77 K and then to 4 K, the charcoal trap was kept warm by resistive heating with 400 mW of power. After reaching 4 K, the bulk of the exchange gas was pumped out of the can using a diffusion pump. The power supplied to the charcoal trap was then turned off, resulting in the trap collecting the rest of the lingering gas, due to the fact that charcoal has a large surface area to volume ratio.

Magnets were mounted to provide both an axial and perpendicular DC field. Typically, cryostats have cans that are able to slide inside of a superconducting magnet that is placed directly in the ^{4}He bath. However, variable magnetic fields on the order of a 5000 G can significantly alter the state of the tunnel diode circuitry. It is because of this fact that a hand wound solenoid coil was made on the cylinder that surrounds the sample coil to minimize the field exposure of the tunnel diode and accompanying capacitors. This is shown in Fig. 2.6. NbTi wire was used in constructing the solenoid.

With an axial magnet in place, the next logical step was to design a magnet that could provide a field perpendicular to the solenoid field. With the tunnel diode's sensitivity to field in mind, a small Helmholtz coil was built and mounted just outside the solenoid magnet. The only limitation was the spacing between the coils, which was set by the diameter of the solenoid magnet immediately surrounding the sample coil.

The magnets were calibrated using a small Hall probe. Not only was it used to determine the field to current ratio at the center of the magnet, but it was also used to determine the uniformity of the field. Although solenoid coils are familiar and expected to provide reasonable uniformity, its hard to have a good intuition concerning a pair of separated coils. As it turns out, Helmholtz coils produce a relatively uniform field depending on the spacing between the two coils, which is known as the Helmholtz spacing. The uniformity is greatest when the Helmholtz spacing is equal to the radius of one of the coils[36]. Using the Biot-Savart law on a single loop, it is easy to show that the change in slope of B_z is minimum at this location. The field to current ratio for the Helmholtz magnet was 213 G/A and the solenoid magnet was 1300 G/A.

The last thing to consider was the method of heat sinking the magnet wiring. In the typical configuration, the superconducting magnet is outside of the can in the ^{4}He bath. Effectively, this provides a built in heat sinking situation where all of the magnet leads are constantly at 4K. However, this experiment involves two magnets inside the can. It would be extremely inconvenient to have the magnet leads extend from the coils to the outside of the can because magnet detachment would require cutting the magnet leads. Rather, it was more convenient to have the magnet leads detach inside the can. Therefore, a solder connection between the magnet leads and the wire coming into the can from the bath was needed. Since this joint represents the weakest point between the magnet and power supply, special care was taken to properly heat sink this

connection to the ^{4}He bath. A thin layer of mylar film was wound around a copper rod bolted to the 4 K cryostat can. Four separated strips of copper tape were laid on top of the mylar, creating four zones (two zones per magnet) where internal and external magnet wires could be soldered and heat sunk properly.

Chapter 3

Penetration Depth

3.1 Superconductivity

3.1.1 History

When first discovered in 1911, the idea of zero resistance materials captured the imagination of the science community. In fact, the first four decades were spent searching and characterizing new materials in the absence of any real understanding of how superconductivity worked on a microscopic level. Although many contributed, the London brothers made the first phenomenological model that is still used today[37]. In the 1950's, some important theories came to light that are still widely used today. Ginzburg and Landau presented a phenomenological model that introduced a carrier wavefunction with a characterization length named the coherence length.[38]. Its primary shortcoming was that it was not a microscopic theory of superconductivity and was originally formulated in the limit of temperatures approaching the critical temperature (T_c) where the material transitions from a normal metal to a superconductor. In 1957, there was a break through. Bardeen, Cooper, and Shreiffer (BCS) formulated the first microscopic model of superconductivity that was valid for all temperatures[1]. Although many of the more recent materials deviate from the behavior described in the BCS theory, it is the standard by which all data is analyzed and reported to the science community.

3.1.2 Mechanism

The heart of the BCS theory lies in the interaction of the electrons in the system. Under normal conditions, electrons repel one another due to the Coulomb force. One would expect that any interaction of two electrons in a material would result in separation. However, some scenarios do exist where the electrons will attract one another. According to the BCS model, an attractive potential is essential in pairing up the electrons into what is known as Cooper pairs. Using the lattice as an intermediary, an electron can momentarily attract enough positive ion cores to create a positively charged region capable of attracting another electron. The

lower energy state associated with this attraction is referred to as the condensate. This mechanism was later confirmed experimentally in the discovery of the isotope effect in various isotopes of Mercury[39,40]. It was discovered that the critical temperature (T_c) and field (H_c) were shown to depend on the mass of the positive ions using a variety of isotopes for a given material. In any introductory textbook in superconductivity, it can be shown that $\Delta(0) \propto k_B T_c \propto \hbar\omega_{Debye} \propto M^{-1/2}$, where M is the isotope mass and ω_{Debye} is the Debye frequency. This relation shows a link between the superconducting state and phonons propagated by the ions that make up the lattice.

Although this phonon mediated attraction was postulated as the reason for Cooper pairing, it turns out this mechanism may not always be responsible for pair formation. In the case of high temperature superconductors (HTSC), the observed critical temperatures far exceeded the theoretical limits calculated from a phonon mediated mechanism[4]. Another possible source of attractive interaction is associated with the magnetic moment of the spins. The fact that the organic superconducting materials appear to host superconducting and antiferromagnetic phases makes it a strong candidate for non-phonon mediated attraction[41].

3.1.3 Superconducting Gap

The BCS theory originally assumed a superconductor whose gap is independent of wave vector ($\vec{k}$). In other words, the gap was assumed to be a spherical shape with no nodes. Unlike traditional BCS superconductors, these organics are suspected of having a gap with d-wave symmetry. In the case of a d-wave system, there are directions in k-space that have zero gap, namely along the diagonals where $k_x = k_y$. A picture of the d-wave gap function is shown in Fig. 3.1. As one can see, the phase of the order parameter alternates from positive to negative upon rotation in k-space, making these unconventional superconductors due to the fact that the gap displays less symmetry than the lattice.

As one can imagine, this gap symmetry manifests itself in unambiguous ways in a variety of measurements. The quasi two-dimensional κ-$(ET)_2$X organic conductors resemble the copper oxides in several ways[42,43,44]. Copper oxide superconductors were definitively shown to pair in a state of d-wave symmetry by the Van Harlingen group[45]. Although some experiments have claimed s-wave pairing[12] in κ-$(ET)_2$X superconductors, penetration depth[13,14,15], NMR[21,22], thermal conductivity[16,17], specific heat[18,19] and STM[20] experiments all provide strong support for nodal quasiparticles and d-wave pairing.

The Fermi surface of these materials can be understood by examining the structure of κ-$(ET)_2$X superconductors, as given in Fig. 3.2 and 3.3. In short, the superconductor is made up of alternating conducting and insulating planes. The ET molecules provide the electrons that make up conducting sheets separated by the insulating polymeric anions. The superconducting electrons are supplied by the central C-C bond of the

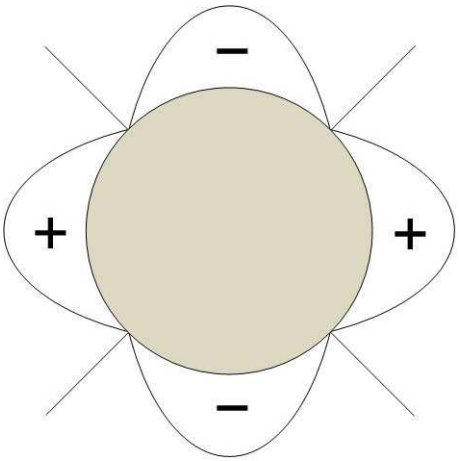


Figure 3.1: Picture of the d-wave superconducting gap in k-space.

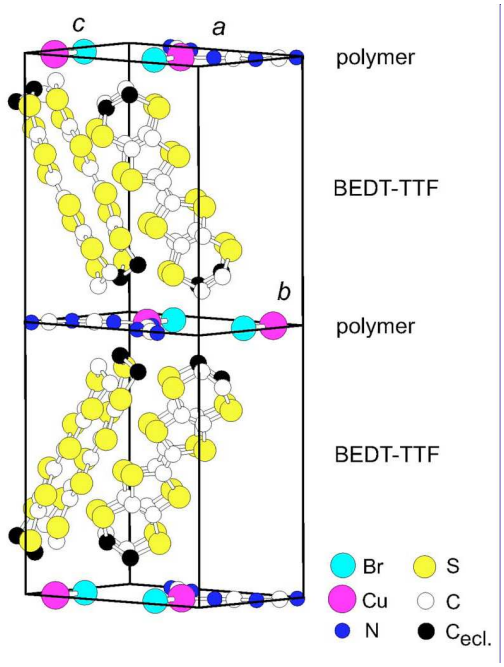


Figure 3.2: The structure of κ-$(ET)_2$-Br consists of ET molecule pairs that are separated by insulating polymers. The terminating ethylene groups are depicted in the eclipsed formation.

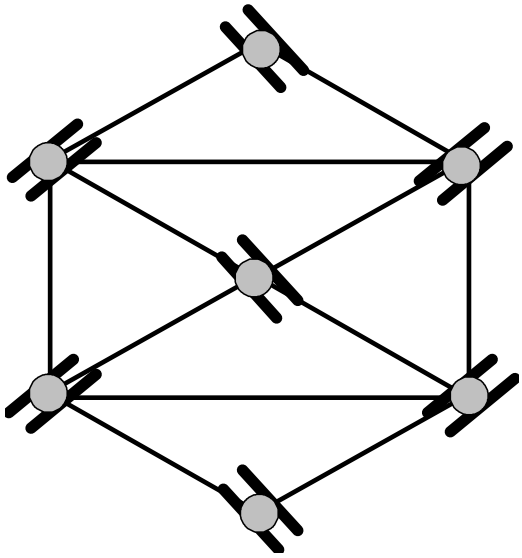


Figure 3.3: The ET molecules pair up into dimers that have a κ configuration with respect to each other.

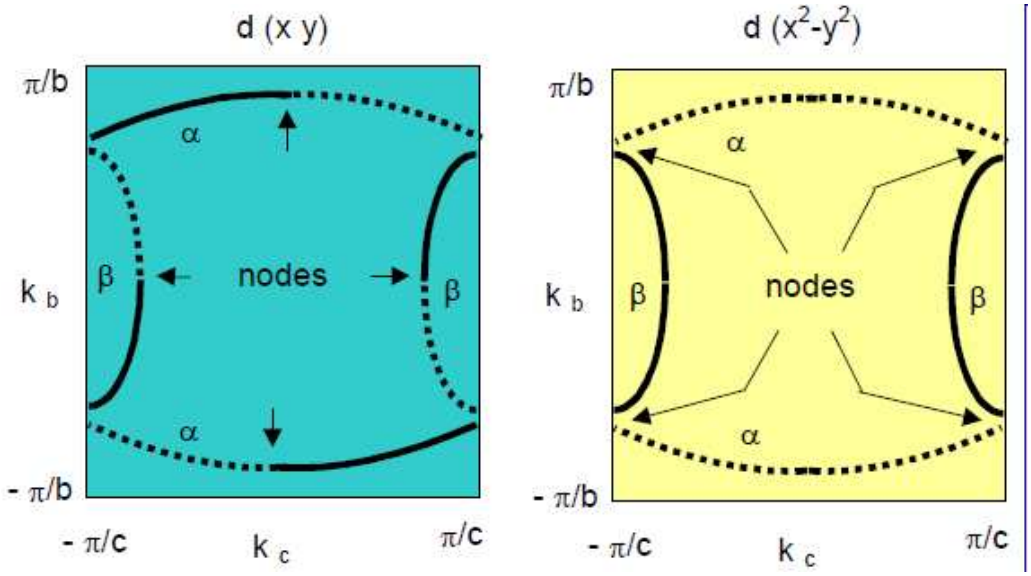


Figure 3.4: Two portions of the Fermi surface in κ-$(ET)_2$X superconductors. The location of the proposed nodes in the superconducting gap are shown. Reprinted with permission.[46]

ET molecules. Each dimer contributes one electron to the conducting layer with each unit cell containing two dimers. For the case of κ-$(ET)_2$Cu[N(CN)$_2$]Br pictured in Fig. 3.2, the anions are $Cu[N(CN)_2]Br^-_\infty$. From Fig. 3.3, note that the ET molecules appear to pair up into dimers. According to Kuroki *et al.*, the proposed node locations for d_{xy} and $d_{x^2-y^2}$ are pointed out on the Fermi surface of a κ-$(ET)_2$X superconductor[46]. Both are shown in Fig. 3.4. Although the majority of experimental studies have pointed to a nodal gap with NMR measurements indicating a gap that must be spin-singlet[21,22], little work has been done to determine the location of the nodes. Although magneto optical absorption measurements[47] indicate d_{xy}, STM[48] and thermal conductivity[17] techniques indicate $d_{x^2-y^2}$. If the $d_{x^2-y^2}$ picture is correct, Kuroki concludes that dimerization would have to be weaker than previously thought. If true, these findings would cast doubt on the widespread belief that spin fluctuations are the underlying mechanism in these materials. This is due to the fact that weak dimerization would rule out the assumption that the four bands (that result from the four molecules per unit cell) can be treated as a two band system, which is crucial to the spin fluctuation picture. For the sake of clarification, the weak dimerization limit corresponds to the situation where tunneling between two ET molecules withing a dimer pair is comparable to tunneling between two different dimers. Although penetration depth measurements are not capable of detecting the phase of the nodes, non-zero quasiparticle densities at low temperatures manifest themselves in measurements of λ.

3.2 Penetration Depth

Penetration depth measurements can be used to answer a host of questions. A thorough review of penetration depth measurements was recently completed by Prozorov *et al.*[49]. This technique can be used to examine dual gap superconductors, the nonlinear Meissner effect, both in-plane and interplane transport, and the coexistence of superconductivity and magnetism to name a few[50,51,13,30,52]. Therefore, penetration depth behavior provides a wealth of information that is helpful in properly characterizing superconducting materials. Before describing specific experiments and results, some basic concepts concerning the history and behavior of the magnetic penetration depth must be established.

3.2.1 London Equations

Long before the BCS theory came on the scene, physicists attempted to explain the two unique characteristics of superconductors. Although a zero resistance conductivity state was the startling phenomenon that drew attention to these materials, it took another 20 years before perfect diamagnetism was discovered by Meissner. The first phenomenological model used to explain these two properties was proposed by the

London brothers[37]. Starting with the Drude model

$$m\frac{d\mathbf{v}}{dt} = e\mathbf{E} - \frac{m\mathbf{v}}{\tau} \tag{3.1}$$

the first London equation can be derived assuming that superconducting carriers do not scatter, which would result in the observed perfect conductivity. The consequence of this assumption is an infinite time between scattering events (τ). This gives

$$\frac{d\mathbf{J_s}}{dt} = \left(\frac{1}{\mu_o\lambda^2}\right)\mathbf{E} \tag{3.2}$$

$$\lambda \equiv \sqrt{\frac{m}{\mu_o n_s e^2}} \tag{3.3}$$

where n_s is the density of superconducting electrons. The variable λ turns out to represent the length scale by which a magnetic field penetrates a superconductor. Although Eqn. 3.2 describes the perfect conductivity aspect of superconductivity, the second London equation is needed to explain the total expulsion of magnet fields from the bulk. This is known as the Meissner effect. The second London equation is

$$\mathbf{H} = -\lambda^2\left(\nabla \times \mathbf{J_s}\right) \tag{3.4}$$

Taking the curl of the Maxwell equation $\nabla \times \mathbf{H} = \mathbf{J}$ and using Eqn. 3.4, we get an expression for the field

$$\nabla^2\mathbf{H} = (1/\lambda^2)\mathbf{H} \tag{3.5}$$

The solution to this differential equation is an exponential decay of $\mathbf{H}$ within a characteristic length λ. This is known as the London penetration depth. The temperature dependence of λ reveals important information concerning the gap of the material.

3.2.2 Penetration Depth Behavior: High T

In the early years of superconductivity, the penetration depth in different materials was observed to fit the following empirical temperature dependence

$$\lambda(T) = \frac{\lambda(0)}{\sqrt{1-(T/T_c)^4}} \tag{3.6}$$

Using a two fluid model to describe the thermodynamics of superconductivity, Gorter and Casimir were able

to derive this temperature dependence of λ near T_c. In recent decades, more exotic types of superconductivity have been discovered, that require a slight modification in the power of the reduced temperature (T/T_c). For example, samples with d-wave gap symmetry empirically obey[49]

$$\lambda(T) = \frac{\lambda(0)}{\sqrt{1-(T/T_c)^{4/3}}} \tag{3.7}$$

Whatever the case, the Gorter-Casimir equation continues to be used as a good first approximation to the zero temperature penetration depth $\lambda(0)$, but has no microscopic justification.

Fifteen years passed before Ginzburg and Landau (GL) would publish a macroscopic model of superconductivity in the limit $T \approx T_c$. Whereas the London model assumed a uniform density of superconducting electrons, the GL theory introduced a pseudowavefunction ($\psi(r)$) for the superconducting electrons. According to the theory, $\psi(r)$ was allowed to vary with position, giving a nonuniform density. In order to find the functional form of this order parameter, GL postulated a free energy:

$$F = F_n + \frac{\mu_o H^2}{2} + \alpha|\psi|^2 + \frac{\beta}{2}|\psi|^4 + \frac{1}{2m^\star}|\left(-i\hbar\nabla - e^\star\mathbf{A}\right)\psi|^2 \tag{3.8}$$

where the first two terms represent the normal state free energy and the remaining three correspond to the superconducting state in the limit that ψ is small and varies slowly in space, both of which hold near T_c. For clarity, $m^\star$ and $e^\star$ represent the mass and charge of the superconducting carriers and α and β are parameters. Since the vector potential ($\mathbf{A}$) and ψ are unknown, the variational method was used to minimize the free energy with respect to these two parameters. This results in the two Ginzburg-Landau differential equations:

$$\alpha\psi + \beta|\psi|^2\psi + \frac{1}{2m^\star}\left(-i\hbar\nabla - e^\star\mathbf{A}\right)^2\psi = 0 \tag{3.9}$$

$$J = \frac{e^\star}{m^\star}|\psi|^2\left(\hbar\nabla\phi - e^\star\mathbf{A}\right) \tag{3.10}$$

This theory not only predicts a specific form of $\lambda(T)$ near T_c, but it is incredibly useful in calculating the coherence length (ξ) and determining whether any given superconductor is Type I or Type II in nature. This classification is determined by calculating the Ginzburg Landau parameter $\kappa = \lambda/\xi$. This parameter is not only useful in classifying a superconductor as Type I or Type II, but it also reveals the locality of the material. The κ value of $1/\sqrt{2}$ is the boundary between the two regimes, with $\kappa_I < 1/\sqrt{2} < \kappa_{II}$. Specifically for the κ-$(ET)_2$-Br samples measured in this project, $\kappa > 100$, revealing the fact that these organics are

local as well as extreme Type II superconductors. For clarification, locality denotes the size of the sphere of influence (of radius ξ) for a given location inside the superconductor. Due to the fact that these organics are extremely localized superconductors, the current density is proportional to the vector potential in these materials, making the London equations and Ginzburg-Landau theory valid for this system.

It should be mentioned that work done by Leggett and Kosztin showed that non-local effects can exist for nodal superconductors at low temperatures[53]. They found that for temperatures $T < T_c\xi/\lambda$, the penetration depth can exhibit a quadratic temperature dependence. Since these materials have very high κ values, these effects could only be observed for temperatures below 70mK, which are well below the temperature range explored in this project.

3.2.3 Penetration Depth Behavior: Low T

In order to derive the temperature dependence of λ at low temperatures, the best place to start is with the superfluid density. According to the BCS model, the superfluid density (ρ) takes the form

$$\rho \equiv \frac{\lambda^2(0)}{\lambda^2(T)} = 1 - 2\int_{\Delta}^{\infty}\left(-\frac{\partial f}{\partial E}\right)\frac{E}{\sqrt{E^2-\Delta^2}}dE \tag{3.11}$$

where f is the Fermi function and Δ represents the superconducting gap. In the limit of $\beta^{-1} = k_BT \ll \Delta$, the superfluid density takes the form

$$\rho = \int_{\Delta}^{\infty}\beta e^{-\beta E}\frac{E}{\sqrt{E^2-\Delta^2}}dE \tag{3.12}$$

For an s-wave superconductor, the gap is assumed to be a constant value for all locations in k-space. In evaluating the integral in light of this fact, the $E/\sqrt{E^2-\Delta^2}$ piece sharply peaks at $E = \Delta$, resulting in an exponential temperature dependence of ρ

$$\rho = 1 - \sqrt{\frac{2\pi\Delta(0)}{k_BT}}e^{-\Delta(0)/k_BT} \tag{3.13}$$

The temperature dependence of the penetration depth can be seen by manipulating the expression for ρ

$$\rho = \frac{\lambda(0)^2}{\lambda(T)^2} = \left(1 + \frac{\Delta\lambda(T)}{\lambda(0)}\right)^{-2} \approx 1 - 2\frac{\Delta\lambda(T)}{\lambda(0)} \tag{3.14}$$

Comparison of the two previous equations reveals

$$\Delta\lambda(T) = 1 + \sqrt{\frac{\pi\Delta(0)}{2k_BT}}e^{-\Delta(0)/kT} \tag{3.15}$$

Since the tunnel diode oscillator is limited to making precise measurements of $\Delta\lambda$, this expression is useful in that it shows that measuring the temperature dependence of the *change* in λ can shed light on the gap structure. For s-wave specifically, this exponential form intuitively makes sense. For temperatures $T << T_c$, the penetration depth will not increase much with temperature. As the system temperature approaches T_c, the quasiparticle density will increase rapidly.

For the case of a superconductor with nodes in the gap, the low temperature behavior will be much different. Due to the fact that certain k-space directions have a zero gap, the quasiparticle number can increase for temperatures well below the critical temperature of the material. Analysis of various gap shapes with nodes revealed a power law temperature dependence[54] for the penetration depth, $\Delta\lambda \propto T^n$. The exponent of the temperature dependence not only depends on the shape of the nodes (lines or points in k-space) but also on the slope of the gap in the vicinity of the nodes. For the specific case of $d_{x^2-y^2}$ symmetry, a superconducting gap of $\Delta(\vec{k}_f) = \Delta(0)\left(\hat{k}_x^2 - \hat{k}_y^2\right)$ was used, where the gaps are located on the Fermi surface where $|k_x| = |k_y|$. This resulted in[55]

$$\Delta\lambda(T) = AT \tag{3.16}$$

$$A = \lambda(0)\frac{2ln(2)}{d\left|\Delta(\theta)\right|/d\theta|_{node}} \tag{3.17}$$

where the derivative in the denominator represents the slope of the gap near the node. In practice, d-wave superconductors display a power law temperature dependence ranging from $n = 1 - 2$ depending on the level of impurities in the sample[56]. This adds new significance to measuring $\Delta\lambda(T)$. A non-exponential temperature dependence of the penetration depth indicates the presence of nodes in the gap function and the exponent of the power law gives insight into the nature of the nodes (line or point).

3.3 Aluminum Plating

The major shortcoming of the tunnel diode oscillator technique is its inability to measure absolute values of the penetration depth[57]. The expression from Eqn. 2.21 will be restated and used for this explanation

$$f_s(T) - f_{ec} = \frac{1}{1-N}\frac{f_{ec}V_s}{2V_c}\left(1 - \frac{\lambda(T)}{R_{eff}}\tanh\frac{R_{eff}}{\lambda(T)}\right) \tag{3.18}$$

Given the high anisotropy of penetration depth in these organic samples, rectangularly shaped slabs were placed in a perpendicular field. Due to the inherent difficulty in modeling this orientation, a relatively large

error is associated with approximating the demagnetization factor (N) and the effective dimension (R_{eff}). Following the description given by Prozorov[57], the error in the measured frequency shift associated with placing the sample ($T = 0K$) in the coil is a few percent of the total shift. Since most samples have a total shift of about 10kHz, the corresponding error is a few hundred Hz. In examining a perfectly diamagnetic sample ($\lambda = 0$) versus one with a finite penetration depth, the total frequency shift associated with the penetration is on the order of 20-40 Hz. Therefore, the absolute frequency cannot possibly give an accurate measure of λ. In the case of *changes* in penetration depth, the 5-10% error is multiplicative instead of additive, resulting in precise measurements of changes in λ.

The best available option for measuring absolute penetration depths is an aluminum plating technique[57]. Since the measured frequency shifts can only be related to changes in λ, the aluminum serves as a reference with $\lambda_o^{Al} \approx 50$ nm[58,59]. This reference makes it possible to calculate and report absolute penetration depth values versus temperature. Although experimental techniques such as μSR claim to measure $\lambda(0)$, some of the assumptions that go into the analysis are questionable. For example, the μSR analysis of $\lambda(0)$ data assumes a fixed vortex lattice, which contradicts previous measurements of vortex pinning in these materials[60].

Aluminum was used to coat the samples for a couple of reasons. First, it is a common, inexpensive material that has been studied extensively. With its transition temperature and $\lambda(T)$ thoroughly characterized, there are no surprises to be expected from using this substance. More importantly, the transition temperature of aluminum is a low value of 1.2 K. Since the organics have T_c values close to 11-12 K, it is still possible to obtain low temperature ($T << T_c$) information about the system before the aluminum begins to expel the AC field.

Some care must be put into determining the proper thickness range for the aluminum films. First, the thickness must be comparable or larger than the penetration depth of aluminum ($t \geq \lambda_{Al}(0)$). This is important because it is essential that the field decays significantly in the aluminum. Otherwise, the purpose of the aluminum serving as a reference would be compromised. Second, the thickness must be smaller than the normal skin depth of the aluminum ($t < \delta_{Al}$) in order to assure that it is effectively invisible to the magnetic field above T_c^{Al}. This condition will guarantee that the signal above 1.2 K is purely due to the organic.

In order to describe the effect of coating any superconductor with aluminum, the model pictured in Fig. 3.5 was used. Notice that the penetration depth behavior differs for temperatures above and below the aluminum critical temperature. Given the present research, the samples under consideration will be denoted by the general label of high temperature superconductor (HTSC). For simplicity, the model will consist of an infinite slab in a parallel field. Using the general solutions to Eqn. 3.5, the field can be described by the

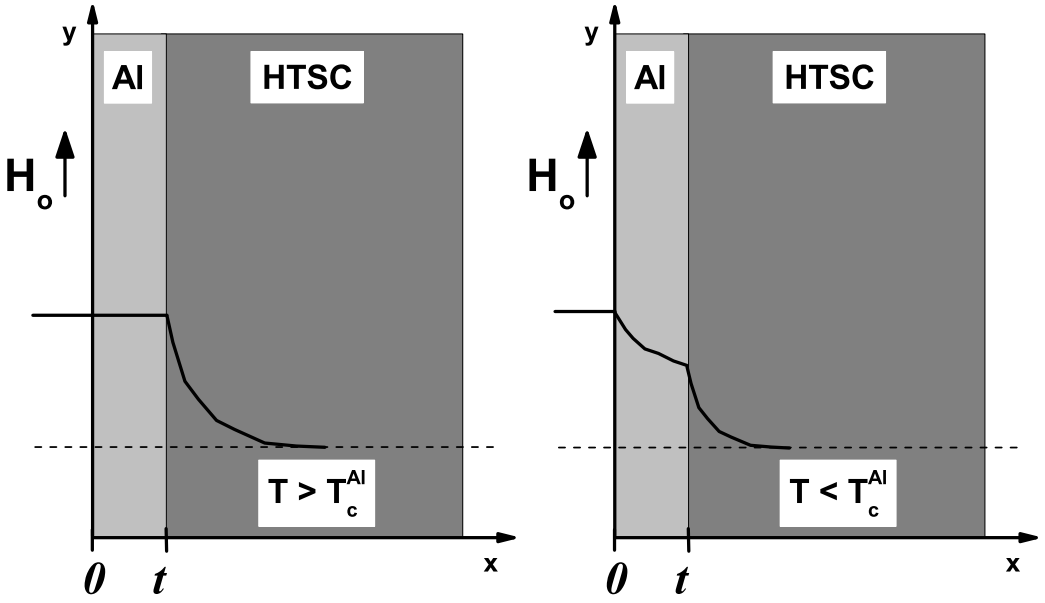


Figure 3.5: A thin aluminum film of thickness t on a superconducting slab in a parallel field $\mathbf{H}_0$. The left and right side represent the penetration for temperatures above and below the critical temperature of aluminum, respectively.

following expressions

$$H_{Al}(x) = Ae^{-x/\lambda^{Al}} + Be^{x/\lambda^{Al}} \tag{3.19}$$
$$H_{HTSC}(x) = Ce^{-x/\lambda^{HTSC}}$$

A relationship between λ^{Al} and λ^{HTSC} can be found using appropriate boundary conditions. Since this is not a transport measurement, $\mathbf{H}$ should be continuous across the boundaries giving the following conditions

$$\mathbf{H}_{Al}(0) = \mathbf{H}_{outside} = H_o\hat{y} \tag{3.20}$$
$$\mathbf{H}_{Al}(x=t) = \mathbf{H}_{HTSC}(x=t)$$
$$E^{\|}_{Al}(x=t) = E^{\|}_{HTSC}(x=t)$$

In order to use the third condition, the electric field ($\mathbf{E}$) must be calculated from the magnetic field. Using Eqn. 3.2 and the Maxwell equation that relates $\mathbf{H}$ to the current density ($\mathbf{J}$), an expression for $\mathbf{E}$ can be calculated

$$\frac{d\mathbf{J_s}}{dt} = i\omega\mathbf{J_s} = \left(\frac{1}{\mu_o\lambda^2}\right)\mathbf{E} \tag{3.21}$$

$$\nabla \times \mathbf{H} = \mathbf{J_s} = \left(\frac{1}{i\mu_o\omega\lambda^2}\right)\mathbf{E} \tag{3.22}$$

Using symmetry arguments and the fact that the field must point in the $\hat{y}$ direction to satisfy the first two boundary conditions, the relation becomes

$$\left(\frac{\partial H_y}{\partial x}\right)_{x=t}\hat{\mathbf{z}} = \frac{1}{i\mu_o\omega\lambda^2}\mathbf{E} \tag{3.23}$$

For completeness, the three boundary conditions in terms of $\mathbf{H}$ are

$$\begin{aligned} \mathbf{H}_{Al}(0) &= H_o\hat{y} \\ \mathbf{H}_{Al}(x=t) &= \mathbf{H}_{HTSC}(x=t) \\ \left(\frac{\partial H_{Al}}{\partial x}\right)_{x=t}\left(\lambda^{Al}\right)^2 &= \left(\frac{\partial H_{HTSC}}{\partial x}\right)_{x=t}\left(\lambda^{HTSC}\right)^2 \end{aligned} \tag{3.24}$$

After doing some algebra, the unknown field amplitudes (A, B, C) can be found in terms of known quantities $(\lambda^{Al}, \lambda^{HTSC}, t)$.

By definition, the effective penetration depth of the system (λ_{eff}) is

$$\lambda_{eff} \equiv \frac{1}{H_o}\int_0^\infty H(x)dx = \frac{1}{H_o}\int_0^t [Ae^{-x/\lambda^{Al}} + Be^{x/\lambda^{Al}}]dx + \frac{1}{H_o}\int_t^\infty Ce^{-x/\lambda^{HTSC}}dx \tag{3.25}$$

Plugging in the field amplitude values, the effective penetration depth takes the form

$$\lambda_{eff} = \begin{cases} \lambda^{Al}\frac{\lambda^{HTSC}+\lambda^{Al}tanh(t/\lambda^{Al})}{\lambda^{Al}+\lambda^{HTSC}tanh(t/\lambda^{Al})} & T < T_c(Al) \\ t + \lambda^{HTSC} & T > T_c(Al) \end{cases} \tag{3.26}$$

The analysis before Eqn. 3.26 dealt with the case of a superconducting film of aluminum on a slab of high temperature superconductor. For temperatures above the critical temperature of aluminum, the total penetration depth is simply the addition of the film thickness and the penetration depth into the HTSC.

Since the oscillator only measures an effective penetration depth change $(\Delta\lambda_{eff})$, we can calculate λ^{HTSC} in the following way:

$$\Delta\lambda_{eff} = \lambda_{eff}(T > T_c^{Al}) - \lambda_{eff}(0)$$

$$\lambda^{HTSC}(0) \approx \lambda^{HTSC}(T_c^{Al}) = \frac{1}{2}\left\{F + \sqrt{F^2 + 4\left(\lambda_o^{Al}\right)^2 + \frac{4\lambda_o^{Al}F}{tanh(t/\lambda_o^{Al})}}\right\} \tag{3.27}$$

$$F \equiv \Delta\lambda_{eff}(T_c^{Al}) - t$$

As mentioned before, the tunnel diode oscillator is only capable of measuring changes in λ for bare samples. The above analysis provides an expression that easily converts the traditionally calculated change in penetration depth (denoted as $\Delta\lambda_{eff}$) into an absolute value of $\lambda^{HTSC}(0)$.

It should be noted that the analysis up to this point is only useful in calculating the penetration depth of the HTSC at $T = T_c^{Al} = 1.2K$. As the above equation indicates, this value is approximated as $\lambda^{HTSC}(0)$. There are two ways in which one can calculate $\lambda^{HTSC}(T)$ for higher temperatures. Using the traditional analysis, the changes in penetration depth ($\Delta\lambda(T)$) can be calculated for temperatures above T_c^{Al}, ignoring the data below 1.2 K where the aluminum begins to exclude the field. Given the reference value of $\lambda^{HTSC}(0)$ obtained using this analysis, the temperature dependence of $\lambda^{HTSC}(T)$ can be found. The other method is to go back to the analysis above and solve it for higher temperatures. If $\Delta\lambda_{eff}(T)$ is calculated from Eqn. 3.26 for temperatures above T_c^{Al}, plugging in $\lambda^{HTSC}(1.2K) \approx \lambda^{HTSC}(0)$ from Eqn. 3.27 results in

$$\lambda^{HTSC}(T) = \Delta\lambda_{eff}(T) - t + \lambda_o^{Al}\frac{\lambda_o^{Al}\sinh t/\lambda_o^{Al} + \lambda_o^{HTSC}\cosh t/\lambda_o^{Al}}{\lambda_o^{Al}\cosh t/\lambda_o^{Al} + \lambda_o^{HTSC}\sinh t/\lambda_o^{Al}} \tag{3.28}$$

Since our samples have penetration depths on the order of $\sim 10\mu m$, both methods give identical results. Although this technique can be applied to any two local superconductors, this analysis is ideal for materials with large penetration depths. When dealing with $\lambda^{HTSC} \sim 10\mu$m, error associated with the aluminum thickness and penetration depth (both 50 ± 10 nm) are negligible.

Chapter 4

In-Plane Penetration Depth of Deuterated κ-$(ET)_2Cu[N(CN)_2]Br$

Although undeuterated (h8) κ-(BEDT-TTF)$_2$Cu[N(CN)$_2$]Br is interesting in its own respect, the focus of this research was on fully deuterated (d8) samples of κ-(BEDT-TTF)$_2$Cu[N(CN)$_2$]Br (κ-Br). The deuterated hydrogen locations are highlighted in Fig. 4.1. With the temperature vs pressure phase diagram for κ-(BEDT-TTF)$_2$Cu[N(CN)$_2$]Cl in mind (as shown in Fig. 1.3) full deuteration of the terminating ethyl groups for each BEDT-TTF molecule appears to have the effect of producing an internal pressure that moves the system somewhere in between the ambient pressure antiferromagnetic insulating (AFI) behavior of κ-(BEDT-TTF)$_2$Cu[N(CN)$_2$]Cl and the purely superconducting (SC) phase of the undeuterated κ-(BEDT-TTF)$_2$Cu[N(CN)$_2$]Br. The strongest evidence for the coexistence of AFI and SC phases in d8-κ-Br comes from ^{13}C NMR measurements with a field parallel to the conducting planes (a axis). Data obtained by Miyagawa and coworkers is given in Fig. 4.2. Although not shown, the h8-κ-Br system shows line broadening that levels off around 50 K. However, the d8-κ-Br system line broadening rapidly increases below 50 K with a two-peak structure remaining. This is an indicator that another phase exists below the superconducting critical temperature.

In addition to deuteration, the cooling rate of d8-κ-Br in the vicinity of 80K appears to effect the proportions of SC and AFI phases[61,62,63,64]. Some ^{13}C NMR measurements of the spin-lattice relaxation time for fast and slow cooled d8-κ-Br samples are shown in Fig. 4.3. For reference, the data for h8-κ-Br and κ-(BEDT-TTF)$_2$Cu[N(CN)$_2$]Cl were also shown. Notice that rapidly cooled d8-κ-Br samples appear to mimic the AFI behavior of κ-(BEDT-TTF)$_2$Cu[N(CN)$_2$]Cl whereas slow cooled d8-κ-Br samples behave more like the SC h8-κ-Br system. Although there is some opposition[11], the origin of this effect is believed to originate with the conformational freezing of the terminal ethylene groups[65] pictured in Fig. 4.1. Looking down the axis of the BEDT-TTF molecule, the pair of ethylene groups can either be in the eclipsed or staggered configuration. It is proposed that these ethylene groups are free to alternate between the two configurations for $T >> 80K$. Depending on the rate at which the temperature drops near 80K, the system can be forced to freeze into a frustrated state consisting of increased proportions of ethylene groups in the staggered configuration.

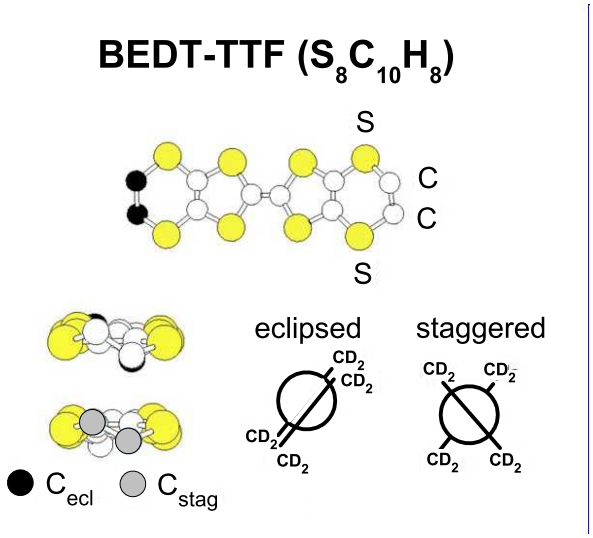


Figure 4.1: The BEDT-TTF molecule with the deuteration locations. Staggered and eclipsed configurations of the terminal ethylene groups are depicted. Reprinted with permission.[11].

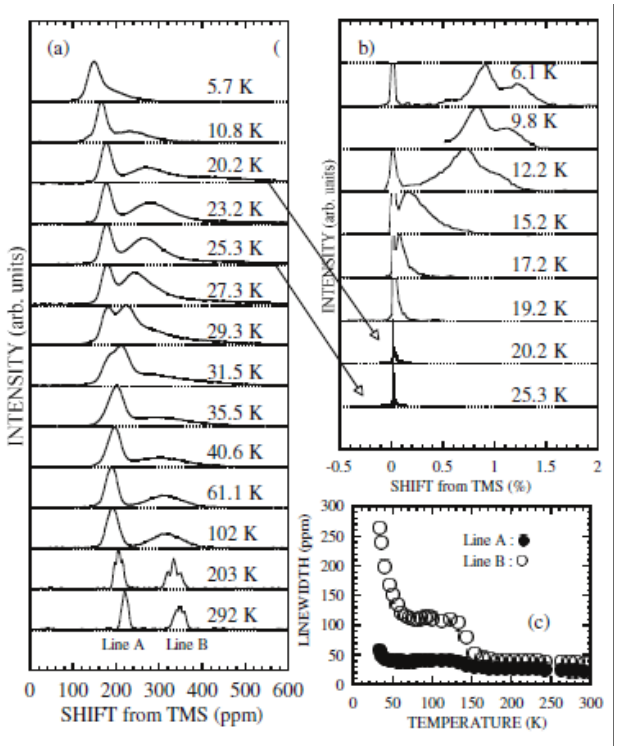


Figure 4.2: The NMR spectra for a single crystal of d8-κ-Br. a) Shift range is in ppm and b) of percent as the peaks separate further below 30K. c) Shows the temperature dependence of the linewidth. Reprinted with permission.[23].

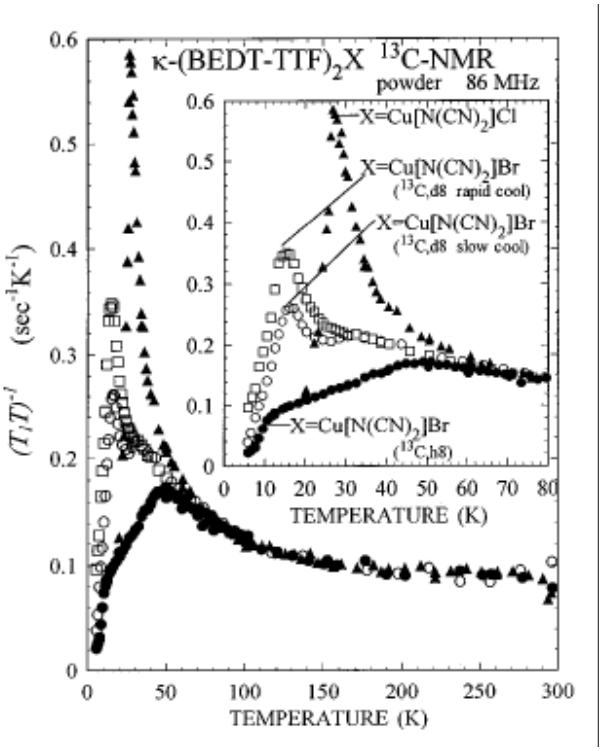


Figure 4.3: Spin-lattice relaxation rate for d8-κ-Br for fast and slow cooling rates. The rates for h8-κ-Br and κ-(BEDT-TTF)$_2$Cu[N(CN)$_2$]Cl were also measured for comparison. Reprinted with permission.[66].

4.1 Temperature Dependence of $\Delta\lambda_{d8}$

For the case of the cuprates, a thin sample placed in a parallel magnetic field would be sufficient to extract the in-plane penetration depth. However, prior investigations of κ-Br suggest $\lambda_\perp/\lambda_{||} > 100$, ruling out this possibility[60,29,30]. Therefore, the in-plane penetration depth was studied by placing rectangular samples in a perpendicular field. For this configuration, the penetration depth of the fully deuterated sample (λ_{d8}) is related to the change in oscillator frequency, $f_s(T)$, upon *in situ* insertion of the sample into the empty coil. The relationship is restated from Eqn. 2.19 as

$$f_s(T) - f_{ec} = \frac{gV_s}{1-N}\left(1 - \frac{\lambda_{d8}(T)}{R_{eff}}\tanh\frac{R_{eff}}{\lambda_{d8}(T)}\right) \tag{4.1}$$

It should be noted that all penetration depth quantities in this chapter result from in-plane supercurrents and therefore the || subscript will be omitted. The obvious problem with a finite slab in a perpendicular field is that the London equations cannot be solved analytically. Some work that was done previously in our lab was used to deal with this geometry and field orientation. In solving the London equations in two dimensions, the result was expanded to three dimensions, giving the expression[31]

$$R_{eff} = \frac{w}{4\left(1 + [1 + (d/w)^2]\arctan(w/d) - (d/w)\right)} \tag{4.2}$$

where d is the thickness of the sample and w is the effective width defined as $w = \sqrt{A_{surface}}$. As shown and derived in section 2.6, changes in penetration depth are proportional to changes in frequency

$$\Delta\lambda_{d8} = \lambda_{d8}(T) - \lambda_{d8}(0) = -\frac{R_{eff}}{\Delta f_p}\Delta f_s(T) \tag{4.3}$$

for the typical situation where $R_{eff} >> \lambda_{d8}$. Even though the penetration depth of these samples is very large, this approximation is still good for cases where $R_{eff} \geq 2\lambda_{d8}$.

The temperature dependence of the change in penetration depth is shown in Fig. 4.4. The cooling rate was varied from 6 K/min to 30 mK/min. The data are plotted versus $T^{3/2}$ since, for all rates, the exponent is within the range $n = 1.5$–1.7. This exponent is close to the value $n = 1.5$ which was first reported in slowly-cooled, single crystals of undeuterated κ-$(ET)_2Cu[N(CN)_2]Br$ and κ-$(ET)_2Cu(NCS)_2$ [13]. Although the deuterated samples are most likely composed of separated regions of AFI and SC, the power law temperature dependence is quite robust, indicating that the superconducting gap function still manifests nodal characteristics.

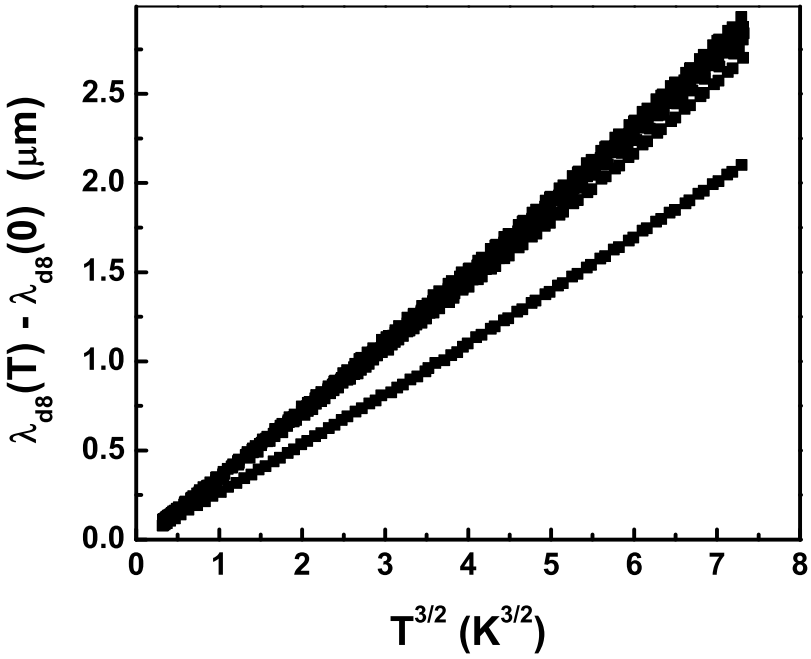


Figure 4.4: Temperature dependence of $\Delta\lambda_{d8}$ for an unplated sample. Separate curves for each sample correspond to different cooling rates.

4.2 Absolute Values of Penetration Depth

Although $\Delta\lambda_{d8}(T)$ reveals the fact that d8-κ-Br has a nodal gap, there is no way to determine the absolute value of the penetration depth using conventional tunnel diode methods. Therefore, the aluminum plating technique was used to measure this quantity directly. The change in frequency $\delta f(T_c^{Al})$ is proportional to the change in penetration depth of the plated sample $\Delta\lambda_{eff}(T_c^{Al})$. As can be observed from Fig. 4.5, $\delta f(T_c^{Al})$ is the frequency shift associated with the aluminum film transition. In the limit that $\Delta\lambda_{eff}(T_c^{Al}) \gg t, \lambda_o^{Al}$, the expression simplifies to $\lambda_{d8}(0) \approx \Delta\lambda_{eff}(T_c^{Al} - t + \lambda_o^{Al} \approx \Delta\lambda_{eff}(T_c^{Al})$. Given that the penetration depths of these samples are on the order of microns, all of the data was in this limit. In order to calculate $\Delta\lambda_{eff}$, the aluminum frequency shift $\delta f(T_c^{Al})$ is measured and used in the familiar expression

$$\Delta\lambda_{eff} = \frac{R_{eff}}{\Delta f_p}\delta f(T_c^{Al}) \tag{4.4}$$

where $R_{eff} >> \lambda_{eff}$ is assumed.

As a test, this technique was attempted on a sample of known penetration depth. Applying this method to a slowly cooled sample of undeuterated h8-κ-Br yielded $\lambda_{h8}(0) = 1.2\mu$m, which is comparable to, though somewhat larger than the value of 0.8 μm obtained from μSR measurements[67]. The results are shown in Fig. 4.6. In addition, the temperature dependence of the penetration depth was measured. This resulted in a 3/2 power law which agrees with earlier tunnel diode results[13]. This was an important result because it assured that the aluminum was magnetically invisible for $T > T_c^{Al}$.

With initial testing done, a d8-κ-Br sample was coated uniformly with Al to a thickness of $t = 500$ Å, a value small compared to the Al skin depth but comparable to its penetration depth ($\lambda_o^{Al} = 500$Å). Using the expression above, the raw data was converted to penetration depth values. However, initial analysis suggested penetration depths on the order of 30-80 μm, proving the assumption that $R_{eff} >> \lambda_{eff}$ is not true for the faster cooling rates. In the regime where the penetration depth is comparable to R_{eff}, a corrective factor is added to Eqn. 4.4 giving

$$\delta f(T_c^{Al}) = \Delta f_p \frac{\lambda_{eff}(T_c^{Al})}{R_{eff}} \tanh\left(\frac{R_{eff}}{\lambda_{eff}(T_c^{Al})}\right) \tag{4.5}$$

$$\Delta\lambda_{eff} = \lambda_{eff}(T_c^{Al}) - \lambda_{eff}(0) \approx \lambda_{eff}(T_c^{Al}) \tag{4.6}$$

where the effective penetration depth for $T << T_c^{Al}$ is very small compared to R_{eff}. This is certainly true since the majority of the field is screened by the aluminum coating at this temperature, which means

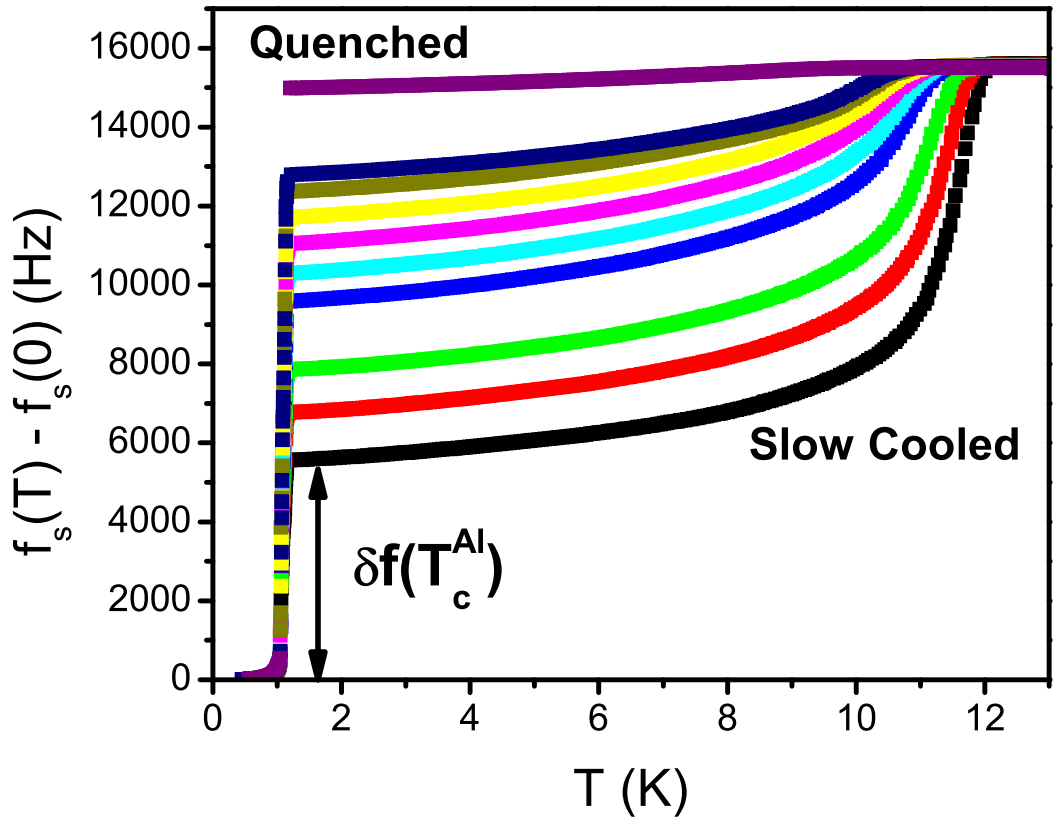


Figure 4.5: Temperature dependence of the frequency response of the aluminum plated d8-κ-Br sample for all of the cooling rates. The frequency shift associated with the aluminum transition ($\delta f(T_c^{Al})$)is labeled for the slowest cooling rate.

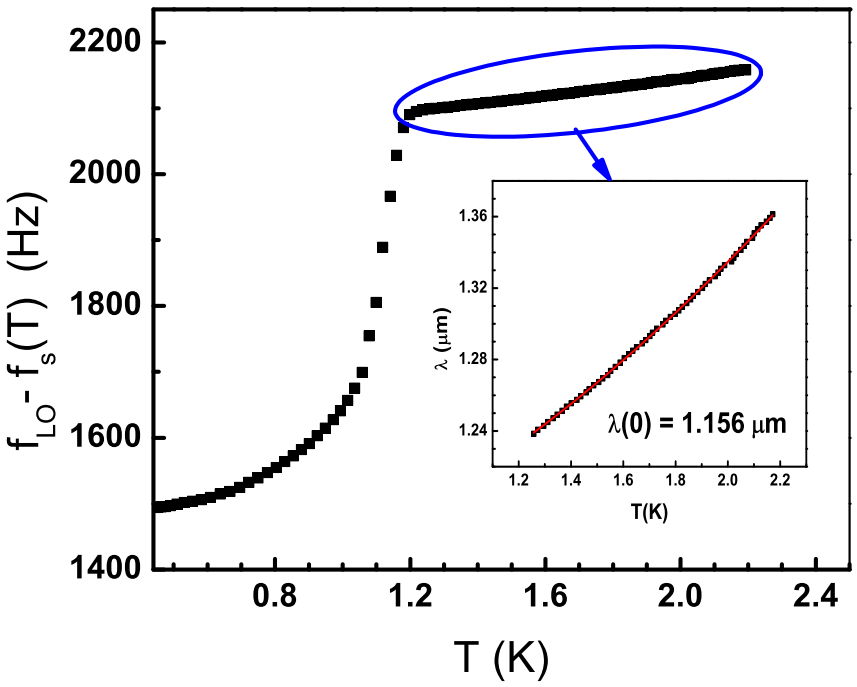


Figure 4.6: Frequency data for aluminum plated h8-κ-Br. The inset shows the resulting value of the absolute value of the zero temperature penetration depth.

$\lambda_{eff}(T << T_c^{Al}) \approx \lambda_o^{Al} = 50nm << R_{eff}$. Fig. 4.7 shows the absolute penetration depth λ_{d8} for the Al-plated sample. Cooling rates ranged from 180 K/min (20 sec cooling time) to 2.5 mK/min (3 week cooling time). The λ_{d8} values are extremely large, though in reasonable agreement with previous susceptibility measurements[68,14] and consistent with the picture of a composite material as discussed earlier. Again, all data fit a power law exponent in the range $n = 1.6$–1.8, with the exception of the quenched sample that had an exponent $n = 2$.

In addition to changes in the absolute penetration depth, a noticeable T_c reduction was observed with increased cooling rates. Frequency data taken near the superconducting transition is shown in Fig. 4.8. The critical temperature ranged from 10-12K for fast-slow cooling rates. With respect to reporting the critical temperature, some groups locate T_c at the midpoint of the transition while others determine the onset transition from the normal to superconducting state. The critical temperatures for this work were found by determining the temperature at which the data deviates by 1% from the normal state extrapolation.

The Al coating also provides a measure of the Meissner fraction, η_{sc}. At the lowest temperatures, the sample is a nearly perfect diamagnet since λ_o^{Al} is far smaller than any sample dimension. Just above T_c^{Al} the screening is determined by the organic superconductor alone. By comparing these two frequency shifts, we obtain η_{sc}

$$\eta_{sc} = \frac{\Delta f_p - \delta f(T_c^{Al})}{\Delta f_p} \tag{4.7}$$

where it should be repeated that the pullout frequency (Δf_p) refers to the frequency shift associated with pulling the sample out of the coil at the base temperature. Fig. 4.9 shows the Meissner fraction plotted verses the $\log_{10}$(Cool Time) over 5 decades of cooling time. The linear relationship is consistent with several previous studies showing that the formation of superconducting regions is governed by glassy dynamics near 80K[64].

Since the temperature dependence of λ_{d8} is non-integer and falls in the range n = 1-2, d8-κ-Br is suspected of being a dirty d-wave superconductor. Within the d-wave with impurity model, one has $\rho_{d8} = (\lambda_{d8}(0)/\lambda_{d8}(T))^2 = 1 - \alpha T^2/(T + T^\star)$. $T^\star$ is an impurity crossover temperature that increases with unitary limit scattering[56]. A plot of the temperature dependence of the superfluid density is shown in Fig. 4.10 for several cooling rates with one data set fit to the d-wave impurity model. We found that $2.6K < T^\star < 6.6K$ with no correlation between $T^\star$ and cooling rate. These values as well as other relevant quantities are shown in Table 4.1 for the aluminum plated sample. This is consistent with n being nearly constant and would imply that no significant disorder is introduced by rapid cooling, despite the large changes in Meissner fraction that occur. The near constancy of n in this experiment, together with previous observations in both

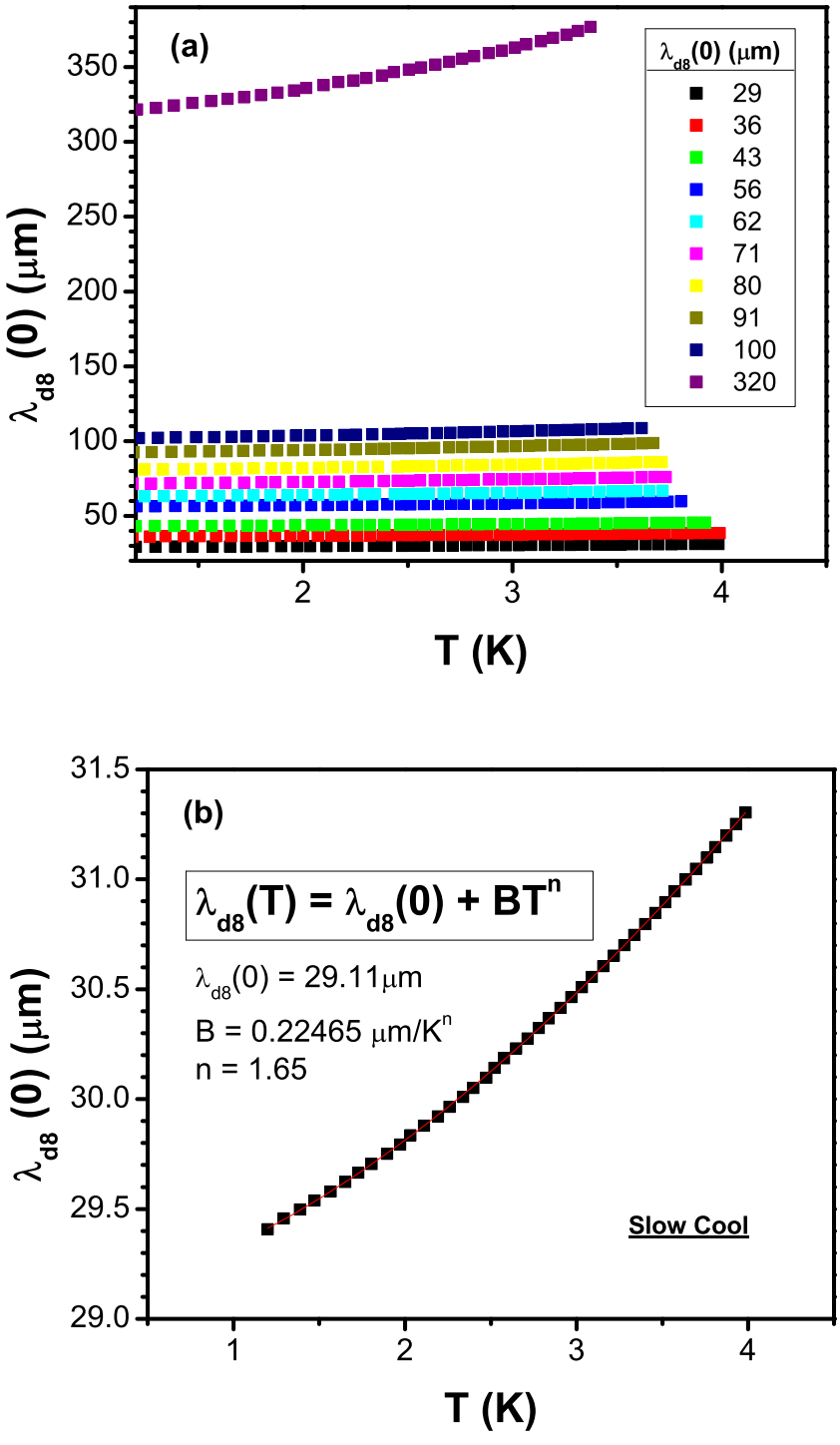


Figure 4.7: (a) Plot of λ_{d8} as a function of T for several cooling rates. Each curve has a distinct $\lambda_{d8}(0)$. (b) Slow cooled data fit to a power law temperature dependence.

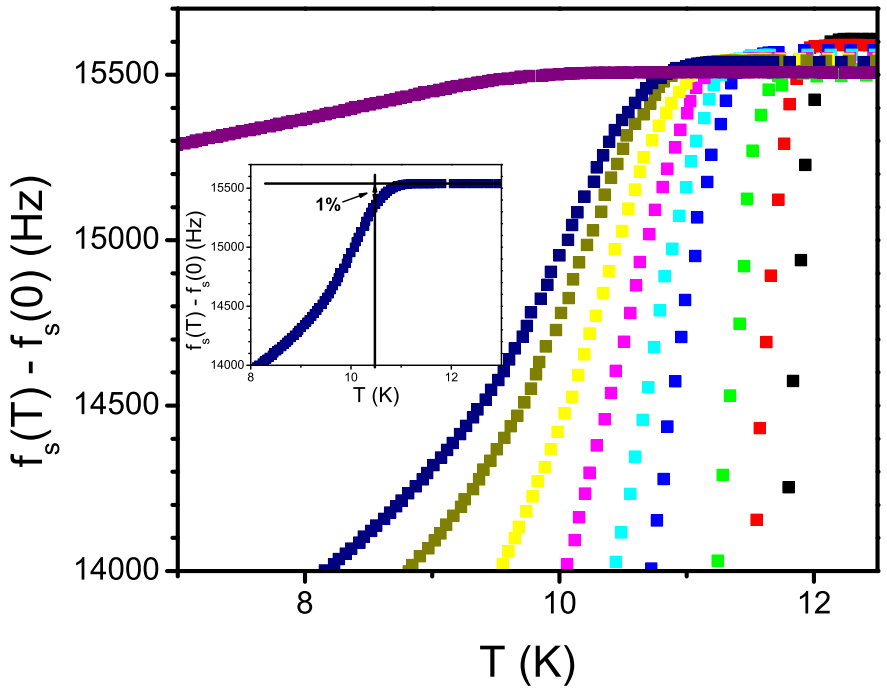


Figure 4.8: Frequency data for all cooling rates with the highest T_c curve corresponding to the slowest cooling rate. The inset shows the procedure for determining T_c.

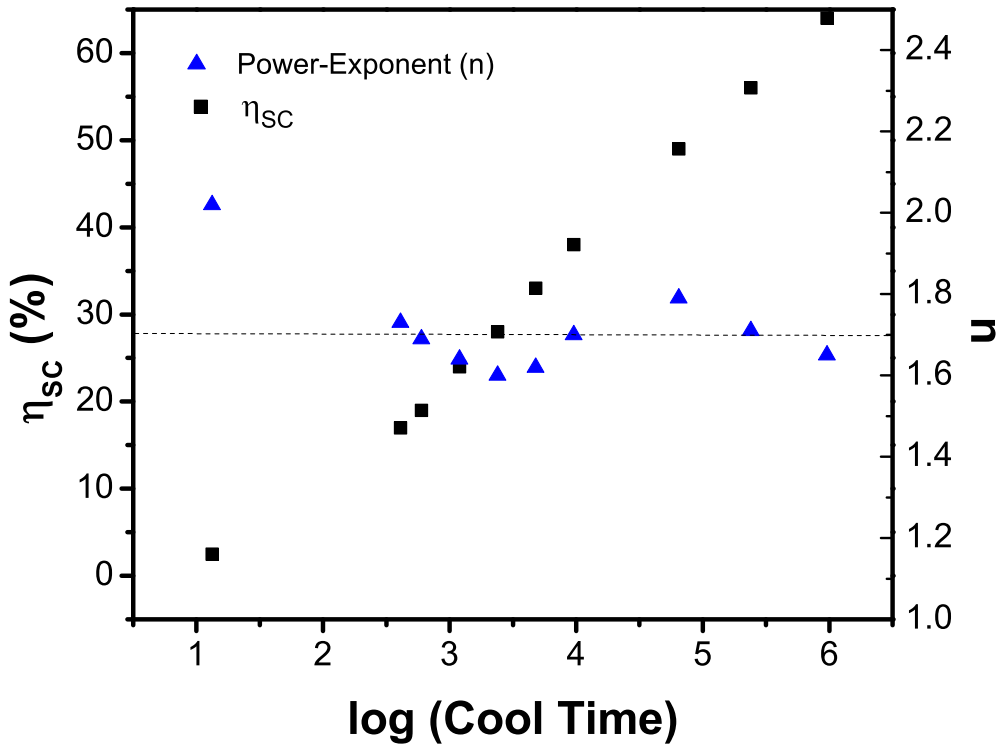


Figure 4.9: Plot of the linear dependence of η_{sc} on the log(CoolTime) from 100-60K as well as the power law exponent n.

κ-$(ET)_2Cu[N(CN)_2]Br$ and κ-$(ET)_2Cu(NCS)_2$ [13] suggests that the quasiparticle spectrum in these materials has general features that survive changes in anion chemistry, unit cell symmetry, transition temperature, phase separation, deuteration and proximity to antiferromagnetism.

4.3 Spherical Grain Analysis

Since these d8-κ-Br samples yielded penetration depths of 30-320 μm, the picture of a SC/AFI coexistence seemed quite possible. With this in mind, the data was reevaluated in the context of a collection of superconducting spheres. The d8-κ-Br sample was assumed to consist of N_{sph} independent spherical grains of identical radius R_{sph}, each with in-plane penetration depth, λ_{sph}, surrounded by an insulating matrix whose magnetic properties can be neglected. The change in oscillator frequency upon inserting the sample is then given by,

$$f_s(T) - f_{ec} = g \sum_{i=1}^{N_{sph}} V_i \chi_i(T) = g N_{sph} \frac{4\pi R_{sph}^3}{3} \chi_{sph}(T) \tag{4.8}$$

for $T > T_c(Al)$. Also, g is a constant that depends on the effective coil volume and empty coil frequency

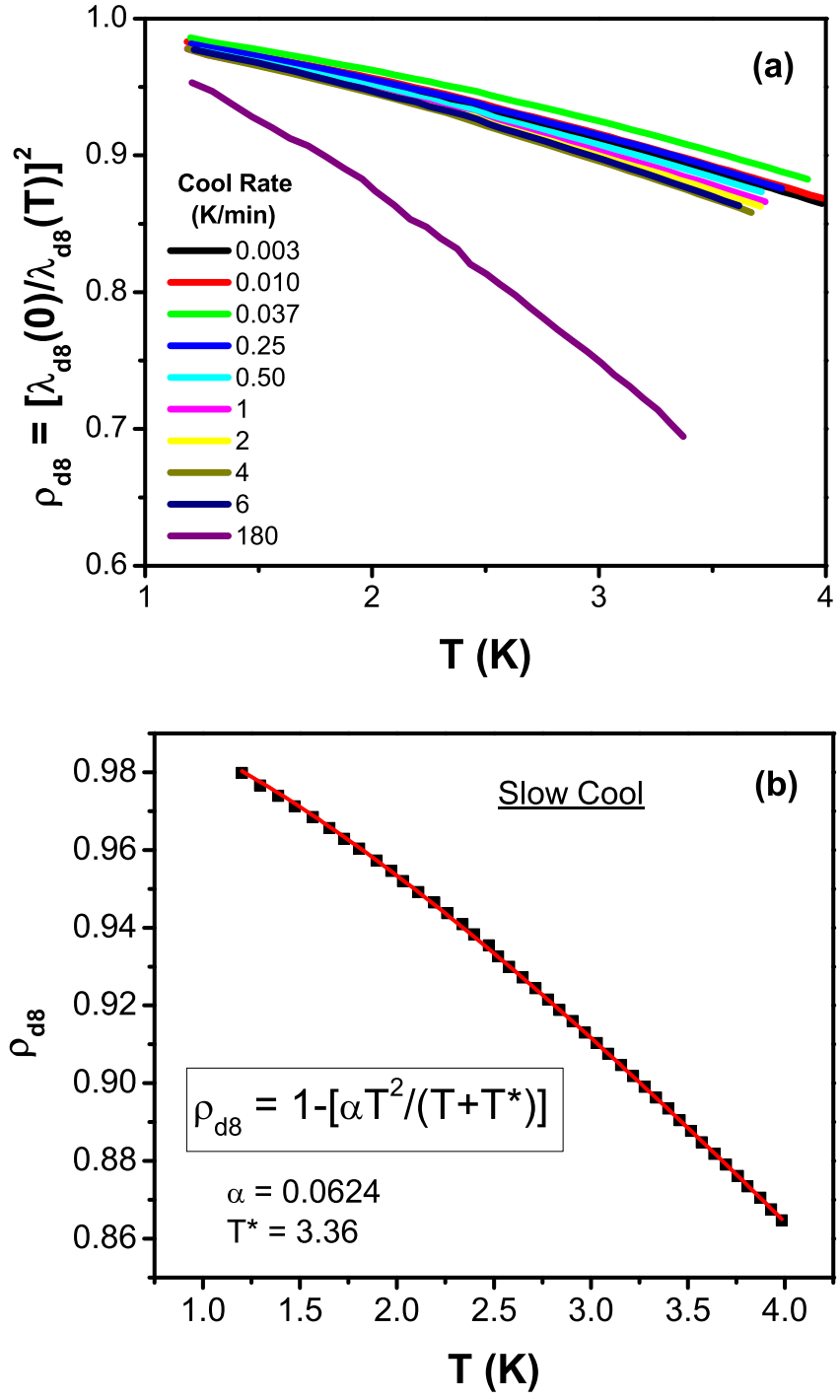


Figure 4.10: (a) The superfluid density versus temperature for a wide range of cooling rates. With the aluminum plating method, the actual value of $\lambda_{d8}(0)$ can be used instead of treating it as a fitting parameter. (b) The slow cool superfluid density is fit to the impurity model for d-wave superconductors.

Al-plated d8-κ-Br

Cool Rate (K/min)	α (1/K)	T* (K)	$\lambda_{d8}(0)$ (μm)	T_c (K)	n	η_{sc} (%)	τ (psec)
0.0025	0.0624	3.36	29	12.01	1.65	64	0.636
0.01	0.0677	4.22	36	11.87	1.71	56	0.643
0.037	0.0786	6.39	43	11.67	1.79	49	0.655
0.25	0.0667	4.03	56	11.39	1.7	38	0.671
0.5	0.0596	2.81	62	11.29	1.62	33	0.677
1	0.0603	2.57	71	11.2	1.6	28	0.682
2	0.0666	2.99	80	11.07	1.64	24	0.69
4	0.0753	3.52	91	10.96	1.69	19	0.697
5.8	0.0808	4.12	101	10.88	1.73	17	0.702
180	0.268	6.59	320	10	2.02	2.4	0.764

Table 4.1: Calculated quantities for the aluminum plated d8-κ-Br sample.

($g = f_{ec}/2V_c$). The standard expression for the susceptibility of a sphere is given by

$$\chi_{sph}(T) = 1 - 3\left(\frac{\lambda_{sph}(T)}{R_{sph}}\right)\coth\left(\frac{R_{sph}}{\lambda_{sph}(T)}\right) + 3\left(\frac{\lambda_{sph}(T)}{R_{sph}}\right)^2 \tag{4.9}$$

To eliminate N_{sph}, which is assumed to be fixed for a given cool rate yet not known, we took the ratio of $f_s(T) - f_s(0)$ to the total change in frequency obtained by removing the sample, $\Delta f_p = f_s(0) - f_{ec}$. Assuming that $R_{sph} \gg \lambda_{sph}(0)$, Eqn. 4.8 leads to,

$$\frac{f_s(T) - f_s(0)}{\Delta f_p} = -3\frac{\Delta\lambda_{sph}(T)}{R_{sph}} \tag{4.10}$$

In order to isolate the radius, the grains were assumed to have the same parameters as undeuterated h8-κ-Br ($B = 0.0425\mu m K^{-1.5}$, $\lambda_{sph}(0) = 0.78\mu m$), where $\lambda(T) - \lambda(0) = BT^{3/2}$. Fitting the data to Eq. 4.10 yields $R_{sph} \approx 6 - 40\mu m$ with slower cooling rates giving larger values of the radii. These values were obtained from an unplated d8-κ-Br sample with the values given in Table 4.2. The calculated grain sizes are in good agreement with local infrared measurements[69].

Since the B parameter actually contains a factor of $\lambda_{sph}(0)$, the natural question arose whether the change in R_{sph} was real or actually a change in B with cooling rate. If it was the latter, the assumption that the spheres were made up of h8-κ-Br would not be valid. In order to answer this question, the high

Unplated d8-κ-Br			
Cool Rate (K/min)	**T_c (K)**	**R_{sph} (μm)**	**n**
0.037	11.9	39.2	1.59
0.25	11.54	23.4	1.56
0.5	11.45	20.5	1.58
1	11.33	18.2	1.59
2	11.24	16.3	1.59
3	11.17	15.4	1.57
4	11.13	14.4	1.58
5.8	11.07	14.1	1.61
180	10.22	5.6	1.61

Table 4.2: Calculated and measured quantities for an unplated d8-κ-Br sample.

temperature data was analyzed. Using the same method as before, the number of grains can be divided out. However, the assumption that $\lambda_{sph} << R_{sph}$ does not hold near T_c leaving the expression

$$\frac{f_s(T) - f_{ec}}{f_s(0) - f_{ec}} = \frac{1 - 3\left(\frac{\lambda_{sph}(T)}{R_{sph}}\right)\coth R_{sph}/\lambda_{sph}(T) + 3\left(\frac{\lambda_{sph}(T)}{R_{sph}}\right)^2}{1 - 3\left(\frac{\lambda_{sph}(0)}{R_{sph}}\right)\coth R_{sph}/\lambda_{sph}(0) + 3\left(\frac{\lambda_{sph}(0)}{R_{sph}}\right)^2} \tag{4.11}$$

As it stands, this expression has three unknowns. Since this part of the analysis focuses on temperatures comparable to the critical temperature, the modified Gorter-Casimir relation was used, which relates the temperature dependence of $\lambda(T)$ to $\lambda(0)$

$$\lambda(T) = \frac{\lambda(0)}{\sqrt{1 - t_c^{4/3}}} \tag{4.12}$$

where $t_c = T/T_c$ is the reduced temperature and the power of t_c has been modified from the classic value of $n = 4 \rightarrow 4/3$ since the sample is believed to be d-wave[49]. A sample data fit using this modified exponent is given in Fig. 4.11. Plugging this into Eqn. 4.11, only one unknown remains $(\lambda(0)/R_{sph})$ since T_c is easily determined from the high temperature data. Using this method, we obtain values of $\lambda(0)/R_{sph} = 0.0540 - 0.1861$ with larger values pertaining to faster cooling rates.

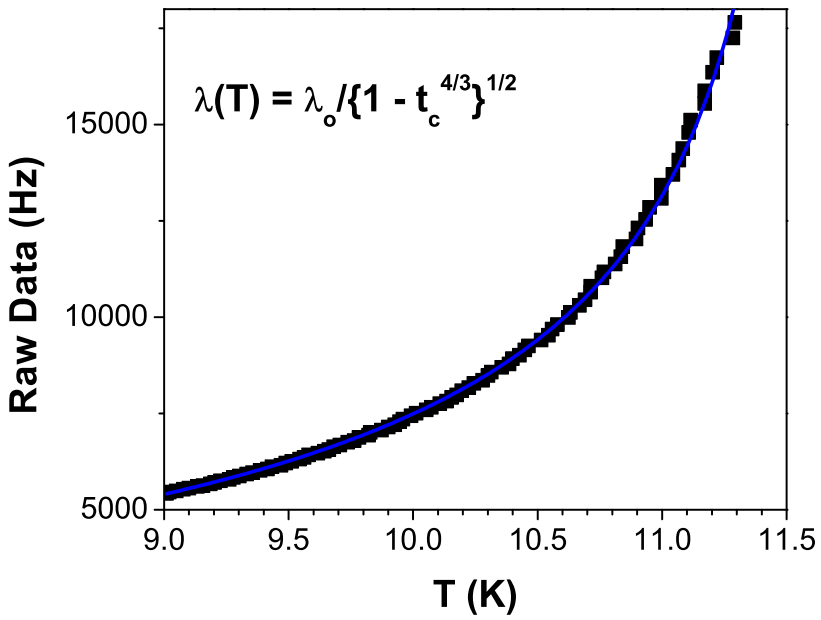


Figure 4.11: Data fit to the modified Gorter-Casimir relation with $n = 4/3$.

With the radii determined from low temperature data coupled with data near T_c, $\lambda(0)$ values could be calculated for each of the cooling rates. As it turns out, values of $\lambda(0) = 2.3 \pm 0.3\mu m$ were obtained without any observable monotonic behavior. Although these values are larger than the 0.78 μm assumed for low

data analysis, the values are not far removed from the value of 1.8 μm previous reported by our group for h8-κ-Br samples[13]. Also, the fact that R_{sph} was assumed to be constant for the entire temperature range from 0K up to T_c could be the source of the apparent difference in $\lambda(0)$.

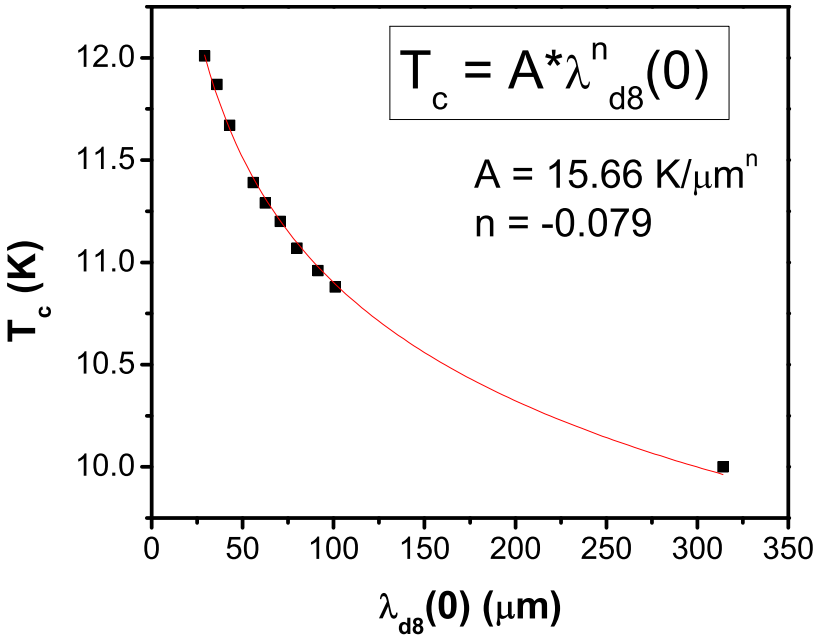


Figure 4.12: Plot of $\lambda_{d8}(0)$ versus T_c for all cooling rates.

Another relationship of interest is the dependence of $\lambda_{d8}(0)$ with T_c. For cooling rates ranging from 0.003 to 180 K/min, our experiments yield a precise power law reduction in T_c as a function of $\lambda_{d8}(0)$ as shown in Fig. 4.12. The exponent of the power law is $n = -0.079$. This is rather different from the $T_c \sim \lambda_0^{-2}$ relation first reported by Uemura in Copper oxide materials where the T_c reduction was thought to depend on the change in superconducting electron density[70].

Another way of modeling the pair breaking that leads to T_c reduction is found in the Abrikosov-Gorkov theory. For our specific case, the reduction in critical temperature would be modeled as

$$k_B \left(T_{c0} - T_c\right) = \frac{\hbar}{\tau} \tag{4.13}$$

where $1/\tau$ is the scattering rate. Since each cooling rate results in a different T_c and therefore a different $1/\tau$, the scattering rate is plotted verses the $\log_{10}$(Cool Time) in Fig. 4.13. Although magnetic impurities would be required for s-wave, the mechanism for a d-wave superconductor could be a variety of scattering mechanisms.

Another cause for the T_c reduction could be a metastable pressure developed during the cooling process.

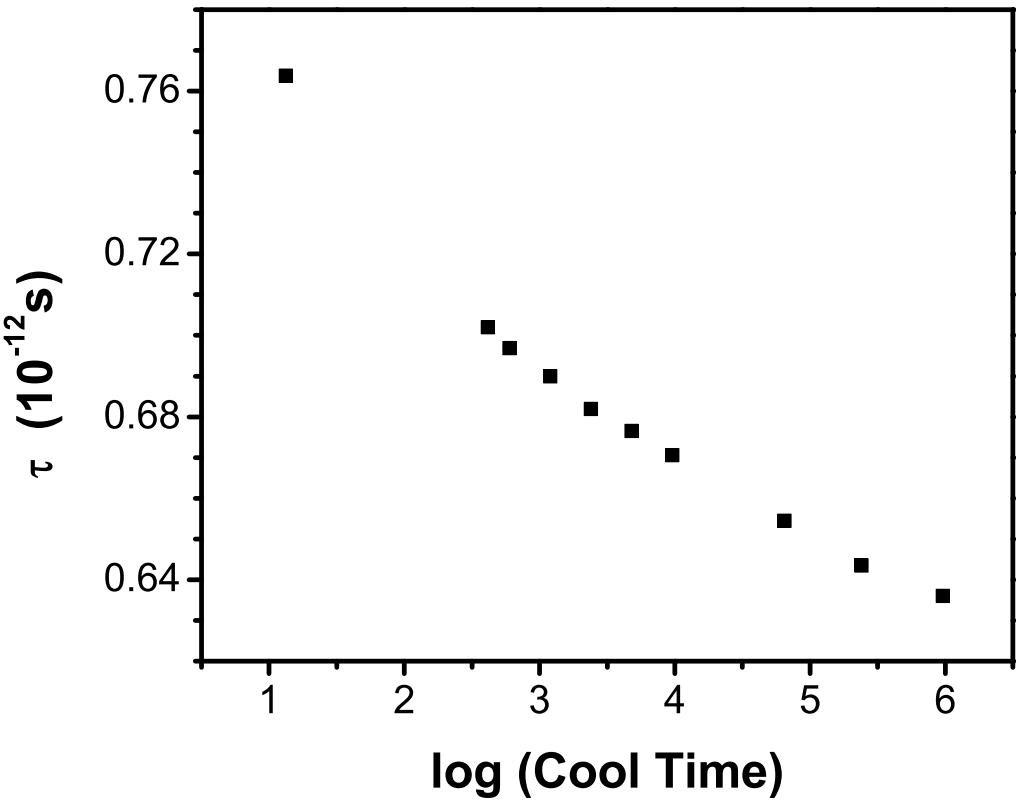


Figure 4.13: Abrikosov-Gorkov scattering time as a function of the log of the cooling time in the vicinity of 80K.

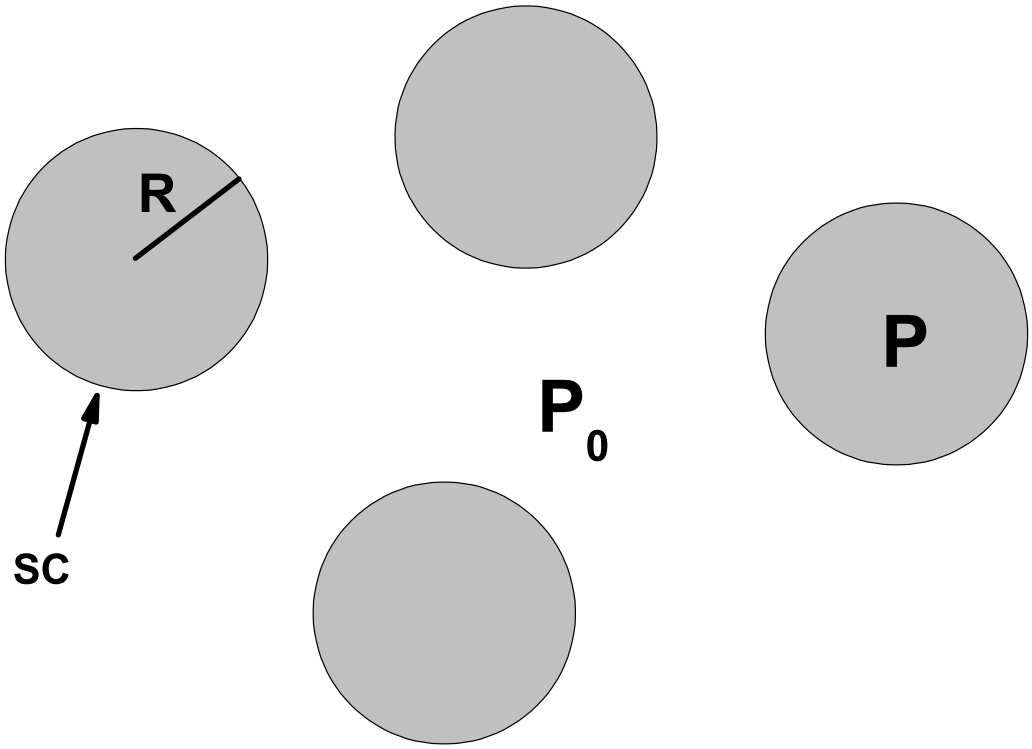


Figure 4.14: Picture of superconducting spheres that experience a pressure differential.

It is well-established that organic superconductors exhibit the largest coefficient of dT_c/dP of any class of materials[71]. This has been attributed to a decrease of electronic correlation energy with pressure. Given the logarithmically slow rates of nucleation, any finite cooling rate will lead to a metastable equilibrium and unrelaxed pressure. A picture of this scenario is given in Fig. 4.14. The AFI background is assumed to be at one pressure (P_0) while each superconducting grain is at a different pressure (P). This pressure difference can be represented as

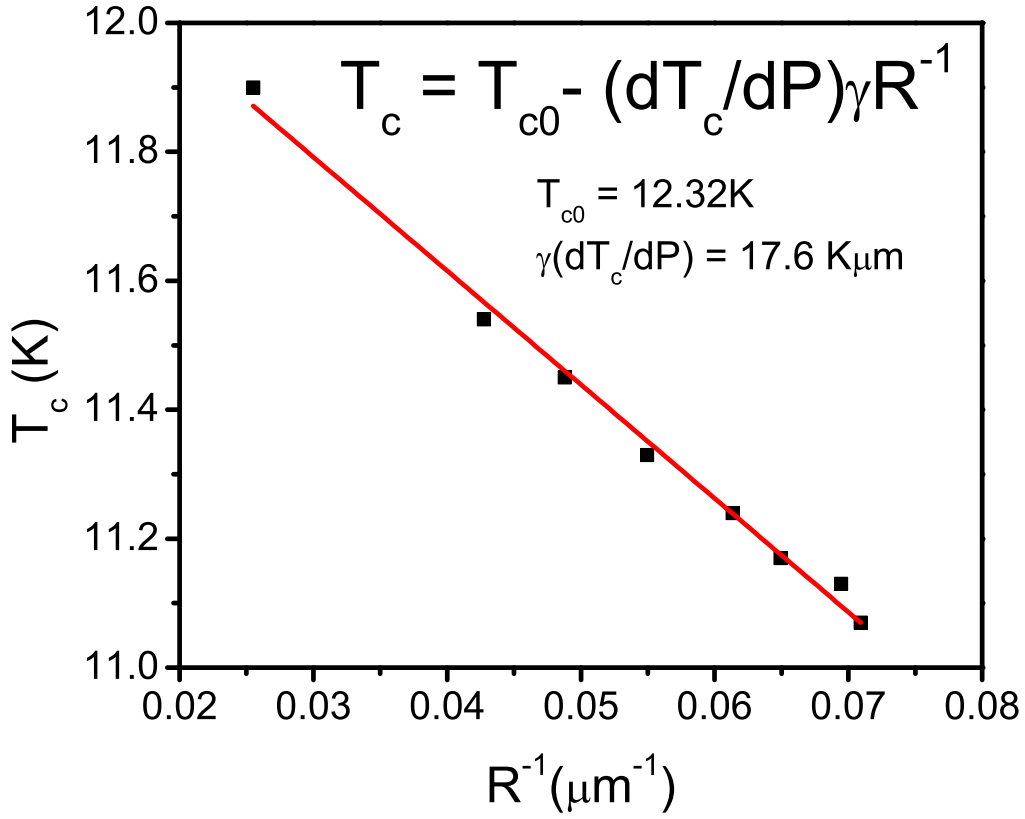


Figure 4.15: Inversely proportional relationship between T_c and grain radius for various cooling rates.

$$P - P_0 = \frac{\gamma}{R} \tag{4.14}$$

where γ is the surface tension of the grains/background interface and R is the radius of the SC grains. In examining the expression for the suppression of T_c with pressure

$$T_{c0} - T_c = \frac{dT_c}{dP}\Delta P \tag{4.15}$$

where T_{c0} and T_c represent the fully SC and partially SC (brought about by faster cooling rates) critical

temperatures, a relationship between T_c reduction and grain radius can be obtained

$$T_{c0} - T_c = \frac{dT_c}{dP}\frac{\gamma}{R} \tag{4.16}$$

A plot of $T_{c0} - T_c$ vs. R^{-1} is given in Fig. 4.15. Taking the slope of the fit and using the value of $dT_c/dP = 3K/kbar$ for κ-(BEDT-TTF)$_2$Cu(NCS)$_2$, a rough estimate of the surface tension was calculated, resulting in $\gamma = 600$ J/m^2. For comparison, the γ value for the Pt-air interface is 2 J/m^2. Given that a solid/gas interface is much different than the boundary between a SC and AFI, this high value may be reasonable. Given the good fit of this model, the reduction in critical temperature most likely results from pressure differentials introduced by cooling rates.

4.4 Conclusions

In conclusion, absolute penetration depth measurements confirm that deuterated κ-(ET)$_2$Cu[N(CN)$_2$]Br have penetration depths on the order of 30-300 μm. The linear relationship between the Meissner fraction and the log$_{10}$(Cool Time) suggests that the superconducting domains are formed via a glassy transition. Through the use of a simple, independent spheres model, the system may be comprised of a collection of h8-κ-Br grains in an antiferromagnetic background with a T_c reduction caused by pressure differences between the two phases. Also, the penetration depth temperature dependence exhibits a power law behavior with exponents ranging from 1.6-1.8 for non-quenched cooling rates, suggesting that the nodal gap nature remains relatively unchanged with large changes in Meissner fraction.

Chapter 5

Interplane Penetration Depth of κ-$(ET)_2Cu[N(CN)_2]Br$

Although several groups using a variety of techniques claim large values for the interplane penetration depth ($\lambda_\perp \sim 100\mu m$), the range of values vary by an order of magnitude. In this work, two undeuterated superconductors from the κ-$(ET)_2X$ family were studied, namely κ-$(ET)_2Cu[N(CN)_2]Br$ and κ-$(ET)_2Cu(NCS)_2$. In addition to confirming abnormally large penetration depths in these organics, the transport associated with these anamolous materials was investigated[30].

5.1 Experimental

Samples of κ-$(ET)_2Cu[N(CN)_2]Br$ ($T_c = 11.95K$) and κ-$(ET)_2Cu(NCS)_2$ ($T_c = 9.8K$) in the shape of thin, irregular platelets were grown using methods described earlier[72]. For each sample, the RF magnetic field was applied in two orthogonal directions (in separate runs) as shown in Fig. 5.1. Both field orientations were parallel to the conducting planes, in turn generating both in-plane and interlayer supercurrents. These currents penetrate the sample by $\lambda_{||}$ and $\lambda_\perp$, respectively. For a thin rectangular slab of thickness d and length L, in which demagnetizing effects are negligible, the effective susceptibility is given by[27],

$$-\chi = 1 - \frac{2\lambda_{||}}{d}\tanh\frac{d}{\lambda_{||}} - \frac{16\lambda_\perp}{\pi^2 L}\sum_{n=0}^{\infty}\frac{\tanh\left(q_n L/2\right)}{\left(2n+1\right)^2\left(k_n^2\lambda_{||}^2+1\right)^{3/2}} \tag{5.1}$$

where $k_n = (2n+1)\pi/d$ and $q_n^2 = (k_n^2\lambda_{||}^2 + 1)/\lambda_\perp^2$. According to this formula the susceptibility will be dominated by $\lambda_\perp$ if the anisotropy $\gamma = \lambda_\perp/\lambda_{||} >> L/d$. In our case $\gamma \approx 100 >> L/d < 10$ so this condition is well satisfied. In this limit of extreme anisotropy, the susceptibility reduces to the standard result,

$$-\chi = 1 - \frac{2\lambda_\perp}{L}\tanh\frac{L}{2\lambda_\perp} \tag{5.2}$$

In fact, our samples were thin, irregular polygons as shown schematically in Fig. 5.1. We approximated the total RF susceptibility by assuming the slab susceptibility Eqn. 5.2 for each section of width L(x) and then integrating the result to obtain,

Material	$\lambda_\perp(0)$ (μm)	Technique	Reference
κ-$(ET)_2Cu[N(CN)_2]Br$	130 ± 20	Tunnel diode oscillator	This work
κ-$(ET)_2Cu[N(CN)_2]Br$	100 ± 20	Tunnel diode oscillator	Ref.[13]
κ-$(ET)_2Cu[N(CN)_2]Br$	90	Josephson plasma resonance	Ref.[73]
κ-$(ET)_2Cu[N(CN)_2]Br$	233	AC susceptibility	Ref.[15]
κ-$(ET)_2Cu(NCS)_2$	130 ± 20	Tunnel diode oscillator	This work
κ-$(ET)_2Cu(NCS)_2$	60	Scanning SQUID probe	Ref.[74]
κ-$(ET)_2Cu(NCS)_2$	200	AC susceptibility	Ref.[27]
κ-$(ET)_2Cu(NCS)_2$	30	Surface Impedance (100 GHz)	Ref.[75]
κ-$(ET)_2Cu(NCS)_2$	130-240	Torque magnetometry	Ref.[76]
κ-$(ET)_2Cu(NCS)_2$	120	Josephson plasma resonance	Ref.[77]

Table 5.1: $\lambda_\perp(0)$ for κ-$(ET)_2Cu[N(CN)_2]Br$ and κ-$(ET)_2Cu(NCS)_2$ obtained from various experiments.

$$-\chi_{polygon} = \left[1 - 8\lambda_\perp^2 \sum_{i=1}^{n} \frac{V_i}{V_s} \frac{\ln\left(\frac{\cosh(L_i/2\lambda_\perp)}{\cosh(L_{i-1}/2\lambda_\perp)}\right)}{L_i^2 - L_{i-1}^2}\right] \tag{5.3}$$

In this expression, V_i is the volume of the ith trapezoid or triangle (see Fig. 5.1) and V_s is the total sample volume. As was shown earlier, in strongly demagnetizing geometries, which would occur if the AC field were applied normal to the conducting planes, the effective length scale in Eqn. 5.2 is quite different from the actual sample dimension[78]. For the thin samples used here, this correction was not necessary. Demagnetization was taken in account with a prefactor $1/(1-N)$, which is valid at low temperatures where the susceptibility is close to -1. To estimate the demagnetizing factor N we approximated the sample shape by an inscribed ellipsoid whose demagnetization factor was obtained numerically[79]

$$N = \frac{1}{2}\int_0^\infty \frac{du}{(1+u)^{3/2}\left(1+\frac{Z^2}{X^2}u\right)^{1/2}\left(1+\frac{Z^2}{Y^2}u\right)^{1/2}} \tag{5.4}$$

In this equation, Z is the sample dimension parallel to the applied field while X and Y are dimensions orthogonal to the field. For the κ-$(ET)_2Cu[N(CN)_2]Br$ sample $N \approx .07$ while for the thicker κ-$(ET)_2Cu(NCS)_2$ sample $N \approx 0.16$. The total oscillator frequency shift is then given by $f_s(T) - f_{ec} = gV_s\chi_{polygon}/(1-N)$, where g is a calibration factor related to the coil geometry as described in section 2.4. $\lambda_\perp$ was then obtained by inverting the relation $f_s(T) - f_{ec} = gV_s\chi_{polygon}/(1-N)$ for each temperature. A full inversion procedure was required because the factors $L_i/2\lambda_\perp$ in Eqn. 5.3 could *not* be assumed to be $>> 1$.

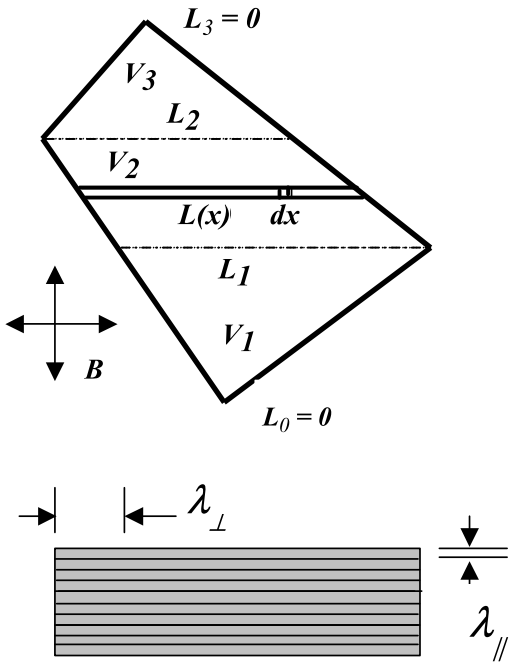


Figure 5.1: (Upper) Polygon-shaped sample looking down onto conducting planes. Two different orientations of rf magnetic field B are shown. L_i and V_i refer to Eqn. 5.3. (Lower) Penetration of in-plane and inter-plane currents into sample. Horizontal lines indicate conducting planes.

5.2 Penetration Depth and Superfluid Density

The values of $\lambda_\perp(0)$ for both κ-$(ET)_2Cu[N(CN)_2]Br$ and κ-$(ET)_2Cu(NCS)_2$ are listed in Table 5.1, along with other reported values. The error bars for the κ-$(ET)_2Cu[N(CN)_2]Br$ measurement are dominated by repeatability in the total frequency shift upon inserting and removing the sample *in situ*, since the sample had a small volume. The errors in the κ-$(ET)_2Cu(NCS)_2$ data represent the spread of values obtained from measuring the sample in the two field orientations. As the table shows, there is a considerable disparity between the various measurements, testifying to both the difficulty of measuring $\lambda_\perp(0)$ accurately and to sample-to-sample dependence. Our previously reported measurement on a much thicker sample of κ-$(ET)_2Cu[N(CN)_2]Br$ gave $\lambda_\perp(0) = 100 \pm 20\mu m$[13].

In clean-limit London superconductors the behavior of the *in-plane* penetration depth $\lambda_{||}$ directly reflects the momentum dependence of gap function. This is true for temperatures below roughly $T_c/3$ where the gap function is essentially constant with temperature. A linear temperature dependence of $\lambda_{||}$ indicates an order parameter with line nodes, as widely observed in the copper oxides[49,28]. The d-wave impurity model mentioned in the previous chapter predicts a temperature dependence of $\lambda_{||} = 1 + AT^2/(T + T^\star)$, where $T^\star$ is an impurity crossover temperature[56]. Previous measurements on both κ-$(ET)_2Cu[N(CN)_2]Br$ and κ-

Material	**n**	α	$T^\star(K)$	**Reference**
κ-$(ET)_2Cu[N(CN)_2]Br$	1.5 ± 0.05	0.72	3.6 ± 0.1	This work
κ-$(ET)_2Cu[N(CN)_2]Br$	1.2 ± 0.1	0.42	0.5	Ref. [13]
κ-$(ET)_2Cu[N(CN)_2]Br$	2			Ref. [76]
κ-$(ET)_2Cu(NCS)_2$	1.4 ± 0.1	0.73	1.9 ± 0.1	This work

Table 5.2: Parameters for fits to $1 - \rho_\perp = bT^n$ and $1 - \rho_\perp = \alpha(T/T_c)/(T + T^\star)$ for both κ-$(ET)_2Cu[N(CN)_2]Br$ and κ-$(ET)_2Cu(NCS)_2$.

$(ET)_2Cu(NCS)_2$ showed exactly this behavior with $T^\star \approx 0.6K$ [13]. To our knowledge there is no theoretical justification for this "dirty d-wave" form for $\lambda_\perp(T)$. Nevertheless, it fits the data extremely well.

In Fig. 5.2, the data for κ-$(ET)_2Cu(NCS)_2$ is shown for one of the two field orientations measured. Fits for κ-$(ET)_2Cu[N(CN)_2]Br$ were of comparable quality. For this orientation, $\lambda_\perp(0) = 119\mu m$. Both $\lambda_\perp$ and the normalized superfluid density $\rho_\perp = [\lambda_\perp(0)/\lambda_\perp(T)]^2$ are plotted along with fits to the dirty d-wave form for $T < 3K$,

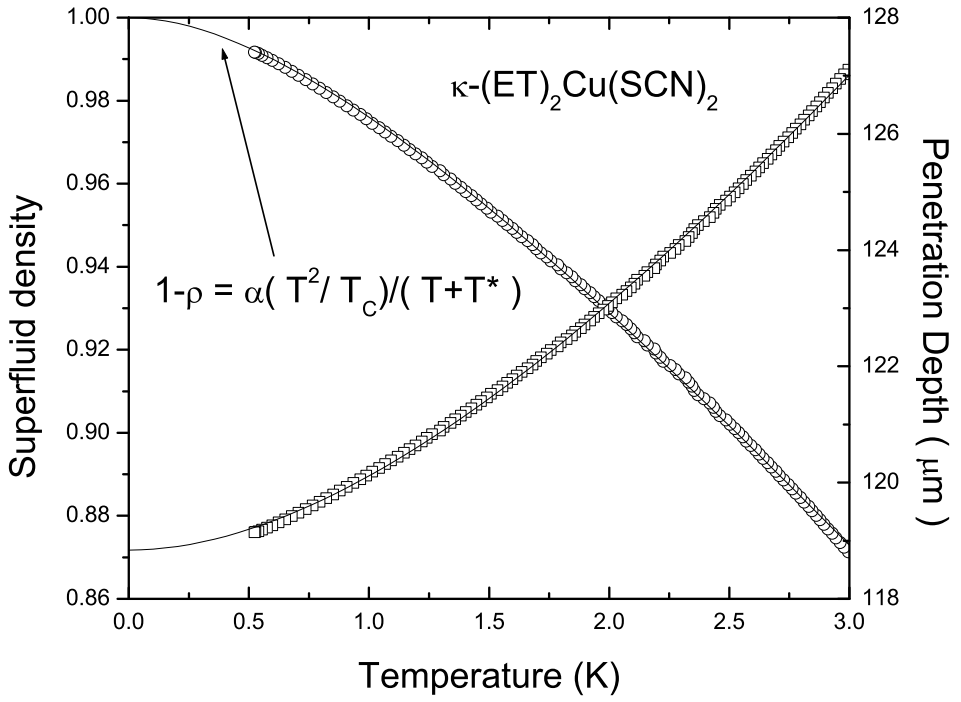


Figure 5.2: $\rho_\perp$ and $\lambda_\perp$ for κ-$(ET)_2Cu(NCS)_2$ with fits to Eqn. 5.5

$$\lambda_\perp = 1 + AT^2/\left(T + T^\star\right), \qquad 1 - \rho_\perp = \alpha\left(T^2/T_c\right)/\left(T + T^\star\right) \tag{5.5}$$

Fig. 5.3 shows the same data fit to a pure power law,

$$\lambda_\perp = \lambda_\perp(0) + aT^{1.58}, \qquad 1 - \rho_\perp = bT^{1.49} \tag{5.6}$$

In Ref.[13] it was shown that the data for $\rho_{||}$ could also be fit to both forms with essentially the same degree of precision.

Table 5.2 summarizes the results for $\rho_\perp$. For κ-$(ET)_2Cu[N(CN)_2]Br$ the error came from uncertainty in $\lambda_\perp(0)$ as described earlier. Nonetheless, the final parameters were largely insensitive to this quantity. For κ-$(ET)_2Cu(NCS)_2$ the errors came predominantly from differences in the two field orientations measured since the demagnetization factors were larger. Overall, we found that $\rho_\perp$ data for both samples could be accurately fit to power laws with relatively small exponents $n = 1.5 \pm 0.05$ (κ-$(ET)_2Cu[N(CN)_2]Br$) and $n = 1.4 \pm 0.1$ (κ-$(ET)_2Cu(NCS)_2$). Alternatively, choosing the dirty d-wave expression resulted in $T^\star = 3.6K$ for κ-$(ET)_2Cu[N(CN)_2]Br$ and $T^\star = 1.9K$ for κ-$(ET)_2Cu(NCS)_2$. These values should be compared to our earlier values of $T^\star = 0.6K$ for$\rho_{||}$[13]. Pinteric *et al.*[74] also measured $\rho_\perp$ in κ-$(ET)_2Cu[N(CN)_2]Br$ and reported an exponent $n \approx 2$. Their data does not go below $T = 1.6$K and shows rather more scatter than our own.

5.3 Discussion

A model for $\rho_\perp(T)$ requires assumptions about the transport channels that participate in the supercurrent. These channels may include wave function overlap, impurity scattering, phonon assisted hopping and resonant tunneling processes. In one limit the system is considered a stack of SIS junctions in which interlayer transport occurs through incoherent processes such as impurity or bosonic scattering. Graf. *et al.* studied this interlayer diffusion model for both s and d-wave pairing[80]. A standard relationship between $\lambda_\perp(0)$ and the critical current $J_c^\perp(0)$ holds, independent of the pairing symmetry,

$$\lambda_\perp(0) = \sqrt{\frac{\hbar}{2e\mu_0 D J_c(0)}} \tag{5.7}$$

For the organics, the spacing between conducting layers $D = 1.5$nm. Using the values in Table 5.2 we obtain 103 A/cm^2 for both materials. Within this model, the normal-state interlayer resistivity $\rho_n^\perp$ is related to the maximum energy gap Δ_0 and $\lambda_\perp(0)$[80],

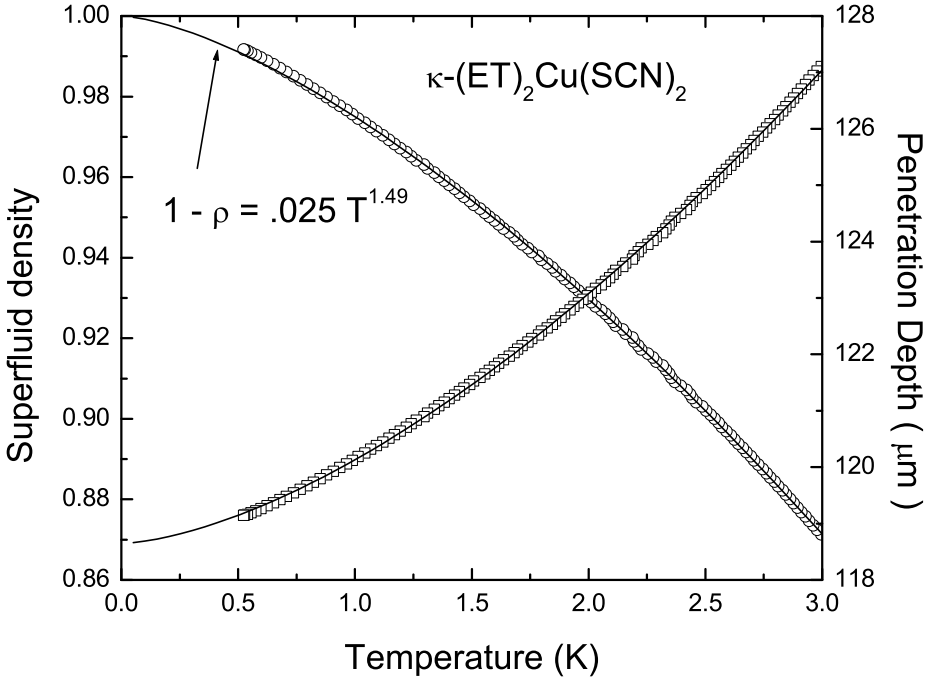


Figure 5.3: $\rho_\perp$ and $\lambda_\perp$ for κ-$(ET)_2Cu(NCS)_2$ with fits to Eqn. 5.6

$$\frac{4\pi^2}{\hbar c^2}\frac{\Delta_0\lambda_\perp^2}{\rho_n^\perp} = \begin{cases} 1 & \text{(s-wave)} \\ R_d \geq 1 & \text{(d-wave).} \end{cases} \tag{5.8}$$

If the scattering is isotropic then $R_d \to \infty$ and so $\lambda_\perp \to \infty$ indicating the lack of Josephson screening currents due to averaging over the d-wave order parameter in momentum space. Josephson screening does appear if the scattering is anisotropic, in which case R_d is finite. Recent specific heat measurements yield a d-wave gap $\Delta_0 = 2.14\beta k_B T_c$ with a strong-coupling enhancements of $\beta = 1.73$ (κ-$(ET)_2Cu[N(CN)_2]Br$) and $\beta = 1.45$ (κ-$(ET)_2Cu(NCS)_2$)[19]. Taking these values, together with $\rho_n^\perp \approx 1\Omega$-cm,[81] we obtain $R_d \approx 30$. This value would imply a d-wave state with isotropic interlayer scattering but again, this conclusion is based on an incoherent transport model. We note that Eqns. 5.7 and 5.8 lead to a generalized Ambegaokar-Baratoff relation[82],

$$\frac{2e}{\pi\Delta_0}\rho_n^\perp J_c^\perp D = \begin{cases} 1 & \text{(s-wave)} \\ R_d^{-1} & \text{(d-wave).} \end{cases} \tag{5.9}$$

For an s-wave superconductor the Ambegaokar-Baratoff model leads to the temperature dependence,

$$\left(\frac{\lambda_\perp(0)}{\lambda_\perp(T)}\right)^2 = \rho_\perp = \frac{\Delta(T)}{\Delta_0}\tanh\frac{\Delta(T)}{2k_BT} \tag{5.10}$$

Our data cannot be fit to this form, even approximately. However, this picture was generalized by Maki and Haas to a d-wave gap function[83]. They found that $1-\rho_\perp \sim T^2$, in reasonable agreement with microwave data on underdoped Bi-2212[84], susceptibility measurements on aligned powders of $HgBa_2Ca_2Cu_3O_{8+\delta}$[85] and measurements on κ-$(ET)_2Cu[N(CN)_2]Br$ by Pinteric *et al.*[15]. Using a somewhat different model for diffusive interlayer transport in a d-wave superconductor[86], Hirschfeld *et al.* predicted $1-\rho_\perp \sim T^3$. Xiang and Wheatley[87] showed that anisotropy in the transfer integrals can lead to $1-\rho_\perp \sim T^5$, which was observed in aligned powders of $HgBa_2CuO_{4+\delta}$[85]. Atkinson and Carbotte have calculated the $\rho_{||}$ and $\rho_\perp$ for proximity-coupled layers (SNS) for both s and d-wave pairing[88]. They show that the superfluid density develops *upward* curvature below some characteristic temperature where the proximity coupling sets in. Upward curvature in the superfluid density appears to be a general characteristic of proximity coupling and was observed previously in Mg-coated MgB_2[89]. However, Figs. 5.2 and 5.3 show no upward curvature so the proximity model for $\rho_\perp$ is not applicable to the organics. The fact that our data accurately obey $1-\rho_\perp \sim T^n$ with $n < 1.5$ appears to rule out all of the above models.

Radtke *et al.* included several contributions to the transport in their calculation of $\rho_\perp$ for a d-wave superconductor[90]. In the limit of purely coherent transport (wave function overlap) they showed that $\rho_\perp$,$\rho_{||}$ should have the same temperature dependence. Sheehy *et al.* developed an alternative theory for $\rho_\perp$ in a d-wave superconductor[91]. In their model, applied to underdoped YBCO, nodal quasiparticles with energies beyond a doping-dependent scale E_c are given reduced weight in determining the superfluid density. Depending upon the relative magnitudes of k_BT,Δ_0, and E_c the power law[91] for $\rho_\perp$ may vary from T to T^3. Qualitatively, the various regimes may be visualized using the quasiparticle wavevector components **k1**, **k2** defined parallel and perpendicular to the Fermi surface at a nodal point, as shown in Fig. 5.4.

The regime of coherent transport corresponds to both **k1** and **k2** preserved during interlayer hopping. In an impurity-free d-wave superconductors this would lead to $1-\rho_\perp \sim T$. The intermediate regime corresponds to the conservation of **k1** but not of **k2**. This situation leads to $1-\rho_\perp \sim T^2$. When neither component is preserved one has $1-\rho_\perp \sim T^3$. Hoessini *et al.* reported $1-\rho_\perp \sim T^{2-2.5}$ in samples of extremely underdoped YBCO.[92] This result signified the presence of nodal quasiparticles and incoherent transport between layers. For the κ-$(ET)_2X$ organics studied here, $1-\rho_\perp \sim T^{1.3-1.5}$ which implies the existence of nodal quasiparticles but-in contrast to the copper oxides-an interlayer transport mechanism that is close to *coherent*, despite strong anisotropy ($\lambda_\perp/\lambda_{||} > 100$).

Probably the clearest indication of coherent interlayer transport in the normal state is the observation of a peak in the angular dependence of the magnetoresistance of κ-$(ET)_2Cu(NCS)_2$ by Singleton *et al.*[93]. Those authors noted that coherence is maintained despite an extremely small transfer integral $t_\perp \approx 0.04meV$, which leads to a violation of the usual condition for coherent transport $t_\perp > \hbar/\tau$, where τ is the in-plane scattering time. In addition, the interlayer resistivity $\rho_n^\perp \approx 1\Omega-$cm is many orders of magnitude higher than that of ordinary metals, although its temperature dependence is metallic. Therefore, one would naively expect these materials to display incoherent transport. And in fact, infrared measurements by McGuire *et al.* of the interlayer conductivity in κ-$(ET)_2Cu[N(CN)_2]Br$ exhibited no Drude peak.[94]. The authors concluded that the transport was indeed incoherent and speculated that the lower frequency measurements were dominated by defects that formed interlayer short circuits. However, it should be noted that the electronic behavior of κ-$(ET)_2Cu[N(CN)_2]Br$ (but not κ-$(ET)_2Cu(NCS)_2$) is highly sensitive to the rate of cooling. Rapid cooling through 80 K leads to partial phase separation[95,23,96] which may account for some of the discrepancies between infrared and low frequency measurements. Finally, recent work by Gutman and Maslov provides new insight into the conduction mechanisms at work[97,98]. They note that in κ-$(ET)_2Cu(NCS)_2$, Sr_2RuO_4 and several other quasi-2D metals, the interlayer resistivity versus temperature passes through a maximum, below which it shows metallic temperature dependence. In κ-$(ET)_2Cu(NCS)_2$ this maximum occurs near 80 K. In their model, there are two parallel interlayer conductance channels. The first, via normal interlayer hopping, leads to band-like metallic contribution. The second consists of phonon-assisted tunneling through resonant defects located between conducting planes. This channel gives an insulator-like temperature dependence. The resistivity maximum represents a competition between the two processes. Their model also predicts a non-Drude frequency dependence in some limits, though it is not clear whether it can reconcile the infrared data with the magnetoresistance and penetration depth measurements.

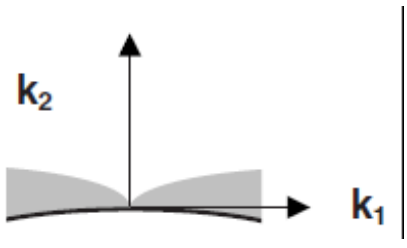


Figure 5.4: Wavevector components near a nodal point on the Fermi surface in a d-wave superconductor.

5.4 Summary

We have measured the interlayer penetration depth $\lambda_\perp$ in both κ-$(ET)_2Cu[N(CN)_2]Br$ and κ-$(ET)_2Cu(NCS)_2$, two closely related quasi-2D organic superconductors. We find that $\lambda_\perp(0) \sim 130\mu$m for both materials. For $T/T_c < 0.3$, the temperature dependence of the interlayer superfluid density $\rho_\perp$ may be fit equally well to a power law $1-\rho_\perp \sim T^{1.3-1.5}$ or to the form $1-\rho_\perp = \alpha\left(T^2/T_c\right)/\left(T+T^\star\right)$ widely used for the in-plane superfluid density in a d-wave superconductor with impurity scattering. Our observations imply that the energy gap is nodal, consistent with d-wave pairing. The relatively low power law exponent ($n = 1.3-1.5$) shows that the interlayer transport is close to coherent, in agreement with magnetoresistance measurements. The appearance of coherent transport differs from the case of copper oxides in which a power law exponent of $n = 2-2.5$ has been taken as evidence for incoherent transport. This finding may be relevant to theories in which interlayer coupling and two-dimensionality play a central role in determining the superconducting transition temperature[99,100].

Appendix A

Attempted STM Fabrication of MgB_2 Nanoislands

A.1 Introduction

A conveniently high transition temperature (39 K)[101] and reduced grain boundary scattering make MgB_2 an attractive material in which to study nanoscale superconductivity. Focused ion beams have been used to fabricate weak links $\sim$ 100 nm wide that exhibit Josephson behavior[102]. While the study of one dimensional (1D) superconductivity in conventional materials such as Al has advanced considerably[103], material issues have made similar studies in the cuprates more difficult. MgB_2 represents a promising new material in which to study 1D effects in a higher temperature superconductor. In addition, MgB_2 possesses two distinct superconducting energy gaps[104,105,106] so its behavior on the nanoscale may be quite different from that of single gap superconductors. Since the coherence length is approximately 5 nm[107], quite small devices would be required to examine MgB_2 in the 1D regime. To this end, we have tried a new approach to fabricating MgB_2 nanowires. Motivated by earlier studies of scanned probe growth[108,109,110,111,112,113,114] we attempted to directly fabricate MgB_2 nanowires with an STM. While we have not yet achieved the goal of a conducting nanowire of MgB_2, we report the appearance of islands formed through the application of a large positive sample voltage in the presence of magnesium and boron reactants. Differential conductance measurements at 70 K indicate that these newly created features have a substantially different conductance than the reactant materials used to create them.

A.2 Experiment

All experiments were performed with an Omicron UHV VT-STM with a variable temperature sample stage. Substrates were boron-doped silicon wafers with resistivities in the range $\rho = 0.005 - 0.013$ Ω-cm. In order to assure smaller defect densities and large terraces, Si(111) was used, with a maximum miscut of $\pm 0.5°$. Our experiments were carried out in a UHV chamber with base pressure $<10^{-11}$ Torr. Sample preparation consisted of outgassing and annealing commonly described in the literature[115]. After annealing for 24 hours,

an image was taken of clean Si surface. Fig. A.1 is a room temperature scan taken with a sample voltage of +1.4 V, showing the expected 7x7 reconstruction.

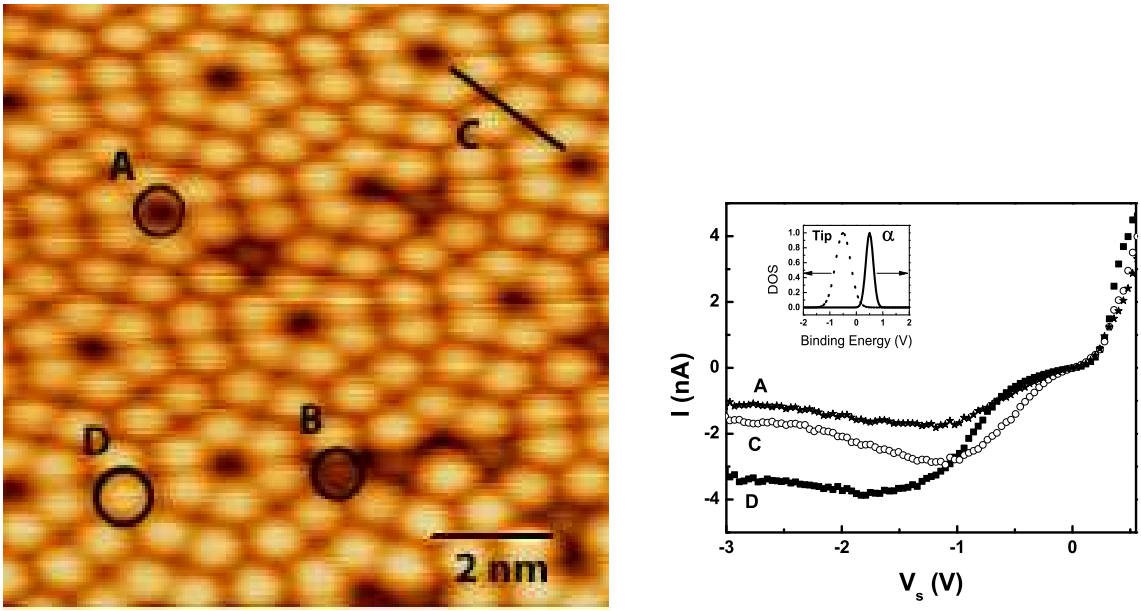


Figure A.1: High resolution image of the empty states of Si(111). Several unique sites are labeled: A) corner hole, B) defect, C) trench, and D) Si atom. Spectroscopy curves are given for non-defect sites with $V_s = 1.4V$ and a tunneling current of 0.2 nA at room temperature. Inset: with the density of states of the tip and boron doped Si surface localized in energy space, rectification is to be expected

Once a satisfactory image of the bare Si(111) surface was obtained, current-voltage (IV) measurements were performed at various locations on the Si surface, as shown in Fig. A.1. All three curves are strongly asymetric. Asymetry can arise for several reasons. First, the curvature of the STM tip results in a nonuniform electric field,

$$E = \frac{E_0}{1 - \frac{z^2}{s(s+R)}} \tag{A.1}$$

where R is the tip curvature, s is the tip-surface separation, and $z = 0$ corresponds to the sample surface. The consequence is to increase the transmission probability for positive sample to tip voltage and decrease the transmission for negative sample to tip voltage[116], leading to rectification. In addition, all three curves appear to have a negative differential resistance (NDR) region. NDR has also been reported in many earlier studies of boron-doped silicon. It has been attributed to localized electrons trapped by boron located under the surface layer of silicon[117,118]. If both tip and sample have an energetically sharp local density of states (LDOS), as shown in Fig. A.1, then scanning the tip-sample voltage will result in a non-monotonic overlap of the two peaks, negative differential resistance and asymetric IV curves[117,118]. These observations, together

with the clear images obtained, suggests that the effective tip in our experiment was atomically sharp.

Having obtained an image of clean silicon, the next step involved the deposition of a sub-monolayer of boron. Boron of 99.9999% purity was placed in a UHV compatible graphite evaporation crucible. Evaporation typically lasted 45 seconds at room temperature. Once the boron deposition was completed, STM images were taken to assess the coverage. Fig. A.2 shows room temperature scans for negative ($V_s = -1.4V$) and positive ($V_s = 1.4V$) sample voltages, respectively. In the former, boron atoms appear as white areas while in the latter they are present but not as widespread. The strong rectification for positive sample voltages resulted in some saturation of the IV curves and lower contrast images. This phenomenon was also displayed by magnesium precursor molecules on bare silicon. As discussed later, this feature was useful in assessing the presence of new reaction products.

Once a satisfactory boron submonolayer was deposited and imaged at room temperature, the sample was cooled to ~70 K. The scan area (40×40 nm^2) was relocated near a terrace edge to find a landmark that could serve as a reference. The system was allowed to scan for one hour to ensure thermal equilibrium. Fig. shows a low temperature (70 K) image taken with positive sample voltage. The image shows perfect 7×7 reconstruction but no obvious boron atoms. The presence of boron was confirmed by negative sample voltage scans, though the scan is not included as a figure. This positive sample voltage image effectively eliminated the boron and magnesium precursor signals and served as a clean slate upon which to observe any new reactants that might be formed.

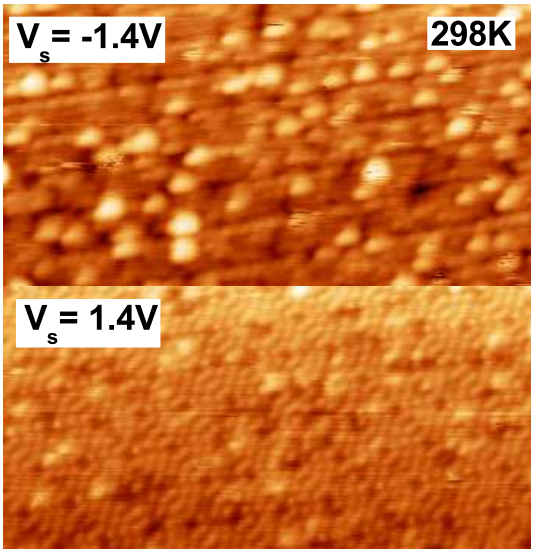


Figure A.2: Top: Occupied states scan (V_s =-1.4V). Boron atoms are represented by the white spots. Bottom: Empty state scan (V_s =1.4V). The Boron atoms are less visible using this tip polarity. Both scans were performed at room temperature.

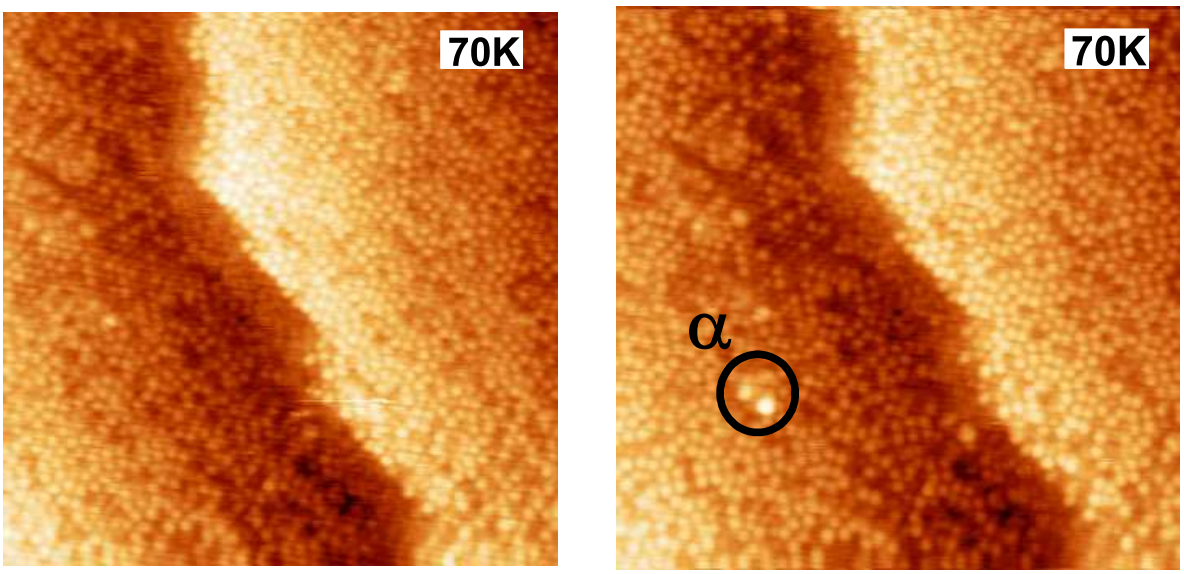


Figure A.3: Image at 70K taken with $V_s = 1.4$V. Notice the circled feature (α) that emerged after scanning with $V_s = 4.4$V in an atmosphere of $MgCp_2$.

The next step was to introduce magnesium to the boron-dusted surface via a precursor molecule. Bis-cyclopentadienyl magnesium ($MgCp_2$) was chosen, a compound widely used to dope GaN with magnesium during chemical vapor deposition[119]. $MgCp_2$ has a melting point of 449 K and a vapor pressure of 0.027 Torr at room temperature. In order to minimize contamination, the precursor was placed in never used, freshly cleaned components in an Ar environment. The precursor was delivered in the form of crystallites sealed in ampoules which were opened under vacuum. Like boron, $MgCp_2$ appeared clearly only in images with negative sample voltage.

In order to induce a chemical reaction, a large positive sample voltage was used while simultaneously scanning the tip across a small area in Fig. zapstrip and dosing the sample with the $MgCp_2$ precursor. The precursor was exposed to the substrate for 60s using a dosing tube a few cm from the sample. While dosing, the chamber pressure remained at $\sim 2 \times 10^{-10}$ Torr. During this exposure, the sample voltage was held at 4.4V for 15s, corresponding to a narrow strip roughly 5 nm in width. After dosing and waiting for the pressure to recover and the scan to stabilize, several images were obtained to make sure the features were not induced by artifacts such as tip-adsorbed molecules or multiple micro tips[120,121]. The before and after images are shown in Fig. A.2. Two noticeable bright spots (circled in Fig. A.2) did appear in the 4.4V region of the scan. The relative scarcity of reaction products may result from the presence of $MgCp_2$ already on the surface blocking reactions with the boron atoms. It may be essential that "airborn" precursor molecules and a clean boron surface are required for an efficient reaction.

A.3 Conductance Spectroscopy

In addition to imaging, local IV measurements were taken with the intent of identifying any new reaction products. Since the experiment required an optimization of imaging, the tip was treated in order to make it atomically sharp. Therefore, the process of sweeping the sample voltage from -3 V to +3V for an IV curve ran the risk of altering the tip enough to destroy its ability to image the surface. IV curves were therefore performed only after the second reaction scan. The curve marked "α" in Fig. A.4 corresponds to the reaction products that are circled and labeled α in Fig. A.2. The curve marked "β" corresponds to an average over the surrounding area and shows a considerably higher conductance at negative voltages. In addition, the curves marked "Boron" and "$MgCp_2$" are room temperature IV characteristics taken at the sites of those materials during a different run. (A negative polarity image was used to actually locate Boron and $MgCp_2$ positions.)

The feature labeled α, formed after the reaction scan, shows negligible conductivity over a span of nearly 3 Volts. STM studies of conductance through single molecules would imply that this value represents a HOMO-LUNO gap of at least 3 eV, with the detailed shape of the IV curve dependent upon the manner in which the electrochemical potential is distributed across the molecule[122]. To our knowledge there are no measurements or calculations of this gap for isolated MgB_2. However, Lombardo et.al.[123] calculated the HOMO-LUMO gap in clusters of the form $(LiBC)_n$ whose electronic structure is apparently very similar to that of MgB_2. For a cluster size of n = 2 they found a gap of 3.4 - 4.1 eV depending upon the spin multiplicity of the cluster. This suggests that the α curve may represent a cluster with electronic structure similar to MgB_2. Obviously data below the superconducting transition temperature is required to determine if MgB_2 itself was formed. As discussed earlier, the IV characteristics are highly dependent upon the nature of the tip. A gently rounded tip has a more constant density of states and leads to IV curves more representative of the sample density of states [120]. Sharp tips, like those used in this experiment, are required for imaging but can result in asymetry and negative differential conductance.

A.4 Discussion

It appears that reaction products were formed using a high voltage tip scan, though their chemical composition is not known. Clearly, much more work is required to increase the reaction yield. The use of highly doped Si(111) as a substrate is beneficial in two ways. First, the Si reconstruction can serve as a way of ensuring that the image is not merely due to a tip effect caused by interacting whiskers [120,121]. Second, the two tip polarities can be used to distinguish the reactants from the product. The occupied state scans can

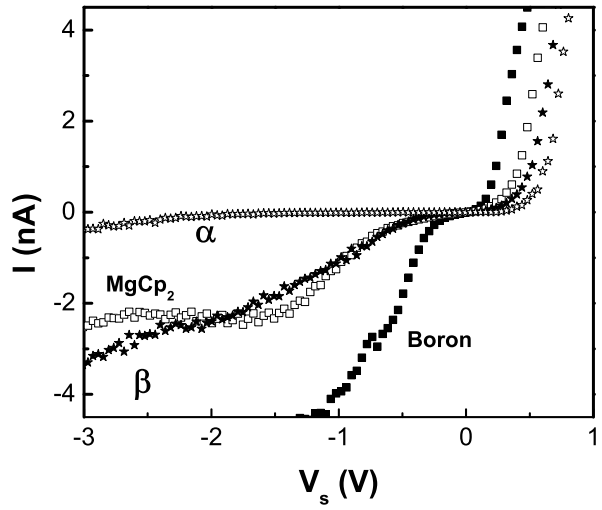


Figure A.4: STS of the new peaks (α) and surrounding silicon (β) covered with boron and $MgCp_2$ at 70K. Room temperature data for boron and $MgCp_2$ from previous runs are also included for comparison. Note that these curves represent an average of many IV curves for each respective site.

be used to measure the boron coverage and assure a submonolayer dusting, while the empty state scan can be used to indicate the regions where the precursor and boron react to give MgB_2.

An alternative fabrication approach would involve hydrogen passivation[124,125,126]. After annealing the silicon and checking for reconstruction, the dangling silicon bonds could be terminated with hydrogen. In doing so, the reconstruction can still be seen, but the surface becomes unreactive to boron or precursor on the whole. Then, high tip voltages could be used to carve designs (by liberating hydrogen) into the hydrogen monolayer, which would later be covered with dosed boron and then reacted with an atmosphere of precursor. In using this approach, the boron can be concentrated in a wire shape and the precursor can be forced to react with the boron using high voltage amplitudes applied to the boron strip. In doing this, the occupied state scan can be used to shape the boron and the empty state scan can be used to see if the precursor reacted to give an MgB_2 wire which could be observed in the empty states scan.

A.5 Conclusion

In exposing a boron-adsorbed, doped Si(1l1) substrate to $MgCp_2$, a large sample voltage (4.4 V) encouraged a reaction between the boron and precursor. A scan of the product feature showed a highly asymetric IV characteristic with with an apparent energy gap of over 3 V. This feature may be indicative of MgB_2 or a material with similar electronic properties.

References

[1] J. Bardeen, L. N. Cooper, and J. R. Schrieffer, Phys. Rev. **106**, 162 (1957).

[2] C. W. Chu, P. H. Hor, R. L. Meng, L. Gao, Z. J. Huang, and Y. Q. Wang, Phys. Rev. Lett. **58**, 405 (1987).

[3] M. K. Wu, J. R. Ashburn, C. J. Torng, P. H. Hor, R. L. Meng, L. Gao, Z. J. Huang, Y. Q. Wang, and C. W. Chu, Phys. Rev. Lett. **58**, 908 (1987).

[4] J. R. Hardy and J. W. Flocken, Phys. Rev. Lett. **60**, 2191 (1988).

[5] J. P. Ferraris, T. O. Poehler, A. N. Bloch, and D. O. Cowan, Tetrahedron Lett. **27**, 2553 (1973).

[6] K. Bechgaard, C. S. Jacobsen, K. Mortensen, M. J. Pedersen, and N. Thorup, Solid State Comm. **33**, 1119 (1980).

[7] K. Bechgaard, K. Carneiro, F. G. Rasmussen, K. Olsen, G. Rindorf, C. S. Jacobsen, H. J. Pederson, and J. E. Scott, J. Am. Chem. Soc. **103**, 2440 (1981).

[8] H. Urayama, H. Yamochi, G. Saito, K. Nozawa, T. Sugano, M. Kinoshita, S. Sato, K. Oshima, A. Kawamoto, and J. Tanaka, Chem. Lett. **1**, 55 (1988).

[9] L. Buravov, N. D. Kushch, V. A. Merzhanov, M. V. Osherov, A. G. Khomenko, and E. B. Yagubskii, J. Phys. I France **2**, 1257 (1992).

[10] W. K. Kwok, U. Welp, K. D. Carlson, G. W. Crabtree, K. G. Vandervoort, H. H. Wang, A. M. Kini, J. M. Williams, D. L. Stupka, L. K. Montgomery, et al., Phys. Rev. B **42**, 8686 (1990).

[11] A. U. B. Wolter, R. Feyerherm, E. Dudzik, S. Sullow, C. Strack, M. Lang, and D. Schweitzer, Phys. Rev. B **75**, 104512 (2007).

[12] H. Elsinger, J. Wosnitza, S. Wanka, J. Hagel, D. Schumacher, and W. Strunz, Phys. Rev. Lett. **84**, 6098 (2000).

[13] A. Carrington, I. J. Bonalde, R. Prozorov, R. W. Giannetta, A. M. Kini, J. Schlueter, H. H. Wang, U. Geiser, and J. M. Williams, Phys. Rev. Lett. **83**, 4172 (1999).

[14] M. Pinterić, S. Tomić, M. Prester, D. Drobac, and K. Maki, Phys. Rev. B **66**, 174521 (2002).

[15] M. Pinteric, S. Tomic, M. Prester, D. Drobac, O. Milat, K. Maki, D. Schweitzer, I. Heinin, and W. Strunz, Phys. Rev. B **61**, 7033 (2000).

[16] S. Belin, K. Behnia, and A. Deluzet, Phys. Rev. Lett. **81**, 4728 (1998).

[17] K. Izawa, H. Yamajuchi, T. Sasaki, and Y. Matsuda, Phys. Rev. Lett. **88**, 027002 (2001).

[18] Y. Nakazawa and K. Kanoda, Phys. Rev. B **55**, R8670 (1997).

[19] O. J. Taylor, A. Carrington, and J. A. Schlueter, Phys. Rev. Lett. **99**, 057001 (2007).

[20] K. Ichimura, M. Takami, and K. Nomura, J. Phys. Soc. Jpn. **77**, 114707 (2008).

[21] S. M. DeSoto, C. P. Slichter, A. M. Kini, H. H. Wang, U. Geiser, and J. M. Williams, Phys. Rev. B **52**, 10364 (1995).

[22] H. Mayaffre, P. Wzietek, D. Jerome, C. Lenoir, and P. Batail, Phys. Rev. Lett. **75**, 4122 (1995).

[23] K. Miyagawa, A. Kawamoto, and K. Kanoda, Phys. Rev. Lett. **89**, 017003 (2002).

[24] A. Kawamoto, K. Miyagawa, and K. Kanoda, Phys. Rev. B **55**, 14140 (1997).

[25] S. Lefebvre, P. Wzietek, S. Brown, C. Bourbonnais, D. Jerome, C. Meziere, M. Fourmigue, and P. Batail, Phys. Rev. Lett. **85**, 5420 (2000).

[26] J. D. Jackson, *Classical Electrodynamics 3rd Edition* (Wiley, 1998).

[27] P. A. Mansky, P. M. Chaikin, and R. C. Haddon, Phys. Rev. B **50**, 15929 (1994).

[28] W. N. Hardy, D. A. Bonn, D. C. Morgan, R. Liang, and K. Zhang, Phys. Rev. Lett. **70**, 3999 (1993).

[29] L. Le, Phys. Rev. Lett. **68**, 1923 (1992).

[30] T. A. Olheiser, Z. Shi, D. D. Lawrie, and R. W. Giannetta, Phys. Rev. B **80**, 054519 (2009).

[31] R. Prozorov, Phys. Rev. B **62**, 115 (2000).

[32] A. R. Smith, D. J. Arnold, and R. W. Mires, Phys. Rev. B **2**, 2323 (1970).

[33] F. Pobell, *Matter and Methods at Low Temperatures* (Springer-Verlag, 1996).

[34] C. V. Degrift, Rev. Sci. Instrum. **46**, 599 (1975).

[35] Russ Giannetta, private communication.

[36] R. K. Cacak and J. R. Craig, Rev. Sci. Instrum. **40**, 1468 (1969).

[37] F. London and H. London, Proc. Roy. Soc. **A149**, 71 (1935).

[38] V. L. Ginzburg and L. D. Landau, J.E.T.P. USSR **20**, 1064 (1950).

[39] C. A. Reynolds, B. Serin, W. H. Wright, and L. B. Nesbitt, Phys. Rev. **78**, 487 (1950).

[40] E. Maxwell, Phys. Rev. **78**, 477 (1950).

[41] P. Monthoux, D. Pines, and G. G. Lonzarich, Nature **450**, 1177 (2007).

[42] T. Ishiguro, K. Yamaji, and G. Saito, *Organic Superconductivity* (Springer-Verlag, 1998).

[43] B. J. Powell and R. H. McKenzie, Phys. Rev. Lett. **94**, 047004 (2005).

[44] P. A. Lee, Rep. Prog. Phys. **71**, 012501 (2008).

[45] D. A. Wollman, D. J. V. Harlingen, W. C. Lee, D. M. Ginsberg, and A. J. Leggett, Phys. Rev. Lett. **71**, 2134 (1993).

[46] K. Kuroki, T. Kimura, R. Arita, Y. Tanaka, and Y. Matsuda, Phys. Rev. B **65**, 100516(R) (2002).

[47] J. M. Schrama, E. Rzepnienski, R. S. Edwards, J. Singleton, A. Ardavan, M. Kurmoo, and P. Bay, Phys. Rev. Lett. **83**, 3041 (1999).

[48] T. Arai, K. Ichimura, K. Nomura, S. Takasaki, J. Yamada, S. Nakatsuji, and H. Anzai, Phys. Rev. B **63**, 104518 (2001).

[49] R. Prozorov and R. W. Giannetta, Supercond. Sci. Technol. **19**, R41 (2006).

[50] A. Carrington and F. Manzano, Physica C **385**, 205 (2003).

[51] A. Maeda, T. Hanaguri, Y. Iino, S. Masuoka, Y. Kokata, J. Shimoyama, and K. Kishio, J. Phys. Soc. Japan **65**, 3638 (1996).

[52] R. Prozorov, M. D. Vannette, R. T. Gordon, C. Martin, S. L. Bud'ko, and P. C. Canfield, Supercond. Sci. Technol. **22**, 034008 (2009).

[53] I. Kosztin and A. J. Leggett, Phys. Rev. Lett. **79**, 135 (1997).

[54] F. Gross, B. S. Chandrasekhar, D. Einzel, K. Andres, P. J. Hirschfeld, H. R. Ott, J. Beuers, Z. Fisk, and J. L. Smith, Z. Phys. B - Condensed Matter **64**, 175 (1986).

[55] D. Xu, S. K. Yip, and J. A. Sauls, Phys. Rev. B **51**, 16233 (1995).

[56] P. Hirschfeld and N. Goldenfeld, Phys. Rev. B **48**, 4219 (1993).

[57] R. Prozorov, R. W. Giannetta, A. Carrington, P. Fournier, and R. L. Greene, Appl. Phys. Lett. **77**, 4202 (2000).

[58] J. Romijn, T. M. Klapwijk, M. J. Renne, and J. E. Mooij, Phys. Rev. B **26**, 3648 (1982).

[59] P. M. Tedrow, G. Faraci, and R. Meservey, Phys. Rev. B **4**, 74 (1971).

[60] N. H. Tea, F. A. B. Chaves, U. Klostermann, R. Giannetta, M. B. Salamon, J. M. Williams, H. H. Wang, and U. Geiser, Physica C **280**, 281 (1997).

[61] A. Kawamoto, K. Miyagawa, Y. Nakazawa, and K. Kanoda, Phys. Rev. Lett. **74**, 3455 (1995).

[62] H. Taniguchi, A. Kawamoto, and K. Kanoda, Phys. Rev. B **59**, 8424 (1999).

[63] X. Su, F. Zuo, J. A. Schlueter, A. M. Kini, and J. M. Williams, Phys. Rev. B **58**, R2944 (1998).

[64] S. Senoussi, A. Tirbiyine, A. Ramzi, A. Haouam, and F. Pesty, Phys. Rev. B **73**, 014525 (2006).

[65] J. Müller, M. Lang, F. Steglich, J. A. Schlueter, A. M. Kini, and T. Sasaki, Phys. Rev. B **65**, 144521 (2002).

[66] A. Kawamoto, K. Miyagawa, and K. Kanoda, Phys. Rev. B **55**, 14140 (1997).

[67] L. P. Le, G. M. Luke, B. J. Sternlieb, W. D. Wu, Y. J. Uemura, J. H. Brewer, T. M. Riseman, C. E. Stronach, G. Saito, and H. Yamochi, Phys. Rev. Lett. **68**, 1923 (1992).

[68] K. Kanoda, Y. Tsubokura, K. Ikeda, T. Takahashi, N. Matsukawa, G. Saito, H. Mori, T. Mori, B. Hilti, and J. S. Zambounis, Synth. Metals **55-57**, 2865 (1993).

[69] T. Sasaki, N. Yoneyama, N. Kobayashi, Y. Ikemoto, and H. Kimura, Phys. Rev. Lett. **92**, 227001 (2004).

[70] Y. J. Uemura, L. P. Le, G. M. Luke, B. J. Sternlieb, W. D. Wu, J. H. Brewer, T. M. Riseman, C. L. Seaman, M. B. Maple, M. Ishikawa, et al., Phys. Rev. Lett. **66**, 2665 (1991).

[71] J. E. Schirber, E. L. Venturini, A. M. Kini, H. H. Wang, J. R. Whitworth, and J. M. Williams, Physica C **152**, 157 (1988).

[72] A. M. Kini, U. Geiser, H. H. Wang, K. D. Carlson, J. M. Williams, W. K. Kwok, K. G. Vandervoort, J. E. Thompson, and D. L. Stupka, Inorg. Chem. **29**, 2555 (1990).

[73] M. M. Mola, J. T. King, C. P. McRaven, and S. Hill, Phys. Rev. B **62**, 5965 (2000).

[74] J. R. Kirtley, K. A. Moler, J. A. Schlueter, and J. M. Williams, J. Phys. Condens. Matter **11**, 2007 (1999).

[75] O. Klein, K. Holczer, G. Gruner, J. J. Chang, and F. Wudl, Phys. Rev. Lett. **66**, 655 (1991).

[76] D. E. Farrell and C. J. Allen, Phys. Rev. B **42**, 8694 (1990).

[77] T. Shibauchi, M. Sato, A. Mashio, T. Tamegai, H. Mori, S. Tajima, and S. Tanaka, Phys. Rev. B **55**, R11977 (1997).

[78] R. Prozorov, R. W. Giannetta, A. Carrington, and F. M. Araujo-Moreira, Phys. Rev. B **62**, 115 (2000).

[79] M. Beleggia, M. D. Graef, and Y. Millev, Philos. Mag. **86**, 2451 (2006).

[80] M. J. Graf, M. Palumbo, D. Rainer, and J. A. Sauls, Phys. Rev. B **52**, 10588 (1995).

[81] X. Su and F. Zuo, Phys. Rev. B **57**, R14056 (1998).

[82] V. Ambegaokar and A. Baratoff, Phys. Rev. Lett. **10**, 486 (1963).

[83] K. Maki and S. Haas, Phys. Rev. B **67**, 020510(R) (2003).

[84] M. B. Gaifullin, Y. Matsuda, N. Chikomoto, J. Shimoyama, K. Kishio, and R. Yoshizaki, Phys. Rev. Lett. **83**, 3928 (1999).

[85] C. Panagopoulos, J. R. Cooper, T. Xiang, G. B. Peacock, I. Gameson, and P. P. Edwards, Phys. Rev. Lett. **79**, 2320 (1997).

[86] P. J. Hirschfeld, S. M. Quinlan, and D. J. Scalapino, Phys. Rev. B **55**, 12742 (1997).

[87] T. Xiang and J. M. Wheatley, Phys. Rev. Lett. **76**, 134 (1996).

[88] W. A. Atkinson and J. P. Carbotte, Phys. Rev. B **51**, 16371 (1995).

[89] R. Prozorov, R. W. Giannetta, S. L. Bud'ko, and P. C. Canfield, Phys. Rev. B **64**, 180501(R) (2001).

[90] R. J. Radtke, V. N. Kostur, and K. Levin, Phys. Rev. B **53**, R522 (1996).

[91] D. E. Sheehy, T. P. Davis, and M. Franz, Phys. Rev. B **70**, 054510 (2004).

[92] A. Hosseini, D. M. Broun, D. E. Sheehy, T. P. Davis, M. Franz, W. N. Hardy, R. Liang, and D. A. Bonn, Phys. Rev. Lett. **93**, 107003 (2004).

[93] J. Singleton, P. A. Goddard, A. Ardavan, N. Harrison, S. J. Blundell, J. A. Schlueter, and A. M. Kini, Phys. Rev. Lett. **88**, 037001 (2002).

[94] J. J. McGuire, T. Room, T. Pronin, T. Timusk, J. A. Schlueter, M. E. Kelly, and A. M. Kini, Phys. Rev. B **64**, 094503 (2001).

[95] M. A. Tanatar, T. Ishiguro, T. Kondo, and G. Saito, Phys. Rev. B **59**, 3841 (1999).

[96] O. J. Taylor, A. Carrington, and J. A. Schlueter, Phys. Rev. B **77**, 060503(R) (2008).

[97] D. B. Gutman and D. L. Maslov, Phys. Rev. B **77**, 035115 (2008).

[98] D. B. Gutman and D. L. Maslov, Phys. Rev. Lett. **99**, 196602 (2007).

[99] P. W. Anderson, Science **268**, 1154 (1995).

[100] A. J. Leggett, Science **274**, 587 (1996).

[101] J. Nagamatsu, N. Nakagawa, T. Muranaka, Y. Zenitani, and J. Akimitsu, Nature **410**, 63 (2001).

[102] A. Brinkman et al., Appl. Phys. Lett. **79**, 2420 (2001).

[103] A. Bezryadin, C. N. Lau, and M. Tinkham, Nature **404**, 971 (2000).

[104] P. Szabó, P. Samuely, J. Kacmarcik, T. Klein, J. Marcus, D. Fruchart, S. Miraglia, C. Marcenat, and A. G. M. Jansen, Phys. Rev. Lett. **87**, 137005 (2001).

[105] H. Schmidt, J. F. Zasadzinski, K. E. Gray, and D. G. Hinks, Phys. Rev. Lett. **88**, 127002 (2002).

[106] F. Manzano, A. Carrington, N. E. Hussey, S. Lee, A. Yamamoto, and S. Tajima, Phys. Rev. Lett. **88**, 047002 (2002).

[107] D. K. Finnemore, J. E. Ostenson, S. L. Bud'ko, G. Lapertot, and P. C. Canfield, Phys. Rev. Lett. **86**, 2420 (2001).

[108] D. D. Awschalom, M. A. McCord, and G. Grinstein, Phys. Rev. Lett. **65**, 783 (1990).

[109] D. S. Saulys, A. Ermakov, E. L. Garfunkel, and P. A. Dowben, J. Appl. Phys. **76**, 7639 (1994).

[110] T. M. H. Wong, S. J. O'Shea, A. W. McKinnon, and M. E. Welland, Appl. Phys. Lett. **67**, 786 (1995).

[111] I. Lyubinetsky, S. Mezhenny, W. J. Choyke, and J. T. Y. Jr., J. Vac. Sci. Technol. A **17**, 1445 (1999).

[112] J. A. Dagata, T. Inoue, J. Itoh, and H. Yokoyama, Appl. Phys. Lett. **73**, 271 (1998).

[113] P. M. Campbell, E. S. Snow, and P. J. McMarr, Surf. Sci. **361/362**, 870 (1996).

[114] R. Held, T. Vancura, T. Heinzel, K. Ensslin, M. Holland, and W. Wegscheider, Appl. Phys. Lett. **73**, 262 (1998).

[115] R. Wolkow, Phys. Rev. Lett. **68**, 2636 (1992).

[116] R. M. Feenstra, J. A. Stroscio, and A. P. Fein, Surf. Sci. **181**, 295 (1987).

[117] I. W. Lyo and P. Avouris, Science **245**, 1369 (1989).

[118] P. Bedrossian, D. M. Chen, K. Mortensen, and J. A. Golovchenko, Nature **342**, 258 (1989).

[119] M. Bartram, MRS Internet J. Nitride Semicon. Res. **5**, 1 (2000).

[120] T. Klitsner, R. S. Becker, and J. S. Vickers, Phys. Rev. B **41**, 3837 (1990).

[121] S. Park, J. Nogami, H. A. Mizes, and C. F. Quate, Phys. Rev. B **38**, 4269 (1988).

[122] S. Datta, W. Tian, S. Hong, R. Reifenberger, J. Henderson, and C. Kubiak, Phys. Rev. Lett. **79**, 2530 (1997).

[123] G. Lombardo, A. Grassi, G. Forte, G. Angilella, R. Pucci, and N. March, Phys. Rev. Lett. **A 338**, 303 (2005).

[124] J. W. Lyding, T. C. Shen, J. S. Hubacek, J. R. Tucker, and G. C. Abeln, Appl. Phys. Lett. **64**, 2010 (1994).

[125] J. A. Dagata, J. Schneir, H. H. Harary, C. J. Evans, M. T. Postek, and J. Bennett, Appl. Phys. Lett. **56**, 2001 (1990).

[126] J. H. Cho, D. H. Oh, and L. Kleinman, Phys. Rev. B **65**, 081310 (2002).